Neutrino Interactions and Nuclear Effects in Oscillation Experiments and the Nonperturbative Dispersive Sector in Strong (Quasi-)Abelian Fields

Dissertation

zur Erlangung des Grades eines
Doktors der Naturwissenschaften
der Abteilung Physik
der Universität Dortmund

vorgelegt von

Yu, Ji-Young

February 2002

To my father

Charity suffereth long, and is kind; charity envieth not; charity vaunteth not itself, is not puffed up, her own, is not easily provoked, thinketh no evil; Rejoiceth not in iniquity, but rejoiceth in the truth; Beareth all things, believeth all things, hopeth all things, endureth all things. Charity never faileth: but whether there be prophecies, they shall fail; whether there be tongues they shall cease; whether there be knowledge, it shall vanish away.

1 Corinthians 13: 4-8

Contents

Preface

This thesis studies primarily neutrino-nucleon and neutrino-nucleus interactions. This topic has become very important with the observatory of neutrino oscillations. In the near future several new experiments, summarized as long-base line experiments, need precise values of the cross section for the interpretation of their results and precise determination of the parameters (δm^2, θ-mixing, etc.). For this reason I began in Dortmund the investigation of this subject. Earlier results are presented in two publications [1, 2]:

- E. A. Paschos, L. Pasquali, J. Y. Yu, Single pion production in neutrino reactions and estimates for charge-exchange effects, Nucl. Phys. B588, 263 (2000) [Chapter 2]

- E. A. Paschos, J. Y. Yu, Neutrino interactions in oscillation experiments, Phys. Rev. D65, 03302 (2002) [Chapter 3]

In the meanwhile I improved several of the calculations, especially the production of the Δ and the other resonances. Old and new results are included in the thesis. In particular part I chapter 2 contains new results including nuclear rescattering corrections.

Before my association with the topic neutrino reactions, I studied the modification of the Euler-Heisenberg Lagrangian in the presence of electric and magnetic fields. With my collaborator Dr. G. Cvetič we calculated the dispersive part as a sum over complex singularities. This is a non-perturbative effect solved by numerical methods. In this context we studied the concept of separation of the induced dispersive action into non-perturbative and perturbative parts using two numerical methods. The results were published in two articles [3, 4]:

- G. Cvetič and Ji-Young Yu, NONPERTURBATIVE DISPERSIVE SECTOR IN

STRONG (QUASI-)ABELIAN FIELDS, Int. J. Mod. Phys. A16, 57 (2001) [Chapter 5–7]

- G. Cvetič and Ji-Young Yu, BOREL-PADÉ VS. BOREL-WENIGER METHOD: A QED AND A QCD EXAMPLE, Mod. Phys. Lett. A15, 1227 (2000) [Chapter 6]

For a complete picture of my contributions to physics I included these results in the second part of this thesis which is giving a short description of the methods and results.

Part I

Neutrino Interations and Nuclear Effects in Oscillation Experiments

Chapter 1

Introduction and Survey

It has long been believed in the Standard Model that neutrinos have zero rest masses. Recent experimental evidence [5–9] for non-vanishing neutrino masses opens a new exciting era in neutrino studies. The question of neutrino mass is one of the major research areas of particle physics both experimentally and theoretically. The evidence of nonzero neutrino masses stems from the neutrino oscillations that a neutrino of one type or flavor, like the muon neutrino, can transform into another state, such as either a tau or a sterile neutrino.

Recently, atmospheric and solar neutrino experiments [5–9] have provided strong evidence for neutrino oscillations. Currently, the experiments are either running or are under construction planning to obtain a better understanding of the reactions and to observe neutrino oscillations, to measure more precisely the magnitudes of the squared mass differences δm^2 and the angle $\sin^2 2\theta$. To perform these measurements special Long Base Line(LBL) experiments have been approved and will be operating. Among them are:

- the present generation of solar and accelerator experiments: Homestake [10], Kamiokande [11, 12], Super-Kamiokande [13], SAGE [14], GALLEX [15], K2K [16], SNO [17]

- the next generation experiments: miniBOONE [18], MINOS [19], ICANOE [20], OPERA [21], ICARUS [22], KamLAND [23], Borexino [24]

- the high-intensity low energy conventional neutrino beam proposal (JHF-Kamioka [25]) and the muon storage rings (Neutrino Factory [26]).

On the other hand, it is important to understand a necessary input for their relevant reactions in free nucleons and to consider the contribution due to the nuclei, since most of them will use (heavy) nuclei as target.

Until now, there are very few studies about the influence of nuclear effects on the nuclei targets. In addition, in the low energy range the neutrino-nucleon reactions are not well understood. Therefore, part I of this thesis is devoted to a careful study of nuclear effects in nuclei targets and the cross sections for the relevant reactions in the LBL experiments.

The outline of Part I will be as follows:

In chapter 2 we present the general formulas for the calculation of single pion production by neutrinos in the resonance regions concerning both charged and neutral current reactions on free protons and neutrons. Then we apply these results to evaluate the spectra of the emerging pions including the Pauli suppression factor and rescattering corrections for reactions in heavy nuclei targets considering the proposed and constructed LBL experiments.

In chapter 3 we give a compendium of the formulas for deep inelastic and quasi-elastic scattering by neutrinos on free protons and neutrons and heavy nuclei targets. We briefly review resonance production for the tau lepton case, since the muon case has already been discussed in chapter 2. In addition, the charged and neutral current cross sections are calculated for the case of muon- and tau-(anti-)neutrino interactions. Furthermore, the nuclear effects are taken into account in DIS by the use of two recent sets of nuclear parton distributions [27–29], in quasi-elastic interactions by the Pauli reduction factor and in the case of resonance production by the ANP model (multiple scattering) [30]. Then, we consider threshold effects in the tau neutrino reactions and use these results to predict tau event rates in the proposed OPERA LBL experiment [21] which will look for $\nu_\mu \to \nu_\tau$ oscillations. Finally, we summarize our main results in chapter 4.

Chapter 2

Neutrino Induced Single Pion Production and Estimation for Nuclear Effects

2.1 Introduction

There is strong evidence for the mixing of muon neutrinos with either tau or sterile neutrinos. The evidence comes from atmospheric neutrino experiments which observe a decrease of muon neutrinos in charged current reactions, but no decrease of the corresponding electron neutrino interactions [5–7].

In order to obtain better insight into the oscillation which takes place and in order to eliminate the dependence on the flux there are proposals and experiments being planned and constructed, which look at the neutral current interactions. These are reactions which will use neutrinos of an average energy of 1 GeV producing the resonances between 1.0 and 1.6 GeV/c^2. One proposal considers the production of pions directly by the atmospheric neutrinos [31] and the detection of π^0's with the help of two ring events.

More powerful are experiments which use neutrinos from an accelerator with two detectors; the first one nearby the accelerator and a second farther away. The nearby detector will be able to detect all pions and check the neutrino flux and the neutrino energy spectrum, as well as the cross sections for these reactions. The detector with the long baseline (300–400 km) will observe the charged and neutral current reactions. The oscillation of muon neutrinos into other neutrinos, tau or sterile neutrinos, will produce a reduction of muon events in the far away detector.

We classify the reactions. Quasi-elastic charged current reactions $\nu_\mu(\bar{\nu}_\mu) + N \rightarrow \mu^-(\mu^+) + N$ and neutral current reaction $\nu + p \rightarrow \nu + p$ [1] are well understood.

In addition to the above reactions there are excitations of resonances and their subsequent decays

$$\nu_\mu + p \rightarrow \mu^- + p + \pi^+ \tag{2.1}$$
$$\nu_\mu + n \rightarrow \mu^- + n + \pi^+ \tag{2.2}$$
$$\nu_\mu + n \rightarrow \mu^- + p + \pi^0 \ , \tag{2.3}$$

to which the corresponding antineutrino-nucleon processes are

$$\bar{\nu}_\mu + p \rightarrow \mu^+ + p + \pi^- \tag{2.4}$$
$$\bar{\nu}_\mu + n \rightarrow \mu^+ + n + \pi^- \tag{2.5}$$
$$\bar{\nu}_\mu + p \rightarrow \mu^+ + n + \pi^0 \ . \tag{2.6}$$

Furthermore, there are the neutral current reactions

$$\nu + p \rightarrow \nu + p + \pi^0 \tag{2.7}$$
$$\nu + p \rightarrow \nu + n + \pi^+ \tag{2.8}$$
$$\nu + n \rightarrow \nu + n + \pi^0 \tag{2.9}$$
$$\nu + n \rightarrow \nu + p + \pi^- \ , \tag{2.10}$$

to which the following antineutrino-nucleon processes correspond

$$\bar{\nu} + p \rightarrow \bar{\nu} + p + \pi^0 \tag{2.11}$$
$$\bar{\nu} + p \rightarrow \bar{\nu} + n + \pi^+ \tag{2.12}$$
$$\bar{\nu} + n \rightarrow \bar{\nu} + n + \pi^0 \tag{2.13}$$
$$\bar{\nu} + n \rightarrow \bar{\nu} + p + \pi^- \ . \tag{2.14}$$

The theory for the production of these states is known for thirty years now and there are several calculations available. The charged current reactions have been studied extensively [32–38] and the production of the Δ^{++} (2.1) has been well understood theoretically. It has also been measured experimentally [32–37] with good agreement between theory and experiment. For the other charged current reactions there are only few experimental

[1] Note that the corresponding reaction $\nu + n \rightarrow \nu + n$ practically is not measurable.

measurements. For this reason the nearby detectors of the experiments should study the reactions using light and heavy nuclei as targets.

Knowledge of the neutral current reactions is even more limited. The latest calculations of charged and neutral current reactions for the production of single-pion cross sections differ by approximately 20% [33, 34, 39]. One should make all possible efforts now to reduce the overall uncertainty and measure the various channels experimentally.

A second difficulty arises from the fact that the experimental targets are heavy materials so that the interactions take place on protons and neutrons bound in nuclei like for example ${}_8O^{16}$, ${}_{18}Ar^{40}$ or ${}_{26}Fe^{56}$. In the heavy nuclei, the produced pions rescatter before they escape from the nucleus and are subject to two phenomena: (1) the cross sections are reduced by the Pauli exclusion principle, when the energy of the recoiling nucleon is low and can not occupy a filled level of nucleons, and (2) the pion charge exchange due to rescattering. These phenomena are known and have been subject of extensive studies [30, 40–42].

The expectations of the experiments are the following. For all charged current reactions we anticipate a reduction of the observed rates in the far away detector because some of the muon neutrinos oscillate into another state. For the neutral current reactions there will be no reduction in rate if the oscillation is to tau neutrinos because all neutrinos contribute equally to neutral current reactions. On the other hand, we expect a reduction if the oscillation is to sterile neutrinos.

Now, since the reduction is expected to be approximately 40% from the calculations, it is important to understand all possible corrections. An important requirement is that the nearby and the far away detector use the same nuclei as targets. If this is not possible, then corrections have to be applied.

Because of the importance of the experiments and the opportunities they present for establishing the charged and neutral current reactions, we have undertaken the task of calculating the cross section on free protons and neutrons. This way we produce differential, as well as integrated cross sections. Then we use the obtained results to calculate the corrections which are present in nuclei.

This chapter is organized as follow:

Section 2.2 is devoted to the calculation of the differential and total cross sections for single-pion production in neutrino-nucleon interactions. In section 2.3 we discuss the

nuclear effects involved in this process adopting the multiple scattering model [30] and calculate the energy spectra for charged and neutral pions for a few different materials typically used as targets in experiments. Finally, conclusions are presented in section 2.4.

2.2 Single Pion Production

In this section we present the main equations and the form factors used to evaluate the differential and total cross sections for single-pion production in neutrino-nucleon interactions. For neutrino energies of a few GeV the single-pion production proceeds mainly through the excitation of the lower resonances. The main contribution to the cross section comes from the production and the subsequent decay of the $\Delta(1232)P_{33}$ resonance. Nevertheless, some of the channels receive a non-negligible contribution from the isospin 1/2 resonances as, for example, the $N(1440)P_{11}$ and the $N(1535)S_{11}$ resonances.

The channels under investigation in this thesis are the six charged current and the eight neutral current channels listed in the introduction in Eqs. (2.1)–(2.14).

Using Clebsch-Gordan coefficients, it is easy to verify that the amplitudes for the charged current channels, Eqs. (2.1)–(2.6), are given by the following relations [33]:

$$\begin{aligned}
A(\mu^- + p + \pi^+) &= A_3^{cc} \\
A(\mu^- + n + \pi^+) &= \frac{1}{3}A_3^{cc} + \frac{2\sqrt{2}}{3}A_1^{cc} \\
A(\mu^- + p + \pi^0) &= -\frac{\sqrt{2}}{3}A_3^{cc} + \frac{2}{3}A_1^{cc} \\
A(\mu^+ + n + \pi^-) &= A_3^{cc} \\
A(\mu^+ + p + \pi^-) &= \frac{1}{3}A_3^{cc} + \frac{2\sqrt{2}}{3}A_1^{cc} \\
A(\mu^+ + n + \pi^0) &= \frac{\sqrt{2}}{3}A_3^{cc} - \frac{2}{3}A_1^{cc}\ ,
\end{aligned} \tag{2.15}$$

and for the neutral current channels, Eqs. (2.7)–(2.14), one obtains [39]:

$$\begin{aligned}
A(\nu + p + \pi^0) &= \frac{\sqrt{2}}{3}A_3^{nc} + \frac{1}{3}A_1^{nc} + \frac{1}{3}A_1^0 \\
A(\nu + n + \pi^+) &= -\frac{1}{3}A_3^{nc} + \frac{\sqrt{2}}{3}A_1^{nc} + \frac{\sqrt{2}}{3}A_1^0 \\
A(\nu + n + \pi^0) &= \frac{\sqrt{2}}{3}A_3^{nc} + \frac{1}{3}A_1^{nc} - \frac{1}{3}A_1^0 \\
A(\nu + p + \pi^-) &= \frac{1}{3}A_3^{nc} - \frac{\sqrt{2}}{3}A_1^{nc} + \frac{\sqrt{2}}{3}A_1^0,
\end{aligned} \tag{2.16}$$

where $A_3^{cc,nc}$ corresponds to the amplitude for the production of the P_{33} resonance, $A_1^{cc,nc}$ is the sum of the amplitudes for the production of the P_{11} and S_{11} resonances and A_1^0 is the sum of the isoscalar contributions of the P_{11} and S_{11} resonances to the cross section.

Notice that, as suggested in Ref. [33, 39], the neutral current amplitudes A_3^{nc}, A_1^{nc} and A_1^0 can be derived from the corresponding charged current amplitudes A_3^{cc} and A_1^{cc} by simply rescaling the vector and axial form factors. In the case of the A_3^{nc} and A_1^{nc} amplitudes the vector and axial charged current form factors need to be multiplied by $1 - 2\sin^2\theta_W$ and by 1 respectively, where θ_W is the Weinberg angle. For A_1^0 the vector and axial charged current form factors need to be multiplied by $-2/3\sin^2\theta_W$ and 0, respectively. Furthermore, since the A_1^0 amplitude turned out to be very small compared to A_3^{nc} and A_1^{nc}, we neglected the isoscalar contribution in our evaluation of the cross sections.

2.2.1 $\Delta(1232)\mathrm{P}_{33}$

As it was mentioned in the introduction, the theory for the production of the $\Delta(1232)\mathrm{P}_{33}$ is well known and understood, and several independent calculations have already been published, showing good agreement with the experimental results [32–37]. Therefore, rather than developing our own formalism for this process, we decided to follow the article of Schreiner and von Hippel [36], who used the Zucker's model [37].

Differential Cross Section

The unpolarized double-differential cross section for the production of the Δ resonance according to the process

$$\nu(q_1) + p(p_1) \rightarrow l^-(q_2) + \Delta^{++}(P_\Delta) \tag{2.17}$$

shown in Fig. 2.1, is given by [36]:

$$\frac{\mathrm{d}\sigma}{\mathrm{d}Q^2\mathrm{d}W^2} = \frac{G_F^2}{16\pi M_N^2}(K_1\widetilde{W_1} + K_2\widetilde{W_2} + K_3\widetilde{W_3}) \ , \tag{2.18}$$

where G_F is the Fermi constant, M_N with $N = n$, p is the nucleon mass, $q^2 \equiv -Q^2$ is the four-momentum transferred from the lepton to the hadron and W^2 is the invariant mass of the hadronic system. Using the four-momenta given in (2.17) [and in Fig. 2.1] we can write:

$$q^2 = -Q^2 = (q_1 - q_2)^2 = -2q_1 \cdot q_2 + m_l^2 = -2E_\nu(E_l - |\vec{q_2}|\cos\theta) + m_l^2, \tag{2.19}$$

$$W^2 = (q + p_1)^2 = -Q^2 + M_N^2 + 2M_N\nu, \tag{2.20}$$

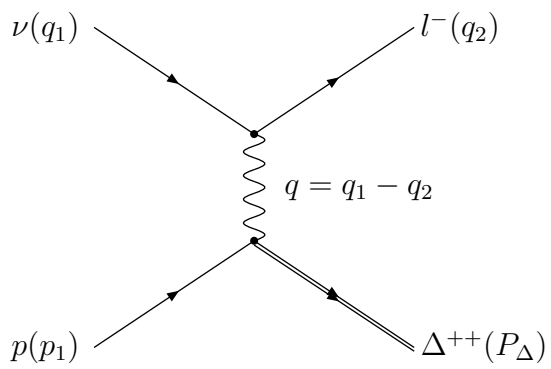

Figure 2.1: The Feynman diagram for the production of the Δ resonance according to the charged current process $\nu(q_1) + p(p_1) \rightarrow l^-(q_2) + \Delta^{++}(P_\Delta)$. q_1, P_1, q_2, P_Δ are the four-momenta of the particles.

where $|\vec{q_2}| = \sqrt{E_l^2 - m_l^2}$, θ is the angle between the initial neutrino and the final lepton, m_l $(l = \mu,\, \tau)$ is the lepton mass, E_ν (E_l) is the energy of the initial neutrino (final lepton) in the *lab* system. Furthermore, the K_i $(i = 1, 2, 3)$ are kinematical factors which are connected to known lepton matrix elements and are given by [37]:

$$K_1 = \frac{2(Q^2 + m_l^2)}{E_\nu^2} \tag{2.21}$$

$$K_2 = 4\big[1 - \frac{(Q^2 + m_l^2)}{E_\nu Q^2}\big(\frac{Q^2 + m_l^2}{4E_\nu} + q_L^0\big)\big] \tag{2.22}$$

$$K_3 = \frac{Q^2 M_N}{E_\nu W q_{CMS}}\big(2 - \frac{q_L^0(Q^2 + m_l^2)}{E_\nu Q^2}\big) \tag{2.23}$$

with

$$\begin{aligned} q_L^0 &= E_\nu - E_\mu = \nu = \frac{W^2 - M_N^2 + Q^2}{2M_N}, \\ q_{CMS}^0 &= \frac{W^2 - M_N^2 - Q^2}{2W}, \\ q_{CMS} &= \sqrt{Q^2 + (q_{CMS}^0)^2}\ , \quad q_{CMS} > 0, \end{aligned} \tag{2.24}$$

where q_{CMS} and q_{CMS}^0 correspond to the three-momentum transfer to the hadrons and energy transfer in the pion-nucleon center of mass system (CMS), respectively, and $q_L^0 = \nu$ is the energy difference in the *lab* system.

Finally, the $\widetilde{W_i}$ are structure functions which describe the hadron currents and they are expressed in terms of the helicity amplitudes from Ref. [37]. In case of the production

of a spin-parity $J^P = \frac{3}{2}$ state the structure functions $\widetilde{W}_i$ are as follows:

$$\begin{aligned}
\widetilde{W}_1 &= \frac{W}{q_{CMS}}\Big(\big[|T_{\frac{3}{2}}|^2 + |T_{\frac{1}{2}}|^2 + |U_{\frac{3}{2}}|^2 + |U_{\frac{1}{2}}|^2\big] + \frac{m_l^2}{q_{CMS}^2}\big[|T_C|^2 + |U_C|^2 + |U_D|^2\big]\Big), \\
\widetilde{W}_2 &= \frac{M_N^2}{W q_{CMS}}\frac{Q^2}{q_{CMS}^2}\Big(\big[|T_{\frac{3}{2}}|^2 + |T_{\frac{1}{2}}|^2 + |U_{\frac{3}{2}}|^2 + |U_{\frac{1}{2}}|^2\big] + \frac{2Q^2}{q_{CMS}^2}\big[|T_C|^2 + |U_C|^2\big]\Big), \\
\widetilde{W}_3 &= \frac{4W}{q_{CMS}}\Big(ReT^*_{\frac{3}{2}}U_{\frac{3}{2}} - ReT^*_{\frac{1}{2}}U_{\frac{1}{2}} + \frac{m_l^2}{q_{CMS}^2}ReU_C^*U_D\Big)\ ,
\end{aligned} \tag{2.25}$$

where T's and U's are helicity amplitudes of the vector and axial-vector currents, respectively, and their subscripts $\frac{3}{2}$ and $\frac{1}{2}$ denote matrix elements of the helicity ± 1 (transverse) currents combining with a nucleon to a Δ whose helicity has absolute value $\frac{3}{2}$ or $\frac{1}{2}$. The subscript $'C'$ means the matrix elements of the Coulomb component of the current and the subscript $'D'$ indicates the matrix elements of its divergence which is zero for the vector current but not for the axial-vector current.

Fully Differential Cross Section

The fully differential cross section with the angular distribution which is fitted by the normalized probability distribution [36] is as follows:

$$\begin{aligned}
\frac{\mathrm{d}\sigma}{\mathrm{d}Q^2\mathrm{d}W\mathrm{d}\Omega_\pi} &= \frac{1}{\sqrt{4\pi}}\frac{\mathrm{d}\sigma}{\mathrm{d}Q^2\mathrm{d}W}\big[Y_0^0 - \frac{2}{\sqrt{5}}(\tilde{\rho}_{33} - \frac{1}{2})Y_2^0 \\
&+ \frac{4}{\sqrt{10}}\tilde{\rho}_{31}ReY_2^1 - \frac{4}{\sqrt{10}}\tilde{\rho}_{3-1}ReY_2^2\big],
\end{aligned} \tag{2.26}$$

where $\mathrm{d}\Omega_\pi = \mathrm{d}\cos\theta_\pi \mathrm{d}\varphi$. Here, $Y_L^M(\Omega)$ are the spherical harmonic functions and some of them are:

$$\begin{aligned}
Y_0^0 &= \frac{1}{\sqrt{4\pi}} \\
Y_2^0 &= \sqrt{\frac{5}{16\pi}}(3\cos^2\theta_\pi - 1) \\
Y_2^1 &= -\sqrt{\frac{15}{8\pi}}\sin\theta_\pi\cos\theta_\pi e^{i\varphi} \\
Y_2^2 &= \sqrt{\frac{15}{32\pi}}\sin^2\theta_\pi e^{2i\varphi}.
\end{aligned} \tag{2.27}$$

We substitute Eq. (2.27) into Eq. (2.26) to integrate over the polar angle φ. As a result we get the cross section:

$$\frac{\mathrm{d}\sigma}{\mathrm{d}Q^2\mathrm{d}W\,\mathrm{d}\cos\theta_\pi} = \frac{\mathrm{d}\sigma}{\mathrm{d}Q^2\mathrm{d}W}\big[\frac{1}{2} - (3/2\cos^2\theta_\pi - \frac{1}{2})(\tilde{\rho}_{33} - \frac{1}{2})\big] \tag{2.28}$$

with

$$(\tilde{\rho}_{33} - \frac{1}{2})\frac{\mathrm{d}\sigma}{\mathrm{d}Q^2\mathrm{d}W} = \frac{W}{M_N^2}\frac{G_F^2}{16\pi}[K_1 D_1 + K_2 D_2 + K_3 D_3]. \tag{2.29}$$

Using Eqs. (2.18) and (2.29) in (2.28) we obtain the final triple-differential cross section:

$$\frac{\mathrm{d}\sigma}{\mathrm{d}Q^2\mathrm{d}W\,\mathrm{d}\cos\theta_\pi} = \frac{G_F^2}{16\pi M_N^2}\sum_{i=1}^{3}\left[K_i\widetilde{W}_i - \frac{1}{2}K_i D_i(3\cos^2\theta_\pi - 1)\right]. \tag{2.30}$$

The structure functions $D_i\,(i = 1, 2, 3)$ are expressed in terms of the helicity matrix elements from Ref. [37] as follows:

$$\begin{aligned}
D_1 &= \frac{W}{q_{CMS}}\Big(\big[|T_{\frac{3}{2}}|^2 - |T_{\frac{1}{2}}|^2 + |U_{\frac{3}{2}}|^2 - |U_{\frac{1}{2}}|^2\big] - \frac{m_l^2}{q_{CMS}^2}\big[|T_C|^2 + |U_C|^2 + |U_D|^2\big]\Big),\\
D_2 &= \frac{M_N^2}{W q_{CMS}}\frac{Q^2}{q_{CMS}^2}\Big(\big[|T_{\frac{3}{2}}|^2 - |T_{\frac{1}{2}}|^2 + |U_{\frac{3}{2}}|^2 - |U_{\frac{1}{2}}|^2\big] + \frac{2Q^2}{q_{CMS}^2}\big[|T_C|^2 + |U_C|^2\big]\Big),\\
D_3 &= \frac{4W}{q_{CMS}}\Big(ReT_{\frac{3}{2}}^* U_{\frac{3}{2}} + ReT_{\frac{1}{2}}^* U_{\frac{1}{2}} - \frac{m_l^2}{q_{CMS}^2}ReU_C^* U_D\Big).
\end{aligned} \tag{2.31}$$

Now, Eq. (2.30) can be converted into the triple-differential cross section $\mathrm{d}\sigma/\mathrm{d}Q^2\mathrm{d}W\mathrm{d}E_\pi$ by using the fact that:

$$E_\pi = E_\pi^L = \gamma E_\pi^{CMS} + \beta\gamma|p_\pi^{CMS}|\cos\theta_\pi \tag{2.32}$$

with the CMS values

$$E_\pi^{CMS} = \frac{M_\Delta^2 + m_\pi^2 - M_N^2}{2M_\Delta}, \tag{2.33}$$

$$|p_\pi^{CMS}| = \sqrt{(E_\pi^{CMS})^2 - m_\pi^2}. \tag{2.34}$$

and the Lorentz factors:

$$\gamma = \frac{\nu + M_N}{M_\Delta}, \quad \beta\gamma = \frac{q_{CMS}}{M_\Delta} = \frac{\sqrt{\nu^2 + Q^2}}{M_\Delta}, \tag{2.35}$$

where $M_\Delta\,(1.232\,\mathrm{GeV})$ denotes the mass of the Δ resonance. Since the triple-differential cross section $\mathrm{d}\sigma/\mathrm{d}Q^2\mathrm{d}W\mathrm{d}\cos\theta_\pi$ changes into $\beta\gamma|p_\pi^{CMS}|\,\mathrm{d}\sigma/\mathrm{d}Q^2\mathrm{d}W\mathrm{d}E_\pi$ using the Lorentz transformation of Eq. (2.32), the final result for the triple-differential cross section is given by:

$$\frac{\mathrm{d}\sigma}{\mathrm{d}Q^2\mathrm{d}W\,\mathrm{d}E_\pi} = \frac{1}{\beta\gamma|p_\pi^{CMS}|}\frac{WG_F^2}{16\pi M_N^2}\sum_{i=1}^{3}\left[K_i\widetilde{W}_i - \frac{1}{2}K_i D_i(3\cos^2\theta_\pi - 1)\right], \tag{2.36}$$

where the kinematic ranges for the $\cos\theta_\pi$ and the pion energy E_π are:

$$-1 \leq \cos\theta_\pi \leq 1 \,, \tag{2.37}$$

$$\Rightarrow \gamma(E_\pi^{CMS} - \beta|p_\pi^{CMS}|) \leq E_\pi \leq \gamma(E_\pi^{CMS} + \beta|p_\pi^{CMS}|). \tag{2.38}$$

The total cross section can be obtained by integrating over the allowed ranges of values of E_π, Q^2 and W^2. In the case of a tau lepton in the final state the Q^2 range is given by:

$$\begin{aligned}
Q^2_{min} &\leq Q^2 \leq Q^2_{max}, \\
Q^2_{min} &= -\frac{1}{(2E_\nu + M_N)}\Big[-2E_\nu^2 M_N + M_N m_\tau^2 + E_\nu(-M_N^2 + m_\tau^2 + W^2) \\
&\quad + E_\nu\sqrt{(s-m_\tau^2)^2 - 2(s+m_\tau^2)W^2 + W^4}\Big], \\
Q^2_{max} &= \frac{1}{(2E_\nu + M_N)}\Big[2E_\nu^2 M_N - M_N m_\tau^2 + E_\nu(M_N^2 - m_\tau^2 - W^2) \\
&\quad + E_\nu\sqrt{(s-m_\tau^2)^2 - 2(s+m_\tau^2)W^2 + W^4}\Big]
\end{aligned} \tag{2.39}$$

with $s = M_N^2 + 2M_N E_\nu$. The integration boundaries in Eq. (2.39) simplify in the limit $m_\tau \to 0$ which is relevant in the case of a muon in the final state:

$$Q^2_{min} = 0, \quad Q^2_{max} = \frac{(s-W^2)(s-M_N^2)}{s}. \tag{2.40}$$

In both cases (muon, tau) the pion energy range is given by Eq. (2.38).

Rarita-Schwinger Formalism

The invariant matrix element for the production of the Δ resonance is as follows [36]:

$$\mathcal{M} = < \mu^- \Delta^{++} | \nu p > = \frac{G_F \cos\theta_c}{\sqrt{2}} j_\alpha < \Delta^{++} | V^\alpha - A^\alpha | p > \,, \tag{2.41}$$

where the hadronic elements V and A denote vector and axial vector parts, respectively, and θ_c is the Cabibbo angle. The leptonic weak current j_α is given by:

$$j^\alpha = \bar{u}_\mu \gamma^\alpha (1-\gamma_5) u_\nu. \tag{2.42}$$

Following the notation of [35] we can express the matrix element as

$$\frac{\mathcal{M}}{\sqrt{3}} = \frac{G}{\sqrt{2}}\bar{\psi}_\alpha \Big\{ \Big[\frac{C_3^V}{M_N}\gamma_\lambda + \frac{C_4^V}{M_N^2}(P_\Delta)_\lambda + \frac{C_5^V}{M_N^2}(P_p)_\lambda \Big]\gamma_5 F^{\lambda\alpha} + C_6^V j^\alpha \gamma_5$$

$$+\Big[\frac{C_3^A}{M_N}\gamma_\lambda + \frac{C_4^A}{M_N^2}(P_\Delta)_\lambda\Big]\gamma_5 F^{\lambda\alpha} + C_5^A j^\alpha + \frac{C_6^A}{M_N^2}q^\alpha q^\lambda j_\lambda\Big\}uf(W) \qquad (2.43)$$

with $F^{\lambda\alpha} \equiv q^\lambda j^\alpha - q^\alpha j^\lambda$. ψ_α is the Rarita-Schwinger spinor for the Δ^{++} spin state, u is the Dirac spinor for the initial proton spin state, P_p is the four-momentum of the proton, and the S-wave Breit-Wigner factor $f(W)$[2] can be written as follows:

$$f(W) = \frac{\sqrt{\frac{\Gamma_\Delta(W)}{2\pi}}}{(M_\Delta - W) - \frac{1}{2}i\Gamma_\Delta(W)}, \quad \Gamma_\Delta(W) = \frac{\Gamma_\Delta^0 q_\pi(W)}{q_\pi(M_\Delta)} \qquad (2.44)$$

with q_π being the modulus of the three-momentum of the pion in the rest frame of the Δ resonance:

$$q_\pi(W) = \sqrt{(W^2 - M_N^2 - m_\pi^2)^2 - 4M_N^2 m_\pi^2}/(2W) \qquad (2.45)$$

and with $\Gamma_\Delta^0 = 120\,\mathrm{MeV}$ being the width of the Δ resonance. The C_j^V and C_j^A ($j = 3, 4, 5, 6$) are the vector and axial-vector form factors. Due to the conserved vector current (CVC) we have $C_6^V = 0$. For our calculation of the cross section we need the connection between the form factors C_j^V, C_j^A and the helicity matrix elements (T's and U's) in Eqs. (2.25) and (2.31). This relationship between them is discussed in appendix A.

Form Factors

For the relevant $N-\Delta$ vector and axial-vector transitions, form factors have been studied extensively for thirty years by the analysis of neutrino scattering experiments [32–38] and quark model calculations [43, 44]. Summaries can be found in Ref. [42].

The vector and axial vector form factors in the approximation of magnetic dipole dominance used in our calculation are the ones given by Alvarez-Ruso et al. [42]. The vector form factors are:

$$C_3^V(Q^2) = \frac{2.05}{(1 + \frac{Q^2}{0.54\,\mathrm{GeV}^2})^2} \qquad (2.46)$$

$$C_4^V(Q^2) = -\frac{M_N}{M_\Delta}C_3^V \qquad (2.47)$$

$$C_5^V(Q^2) = 0, \qquad (2.48)$$

[2]Following Schreiner and von Hippel [36] we parameterize the $\Delta(P_{33})$ resonance by an S-wave Breit-Wigner factor which well describes the experimental data. Alternatively, Rein and Sehgal have utilized a P-wave Breit-Wigner factor [34].

and the axial vector form factors can be parametrized as:

$$C_k^A(Q^2) = C_k(0)\Big(1 + \frac{a_k Q^2}{b_k + Q^2}\Big)\Big(1 + \frac{Q^2}{M_A^2}\Big)^{-2} \tag{2.49}$$

with $k = 3, 4, 5$, $C_3^A(0) = 0$, $C_4^A(0) = -0.3$, $C_5^A(0) = 1.2$, $a_4 = a_5 = -1.21$, $b_4 = b_5 = 2\,\mathrm{GeV}^2$. The axial vector mass M_A is treated as a free parameter. As will be discussed in subsection 2.2.3 we take $M_A = 1.0\,\mathrm{GeV}$. The pion pole dominance of the divergence of the axial vector current can be used to give the following relation:

$$C_6^A(Q^2) = \frac{g_\Delta f_\pi}{2\sqrt{3}M_N}\frac{M^2}{m_\pi^2 + Q^2}, \tag{2.50}$$

where the $\Delta^{++} \to p\pi^+$ coupling constant $g_\Delta = 28.6$, the pion decay constant $f_\pi = 0.97 m_\pi$ and the pion mass $m_\pi = 0.14\,\mathrm{GeV}$. Notice that, since these form factors have been derived from photo- and electro-production experiments in which a Δ^+ or a Δ^0 was produced, in order to obtain the correct cross section for the Δ^{++} production, all the form factors need to be multiplied by $\sqrt{3}$ due to the fact that $< \Delta^{++} \mid \mathrm{V}_\alpha \mid \mathrm{p} >= \sqrt{3} < \Delta^+ \mid \mathrm{V}_\alpha^{\mathrm{em}} \mid \mathrm{p} >$ [36].

2.2.2 N(1440)$\mathbf{P}_{11}$ and N(1535)$\mathbf{S}_{11}$

The $V - A$ form of the leptonic current determines the polarization states of the final muon (as well as that of the initial neutrino) and thus defines a pure polarization state for the virtual W-boson exchanged between the leptons and hadrons. Therefore it is natural to describe the process in terms of cross sections corresponding to the the three helicity states of the virtual W-Boson which is separated into three polarization vectors $\epsilon^r, \epsilon^l, \epsilon^s$ denoting right-handed, left-handed and scalar polarization, respectively.

We show the Feynman diagram for the production of the isospin $I = \frac{1}{2}$ resonances in Fig. 2.2, where k is the neutrino four-momentum, k' is the lepton four-momentum, $\nu = E_\nu - E_l$ is the difference between the energies of the incoming and the outgoing lepton, p and p' are the four-momenta of the initial and final nucleon, respectively, p_π is the four-momentum of the final pion and $q = k - k'$ is the four-momentum transferred from the leptons to the hadrons. The polarization vectors ϵ^i $(i = r, l, s)$ are defined as:

$$\epsilon^s = \frac{1}{Q}\Big(\sqrt{\nu^2 + Q^2}, 0, 0, \nu\Big) \tag{2.51}$$

$$\epsilon^{r,l} = \frac{1}{\sqrt{2}}(0, 1, \pm i, 0) \tag{2.52}$$

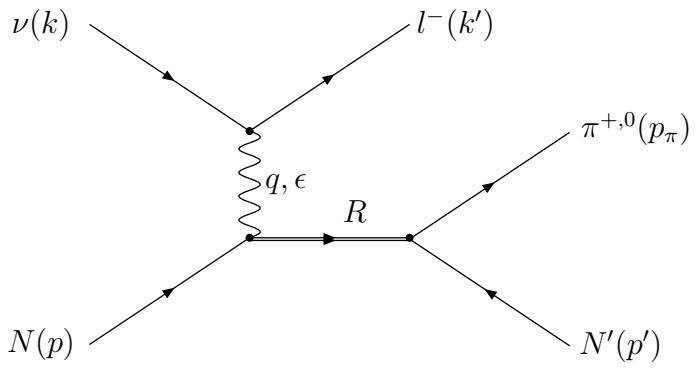

Figure 2.2: s-channel Feynman diagram for the process $\nu(k) + N(p) \to l^-(k') + \pi^{+,0}(p_\pi) + N'(p')$. R denotes one of the two isospin $\frac{1}{2}$ resonances (S_{11}, P_{11}).

and satisfy the following conditions

$$(\epsilon^s)^2 = 1, \quad (\epsilon^{r,l})^2 = -1 \ , \quad (\epsilon^i) \cdot q = 0. \tag{2.53}$$

Remembering that nearby the resonance only the s-channel is essential, the three matrix elements $M_i \, (i = r, l, s)$ can be defined as follows:

$$\mathcal{M}_i = -f_R \bar{u}(p\prime)\gamma_5(\not{p} + \not{q} + M_R)\not{\epsilon}^i(g_V - g_A\gamma_5)u(p)f(W), \tag{2.54}$$

where f_R with $R = P_{11}, S_{11}$ is the coupling constant of the pion to the nucleon and the resonance, M_R is the resonance mass ($M_{P_{11}} = 1.44\,\text{GeV}$, $M_{S_{11}} = 1.535\,\text{GeV}$), and $g_{V,A}$ are the vector and axial form factors, respectively. The values for f_R are given by $f_{P_{11}} = 4.45$ and $f_{S_{11}} = 0.48$ [33]. The Breit-Wigner factor $f(W)$ in Eq. (2.54) for the S_{11} and the P_{11} resonance can be taken in a similar way as in the Δ resonance case (2.44):

$$f(W) = \frac{1}{(W^2 - M_R^2) + iM_R\Gamma_R(W)}, \tag{2.55}$$

changing the resonance mass $M_\Delta \to M_R$ and the width of the resonance $\Gamma^0_\Delta \to \Gamma^0_R$. The widths of the S_{11} and P_{11} resonances are given by $\Gamma^0_{S_{11}} = 0.15\,\text{GeV}$ and $\Gamma^0_{P_{11}} = 0.35\,\text{GeV}$ [45]. In addition, we take the total width $\Gamma_R(W)$ for the S-wave S_{11} resonance from Eq. (2.44). For the P-wave P_{11} resonance we use:

$$\Gamma_{P_{11}}(W) = \Gamma^0_{P_{11}}\Big(\frac{q_\pi(W)}{q_\pi(M_{P_{11}})}\Big)^3, \tag{2.56}$$

where $q_\pi(W)$ is given by Eq. (2.45).

As shown in Ref. [46], the triple-differential cross section $\mathrm{d}\sigma/\mathrm{d}Q^2\mathrm{d}\nu\mathrm{d}\Gamma$ for the production of the P_{11} and S_{11} resonances is given by the following equation:

$$\frac{\mathrm{d}\sigma}{\mathrm{d}Q^2\mathrm{d}\nu\mathrm{d}\Gamma} = \frac{2G_F^2}{(2\pi)^2}\frac{Q^2}{\nu}\Big(1-\frac{Q^2}{2M_N\nu}\Big)\Big[(1-\frac{\nu}{E_\nu})\frac{\mathrm{d}\sigma_s}{\mathrm{d}\Gamma}+\frac{1}{2}(1-\frac{\nu}{E_\nu})^2\frac{\mathrm{d}\sigma_r}{\mathrm{d}\Gamma}+\frac{1}{2}\frac{\mathrm{d}\sigma_l}{\mathrm{d}\Gamma}\Big], \quad (2.57)$$

where the helicity cross sections $\mathrm{d}\sigma_i/\mathrm{d}\Gamma$ for the 'virtual' W-nucleon absorption into final hadronic space spanning the phase space $\mathrm{d}\Gamma$ are defined as:

$$\frac{\mathrm{d}\sigma_i}{\mathrm{d}\Gamma} = \frac{\pi}{\nu}\Big(1-\frac{Q^2}{2M_N\nu}\Big)^{-1}\sum{}' |\mathcal{M}_i|^2(\cos\theta, E_\pi)(2\pi)^4\delta^4(p+q-p_\pi-p'), \quad (2.58)$$

where the summation $\sum'$ is over all final state variables except for the set of final state hadron momenta Γ, which are measured. Inserting Eq. (2.58) into Eq. (2.57) and after some algebra we obtain the final result for the triple-differential cross section:

$$\begin{aligned}\frac{\mathrm{d}\sigma}{\mathrm{d}Q^2\mathrm{d}W\mathrm{d}E_\pi} &= \frac{W}{4M_N}\frac{G_F^2Q^2}{(2\pi)^4\nu^2}\frac{1}{\sqrt{\nu^2+Q^2}}\Big[\big(1-\frac{\nu}{E_\nu}\big)|\mathcal{M}_s|^2(\cos\theta,E_\pi)\\ &\quad +\frac{1}{2}\big(1-\frac{\nu}{E_\nu}\big)^2|\mathcal{M}_r|^2(\cos\theta,E_\pi)+\frac{1}{2}|\mathcal{M}_l|^2(\cos\theta,E_\pi)\Big]\ , \quad (2.59)\end{aligned}$$

where

$$\cos\theta = \frac{Q^2-2(\nu M_N - M_N E_\pi - \nu E_\pi)-m_\pi^2}{2E_\pi\sqrt{\nu^2+Q^2}}. \quad (2.60)$$

Form Factors

For the form factors we use the expressions presented by Fogli and Nardulli in Ref. [33]:

$$g_R^{1V}(Q^2) = -\frac{Q^2 g_R^{2V}(Q^2)}{M_N(M_N-M_R)} \quad (2.61)$$

$$g_R^{2V}(Q^2) = \frac{g_R^V(0)}{(1+\frac{Q^2}{4.3\,\mathrm{GeV}^2})^2}\frac{1}{1+\frac{Q^2}{(M_R-M_N)^2}} \quad (2.62)$$

$$g_R^A(Q^2) = \frac{g_R^A(0)}{(1+\frac{Q^2}{M_A^2})^2}, \quad (2.63)$$

where the $g_R^{V,A}$ denote the vector and axial vector form factors for the resonances S_{11} and P_{11}. For the S_{11} resonance we employ in case of a proton target $g_S^V(0) = -0.28$ and in case of a neutron target $g_S^V(0) = 0.14$. For the P_{11} resonance we take $g_P^V(0) = 0$. The axial vector form factors are $g_{P_{11}}^A(0) = \frac{\sqrt{2}f_P f_\pi}{M_{P_{11}}+M_N} = 0.35$ for the P_{11} resonance and $g_{S_{11}}^A(0) = \frac{\sqrt{2}f_P f_\pi}{M_{S_{11}}+M_N} = 0.16$ for the S_{11} resonance and the axial vector mass is given by $M_A = 1.0\,\mathrm{GeV}$ for both the P_{11} and S_{11} resonance.

2.2.3 Results

In this section we present our results for the total cross sections for the seven channels under examination including the anti-neutrino processes for completeness and, where possible, compare these results with experimental data. They have been calculated by integrating over the allowed range of values for Q^2 and E_π with a cut on the invariant mass W at 1.6 GeV taking Eqs. (2.36)–(2.59). Since some experimental targets consist of heavy nuclei, nuclear effects have to be taken into account in these cases. In addition we investigate also the dependence of the total cross sections on the axial vector mass M_A.

In Fig. 2.3 the total cross section for the $\nu_\mu + p \to \mu^- + p + \pi^+$ process has been plotted versus the incoming neutrino energy. The data points have been taken from Ref. [47] (solid circles) and from Ref. [48] (empty circles) which use hydrogen and deuterium for their experimental targets, respectively. Figs. 2.4–2.5 display the total cross sections for the $\nu_\mu + n \to \mu^- + p + \pi^0$ and $\nu_\mu + n \to \mu^- + n + \pi^+$ processes, respectively, again plotted versus the incoming neutrino energy. In this case the data points have been taken from Refs. [47] (solid circles), [48] (empty circles) and [49] (crosses) using hydrogen, deuterium and CF_3Br (halon) targets, respectively. As can be seen from Figs. 2.3–2.5, the cross sections increase with increasing axial vector mass (due to the factor $(1 + Q^2/M_A^2)^{-1}$) and, at neutrino energies above 1.5 GeV, show a variation of roughly 10% if the axial vector mass is varied by 10%. However, in this region ($E_\nu > 1.5$ GeV) the experimental data are less precise such that the agreement between the theoretical results and the data points is reasonably good for all shown M_A. In the following we utilize $M_A = 1.0$ GeV which seems to be a reasonable choice.

In Fig. 2.6 the total cross section for the $\bar{\nu}_\mu + p \to \mu^+ + p + \pi^-$ process has been plotted versus the incoming neutrino energy. The data points have been taken from Refs. [50] (triangle), [51] (square), and [49] (solid circles) using hydrogen, deuterium and freon targets, respectively. Also here, the agreement between the theoretical curves and the experimental data is quite good.

Figs. 2.7–2.8 display the total cross sections for the $\bar{\nu}_\mu + p \to \mu^+ + n + \pi^0$, and $\bar{\nu}_\mu + n \to \mu^+ + n + \pi^-$ processes, respectively, again plotted versus the incoming neutrino energy. For the latter process the data points have been taken from Refs. [50] (triangle), [51] (square), and [49] (solid circles). The solid and dashed lines take into account the full nuclear corrections according to our (ANP) model which will be discussed in sec. 2.3 and

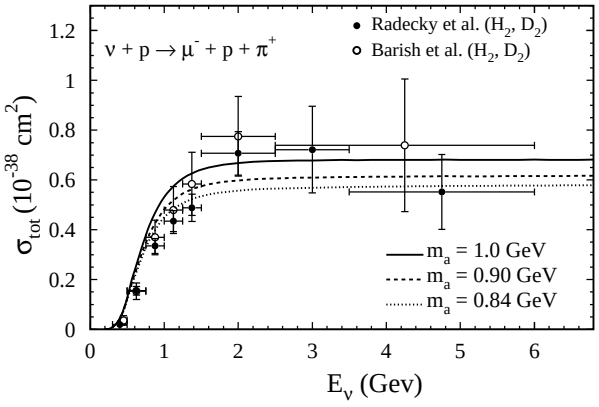

Figure 2.3: Total cross section for the $\nu_\mu + p \to \mu^- + p + \pi^+$ process plotted versus the incoming neutrino energy. The solid, dashed and dotted lines denote axial vector masses $M_A = 1.0$, 0.95 and 0.84 GeV, respectively. The data points are from [47] (H_2, D_2) and [48] (H_2, D_2).

the model of Adler [52], respectively. As can be seen in Fig. 2.8 the resulting curves are very similar and give a satisfactory description of the data. The dotted curve has been calculated without any nuclear corrections and clearly overshoots the data. This nicely illustrates the need of considering nuclear corrections.

The difference between the theoretical and the experimental results can be partially explained by taking into account the fact that, while the theoretical curves have been estimated imposing a cut on the invariant mass W at 1.6 GeV, the experimental points have been obtained without any cut. Notice also that we did not include any non-resonant background and any interference terms of resonances in our evaluation of the cross sections.

In the case of the neutral current interactions, the experimental results are presented in the form of ratios between each of the neutral current channels and one of the charged current channels. For this reason, Figs. 2.9–2.12, which display respectively the total cross sections of the $\nu_\mu(\bar{\nu}_\mu) + p \to \nu_\mu(\bar{\nu}_\mu) + p + \pi^0$, $\nu_\mu(\bar{\nu}_\mu) + p \to \nu_\mu(\bar{\nu}_\mu) + n + \pi^+$, $\nu_\mu(\bar{\nu}_\mu) + n \to \nu_\mu(\bar{\nu}_\mu) + n + \pi^0$ and $\nu_\mu(\bar{\nu}_\mu) + n \to \nu_\mu(\bar{\nu}_\mu) + p + \pi^-$ processes plotted versus the incoming energy, have no data points. Nevertheless, we compared our results with the experimental ratios from Refs. [54–57] and found that there is a reasonable agreement, even if, in some cases, the ratios measured by the different experiments differ a lot from each other. The two Figs. 2.9 (b) and 2.10 (a) as well as the Figs. 2.11 (b) and 2.12 (a) are related by charge symmetry.

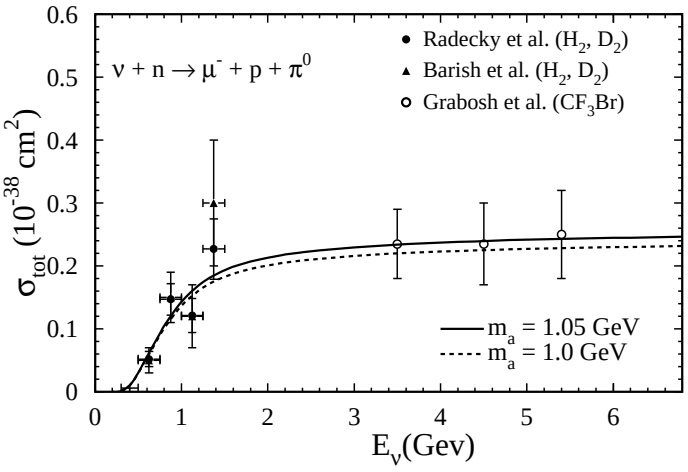

Figure 2.4: Total cross section for the $\nu_\mu + n \rightarrow \mu^- + p + \pi^0$ process plotted versus the incoming neutrino energy. The data points are from [47] (H_2, D_2), [48] (H_2, D_2) and [49] (CF_3Br). The solid and dashed lines have been obtained employing axial vector masses $M_A = 1.05$ and 1.0 GeV, respectively.

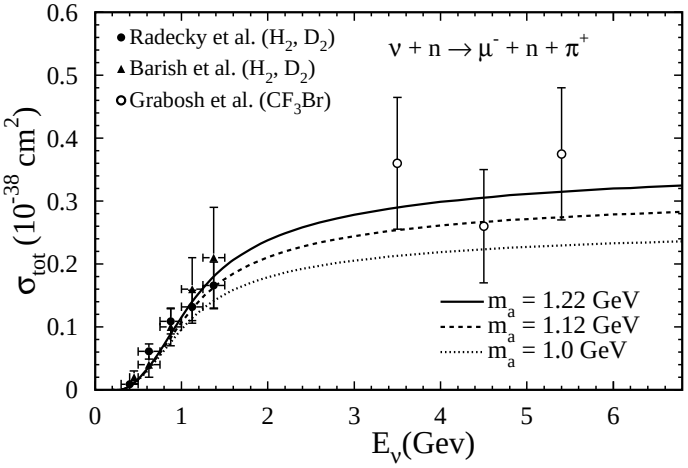

Figure 2.5: Total cross section for the $\nu_\mu + n \rightarrow \mu^- + n + \pi^+$ process plotted versus the incoming neutrino energy. The data points are from [47] (H_2, D_2), [48] (H_2, D_2) and [49] (CF_3Br). The solid, dashed and dotted lines have been obtained employing axial vector masses $M_A = 1.22, 1.12$ and 1.0 GeV.

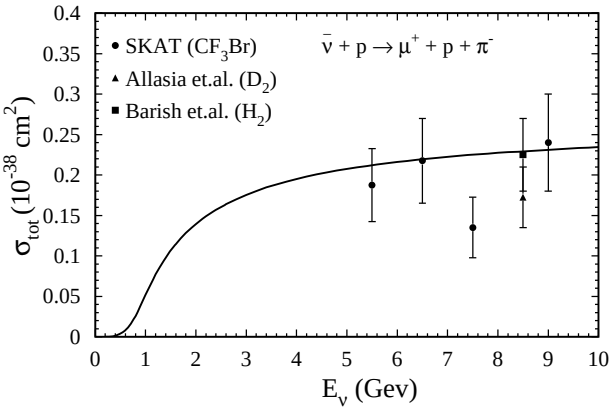

Figure 2.6: Total cross section for the $\bar{\nu}_\mu + p \rightarrow \mu^+ + p + \pi^-$ process plotted versus the incoming neutrino energy. The data points are from [50] (D_2), [51] (H_2), and [49] (CF_3Br).

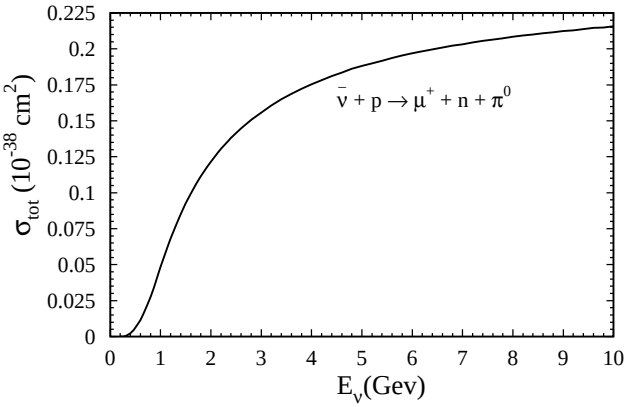

Figure 2.7: Total cross section for the $\bar{\nu}_\mu + p \rightarrow \mu^+ + n + \pi^0$ process plotted versus the incoming neutrino energy.

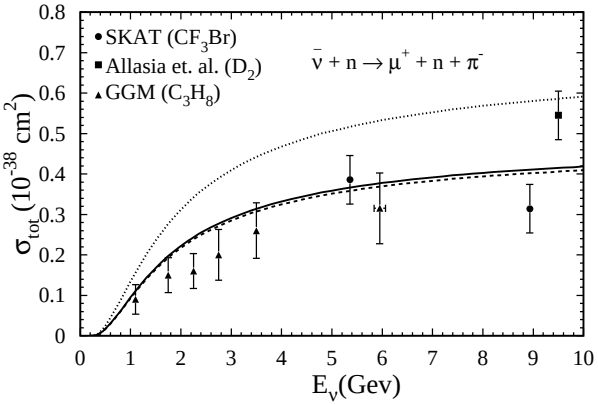

Figure 2.8: Total cross section for the $\bar{\nu}_\mu + n \rightarrow \mu^+ + n + \pi^-$ process plotted versus the incoming neutrino energy. The data points are from [50] (D_2), [49] (CF_3Br), [53] (C_3H_8). The solid and dashed lines take into account nuclear corrections (for propane) according to our (ANP) model and the model of Adler [52], respectively. The dotted line has been calculated without considering nuclear corrections.

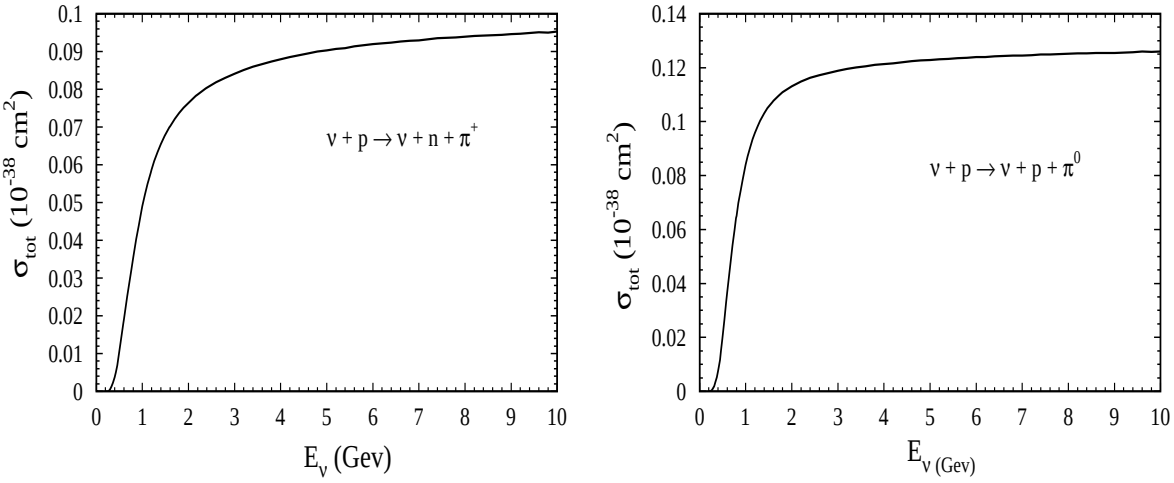

Figure 2.9: Total cross section for the (a) $\nu_\mu + p \rightarrow \nu_\mu + n + \pi^+$ and (b) $\nu_\mu + p \rightarrow \nu_\mu + p + \pi^0$ process plotted versus the incoming neutrino energy.

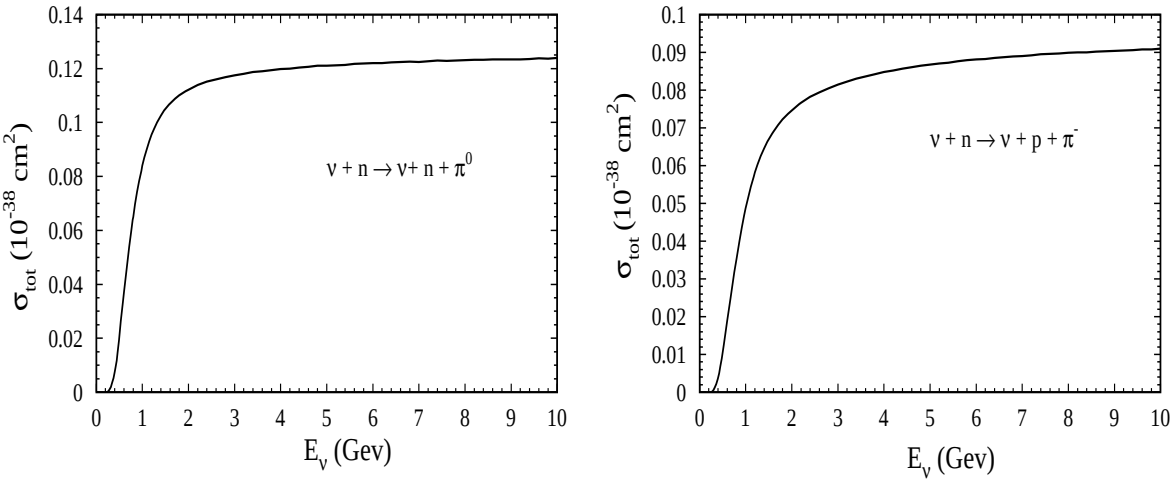

Figure 2.10: Total cross section for the (a) $\nu_\mu + n \rightarrow \nu_\mu + n + \pi^0$ and (b) $\nu_\mu + n \rightarrow \nu_\mu + p + \pi^-$ process plotted versus the incoming neutrino energy.

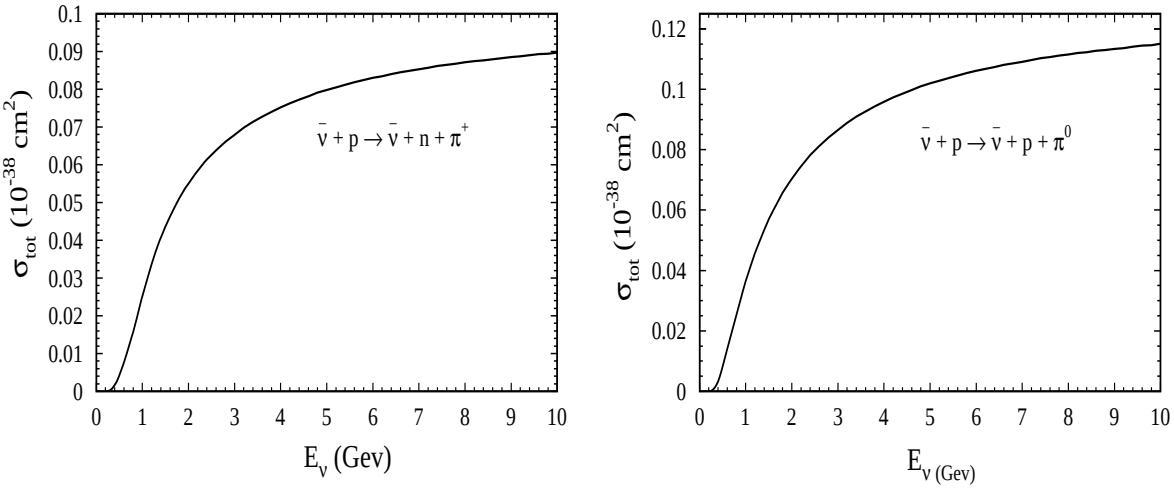

Figure 2.11: Total cross section for the (a) $\bar{\nu}_\mu + p \rightarrow \bar{\nu}_\mu + n + \pi^+$ and (b) $\bar{\nu}_\mu + p \rightarrow \bar{\nu}_\mu + p + \pi^0$ process plotted versus the incoming neutrino energy.

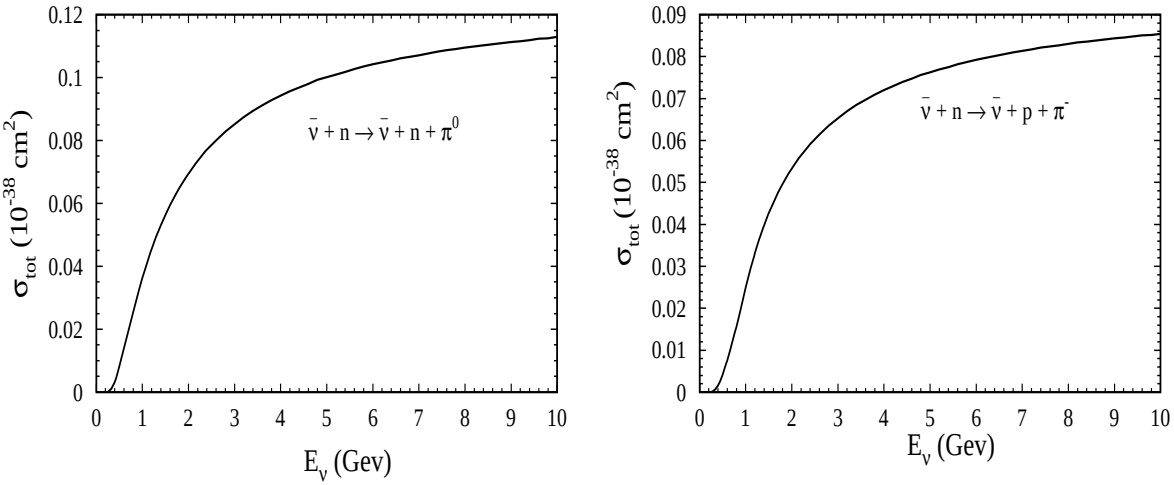

Figure 2.12: Total cross section for the (a) $\bar{\nu}_\mu + n \rightarrow \bar{\nu}_\mu + n + \pi^0$ and (b) $\bar{\nu}_\mu + n \rightarrow \bar{\nu}_\mu + p + \pi^-$ process plotted versus the incoming neutrino energy.

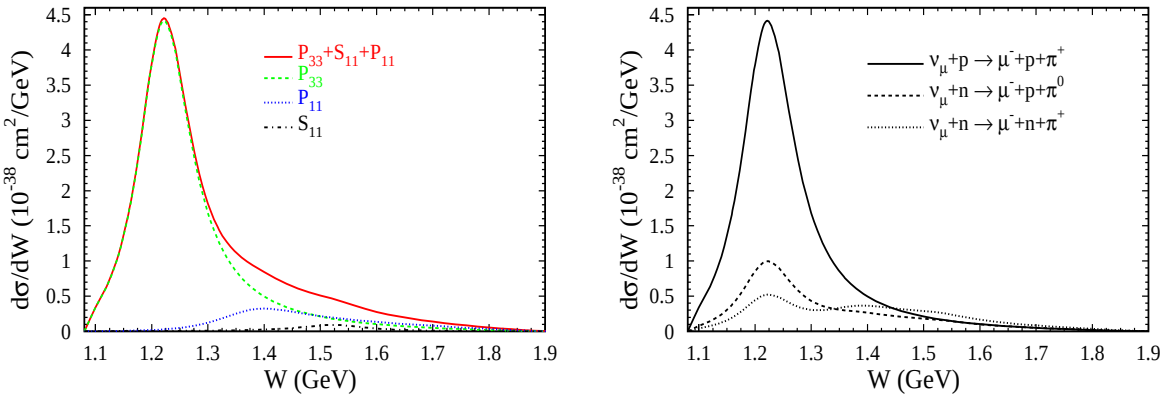

Figure 2.13: Invariant mass W spectra of charged current processes utilizing a fixed neutrino energy $E_\nu = 1.5$ GeV. In (a) the individual contributions from the resonances P_{33} (dashed), P_{11} (dotted), S_{11} (dot-dashed) and the sum $P_{33} + P_{11} + S_{11}$ (solid) are shown. These results have been calculated according to Eqs. (2.36) and (2.59) integrated over E_π and Q^2. In (b) the differential cross sections for the physical processes $\nu_\mu + p \to \mu^- + p + \pi^+$ (solid), $\nu_\mu + n \to \mu^- + p + \pi^0$ (dashed) and $\nu_\mu + n \to \mu^- + n + \pi^+$ (dotted) are plotted.

Finally, in Fig. 2.13 invariant mass spectra $d\sigma/dW$ of several charged current processes are plotted utilizing a fixed neutrino energy $E_\nu = 1.5$ GeV. In Fig. 2.13 (a) the contributions from the resonances P_{33} (dashed), P_{11} (dotted), S_{11} (dot-dashed) and the sum $P_{33} + P_{11} + S_{11}$ (solid) are shown. These results have been calculated according to Eqs. (2.36) and (2.59) integrated over E_π and Q^2. One can see that the delta resonance (P_{33}) dominates over the isospin $I = 1/2$ resonances (P_{11}, S_{11}) for invariant masses $W < 1.4$ GeV, whereas for larger invariant masses the contributions from the P_{11} and S_{11} resonances are not negligible. This is particularly true since the cross sections for the physical processes $\nu_\mu + p \to \mu^- + p + \pi^+$ (solid), $\nu_\mu + n \to \mu^- + p + \pi^0$ (dashed) and $\nu_\mu + n \to \mu^- + n + \pi^+$ (dotted) shown in Fig. 2.13 (b) are linear combinations (C.G. coefficients) of the individual curves in Fig. 2.13 (a) such that the relative importance of the various resonances can be changed.

2.3 Nuclear Effects

In section 2.2 we discussed the reaction $\nu + N \to l + N' + \pi^{\pm,0}$, where N is a free nucleon (proton or neutron). In order to investigate the nuclear effects taking place in the experimental targets (for example, ${}_8O^{16}$, ${}_{18}Ar^{40}$ or ${}_{26}Fe^{56}$), we need to study the modifications necessary for the reaction $\nu + T \to l + T' + \pi^{\pm,0}$, where T is the nuclear

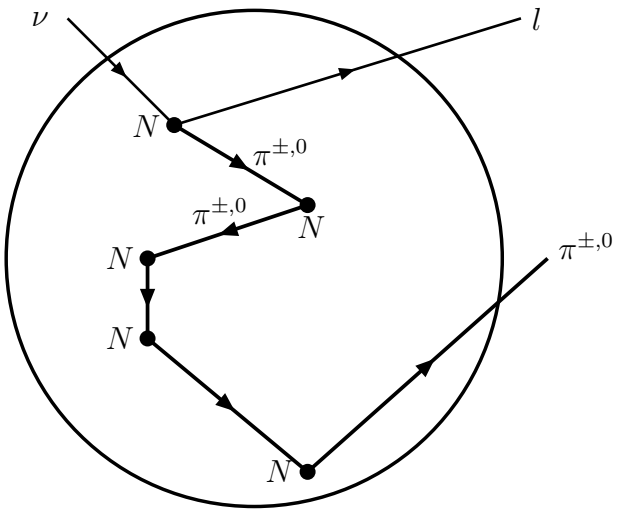

Figure 2.14: Multiple scattering: The incoming neutrinos interact with individual nucleons in the nuclei, producing single pions and excited nuclei. The subsequent journey of the pions is a "random-walk" of multiple scattering until the pion escapes from the nucleus.

target and T' is an unobserved final nuclear state.

We visualize the reaction as a two step process in Fig. 2.14. The incoming neutrinos interact with individual nucleons in the nuclei, producing single pions and excited nuclei. The production process is influenced by the Pauli principle and the Fermi-motion of the individual nucleons. The subsequent journey of the pions is a "random-walk" of multiple scattering until the pion escapes from the nucleus. In the multiple scattering the pions can exchange their charge. The most important effects can be summarized as: charge exchange through the reaction $\pi^i + N \rightarrow \pi^j + N'$, absorption of pions, changing of the direction of pions and Pauli effects. The model of Adler, Nussinov and Paschos (ANP) [30] treats the neutrino induced pion production in the nuclei taking into account all these effects with some constraints. Their model is based mainly on a Clebsch-Gordan analysis and the transport integral equation of the pions.

In this subsection we will outline the theoretical aspects of nuclear effects in nuclei adopting the ANP model. This section is organized in the following way:

In subsection 2.3.1 we explain the general transport problem in a nucleus. In subsection 2.3.2 we discuss the charge density distribution in different nuclear targets. The scattering matrix Q is presented in subsection 2.3.4. The charge exchange matrix M is widely

discussed including the Pauli suppression factor and the function $f(\lambda)$ in subsections 2.3.3 and 2.3.6. Two Pauli factors are discussed in subsections 2.3.7. In subsection 2.3.8 we denote briefly the averaging approximation of the dynamical function $f(\lambda)$. Finally, numerical results are presented in subsection 2.3.9.

2.3.1 General Transport Problem in Nuclei

If an (anti-)neutrino flux hits a nuclear target T (for example, ${}_8O^{16}$, ${}_{18}Ar^{40}$ or ${}_{26}Fe^{56}$), pions are produced by the reactions (2.1)–(2.12). During the journey the produced pions interact with protons and neutrons in the nucleus, before they escape from it and are detected, see Fig. 2.14. The interesting reactions for the latter (multiple scattering) step are as follows:

$$\pi^+ + N \rightarrow \pi^+ + N \tag{2.64}$$

$$\pi^+ + n \rightarrow \pi^0 + p \tag{2.65}$$

$$\pi^0 + N \rightarrow \pi^0 + N \tag{2.66}$$

$$\pi^0 + p \rightarrow \pi^+ + n \tag{2.67}$$

$$\pi^0 + n \rightarrow \pi^- + p \tag{2.68}$$

$$\pi^- + N \rightarrow \pi^- + N \tag{2.69}$$

$$\pi^- + p \rightarrow \pi^0 + n \tag{2.70}$$

and

$$\pi^{\pm,0} + N \rightarrow X. \tag{2.71}$$

The reaction (2.71) is corresponding to the pion absorption, where the final state does not contain any pions. We do not consider more than one pion production reactions and processes which are not important in the Δ resonance region. For the reactions (2.64)–(2.70) the main nuclear corrections are: charge exchange, Pauli effects, pion absorption,

changing of the pion direction and Fermi motion. We neglect Fermi motion and nucleon recoil effects because we consider the nucleon to be fixed within the nucleus.

For the charge exchange processes in Eqs. (2.65), (2.67), (2.68) and (2.70) a scattering matrix Q is considered using a simple isospin Clebsch-Gordan analysis of the channel $I = \frac{3}{2}$. Since the second step is independent of the identity of the leptons involved in the first step, we can factorize the nuclear effects like pion charge exchange and absorption in the charge exchange matrix M. Interactions of the produced pions in the nucleus are dealt with the approximation of complete incoherence, including the utilization of the pion-nucleon cross sections rather than scattering amplitude in the multiple scattering calculation. There are two relevant cross sections, i.e., the elastic and the absorption cross section, in the Δ resonance region. The elastic scattering is taken by [58]:

$$\frac{\mathrm{d}\sigma_{elastic}}{\mathrm{d}\Omega} \propto \sigma_{\pi^+ p}(W)(1 + 3\cos^2\phi), \tag{2.72}$$

where ϕ is the pion scattering angle and W is the invariant mass. Since the Δ resonance dominates compared to the resonance channels $I = \frac{1}{2}$, we consider all πN scattering in the Δ resonance region. We treat the multiple scattering problem as an one-dimensional problem because the three dimensional spherical problem is solved by the ANP model [30] and because there are very small deviations between the one and the three dimensional treatment of the multiple scattering problem.

There is another nuclear effect which does not depend on the pion scattering, namely, the Pauli factor in pion-leptoproduction reactions (2.1)–(2.14) in a nucleus. This reduction factor depends on the invariant mass W and Q^2 and is denoted as $g(W, Q^2)$. A second Pauli factor exists in the pion-nucleon scattering and depends on the pion energy E_π and the pion scattering angle ϕ.

Before we discuss the nuclear effects in the nucleus according to the multiple scattering model [30], we outline useful constraints for our studies:

- pion-nucleon reactions take place in the Δ resonance region
- the number of protons is the same as the number of neutrons in the target nucleus
- the neutrino-pion production by bound nucleons should be the same as neutrino-pion production by a free nucleon.
- E_π does not change in elastic scattering

- approximately, the target nucleus is assumed to be isotropically neutral.

2.3.2 Charge Density Distributions

Following Ref. [30], we treat the target nucleus as a collection of independent nucleons which are distributed in space accordingly to a density profile determined through electron-nucleus scattering experiments.

For the charge density profile of ${}_8O^{16}$ we adopt the harmonic oscillator model in which the density is given by [59]:

$$\rho(r) = \rho(0)\exp(-r^2/R^2)\left(1 + C\frac{r^2}{R^2} + C_1\left(\frac{r^2}{R^2}\right)^2\right), \tag{2.73}$$

where $R = a/K$ with $K = \sqrt{3(2+5C)/2(2+3C)}$ and a is the root mean square radius. The constants C and C_1 are free parameters depending on the material. For ${}_{18}Ar^{40}$ and ${}_{26}Fe^{56}$ we use the two parameters Fermi model [59] and write the charge density in the following way:

$$\rho(r) = \rho(0)\left[1 + \exp\left((r-C)/C_1\right)\right]^{-1} . \tag{2.74}$$

Note that we take different models for various nuclei to describe their charge density due to the fact that they have distinct charge density profiles. The density $\rho(r)$ is normalized as $\int \mathrm{d}^3 r \rho(r) = A$, where A denotes the number of protons plus neutrons in the nucleus.

The different parameters used in Eqs. (2.73) and (2.74) are given in Ref. [59] and are summarized in Table 2.1.

${}_ZT^A$	$a[fm]$	$C[fm]$	$C_1[fm]$	$R[fm]$	$\rho(0)[fm^{-3}]$
${}_8O^{16}$	2.718	1.544	0	1.833	0.141
${}_{18}Ar^{40}$	3.393	3.530	0.542	4.830	0.176
${}_{26}Fe^{56}$	3.801	4.111	0.558	4.907	0.163

Table 2.1: Charge density distribution parameters

2.3.3 Charge Exchange Matrix M

The final and initial pion distributions are related to each other through a scattering matrix Q whose coefficients result from a Clebsch-Gordan analysis as follows:

$$\bar{q}_i = \sum_{j=\pm,0} Q_{ij} q_{Ij}, \tag{2.75}$$

where the indices $i, j = \pm, 0$ denote the final and initial pion charge states. The initial and final pion charge states are defined by:

$$q_I = \begin{pmatrix} \pi^+ \\ \pi^0 \\ \pi^- \end{pmatrix}_I, \tag{2.76}$$

$$\bar{q} = \begin{pmatrix} \pi^+ \\ \pi^0 \\ \pi^- \end{pmatrix}_F. \tag{2.77}$$

The multiple scattering process can be represented by the application of the matrix Q^n on q_I. q_I can be decomposed into a sum of eigenvectors q_k and their eigenvalues λ_k:

$$q_I = \sum_{k=1}^{3} C_k q_k, \quad Q\, q_k = \lambda_k q_k \tag{2.78}$$

with the coefficient C_k. Thus we can rewrite the final pion distribution as follows:

$$\begin{aligned} \bar{q} &= \sum_{n=0}^{\infty} Q^n q_I = \sum_{n=0}^{\infty} \sum_{k=1}^{3} Q^n C_k q_k \\ &= \sum_{n=0}^{\infty} \sum_{k=1}^{3} \lambda_k^n C_k q_k. \end{aligned} \tag{2.79}$$

Absorption of pion and changing of the pion direction except for the charge exchange can be understood by the number of pions $N^{(n)}$ exiting from the medium after exactly n-interactions, since they are independent on the charge exchange. Therefore we can modify Eq. (2.79) in the following form:

$$\bar{q} = \sum_{n=0}^{\infty} N^{(n)} Q^n q_I$$

$$= \sum_{n=0}^{\infty}\sum_{k=1}^{3} N^{(n)}\lambda_k^n C_k q_k$$
$$= \sum_{k=1}^{3} f(\lambda_k) C_k q_k \tag{2.80}$$

with

$$f(\lambda_k) = \sum_{n=0}^{\infty} \lambda_k^n N^{(n)}. \tag{2.81}$$

$f(\lambda_k)$ contains all the dynamics of the multiple scattering problem and the coefficient C_k are linear combinations of the initial pion mutiplicities. $\bar{q}$ and q_I which denote differential cross sections for leptonic pion production on nuclear and on free nucleon targets, respectively, are linked by the so called charge exchange matrix M in the following way:

$$\begin{pmatrix} \frac{\mathrm{d}\sigma({}_Z T^A;+)}{\mathrm{d}Q^2\mathrm{d}W\mathrm{d}E_\pi} \\ \frac{\mathrm{d}\sigma({}_Z T^A;0)}{\mathrm{d}Q^2\mathrm{d}W\mathrm{d}E_\pi} \\ \frac{\mathrm{d}\sigma({}_Z T^A;-)}{\mathrm{d}Q^2\mathrm{d}W\mathrm{d}E_\pi} \end{pmatrix} = M \begin{pmatrix} \frac{\mathrm{d}\sigma(N_T;+)}{\mathrm{d}Q^2\mathrm{d}W\mathrm{d}E_\pi} \\ \frac{\mathrm{d}\sigma(N_T;0)}{\mathrm{d}Q^2\mathrm{d}W\mathrm{d}E_\pi} \\ \frac{\mathrm{d}\sigma(N_T;-)}{\mathrm{d}Q^2\mathrm{d}W\mathrm{d}E_\pi} \end{pmatrix}, \tag{2.82}$$

where

$$\frac{\mathrm{d}\sigma(N_T;\pm 0)}{\mathrm{d}Q^2\mathrm{d}W\mathrm{d}E_\pi} = Z\frac{\mathrm{d}\sigma(p;\pm 0)}{\mathrm{d}Q^2\mathrm{d}W\mathrm{d}E_\pi} + (A-Z)\frac{\mathrm{d}\sigma(n;\pm 0)}{\mathrm{d}Q^2\mathrm{d}W\mathrm{d}E_\pi}\ . \tag{2.83}$$

Its eigenvalues define beams of pions of specific charge combination, which is decreased by the appropriate eigenvalue. The complete scattering phenomenon is characterized by three transition probabilities $f(\lambda_k)$ corresponding to the three eigenvalues of the matrix M. They describe the probabilities of beams with eigenvalues λ_k to survive and exit the nucleus. When we transpose the final pion to the initial state, we obtain the isospin of the system $\pi_i + \bar{\pi}_f$ whose total isospin can be 0, 1 and 2. Therefore we deduce that the charge exchange matrix M includes three independent parameters. Using this property M can be expressed in terms of three parameters A_p, c and d

$$M = A_p \begin{pmatrix} 1-c-d & d & c \\ d & 1-2d & d \\ c & d & 1-c-d \end{pmatrix}\ . \tag{2.84}$$

The overall factor A_p is given by

$$A_p = g(W, Q^2)\, a \tag{2.85}$$

with the Pauli suppression factor $g(W, Q^2)$ in Eq. (2.165) and $a = f(1)$. Using the following identity:

$$\bar{q} = Mq_I = \sum_{k=1}^{3} f(\lambda_k)\, C_k\, q_k, \tag{2.86}$$

we can determine the elements of the charge exchange matrix M. In subsection 2.3.5 we will discuss some details of the dynamical function $f(\lambda_k)$.

2.3.4 Scattering Matrix Q

We analyzed the reactions (2.64)–(2.70) by means of a Clebsch-Gordan analysis, neglecting the isospin $\frac{1}{2}$ channels because the Δ resonance plays the dominant role. The pion-nucleon matrix elements are as follows:

$$M(\pi^i N \to \pi^j N') = C_{ij}(N) < 3/2|S|3/2 > \tag{2.87}$$

with the Clebsch-Gordan coefficient C_{ij}. The probability P that a π^i $(i = \pm, 0)$ is converted into a π^k $(k = \pm, 0)$ by a single scattering process is given by:

$$P_{ik} = \frac{\sum_{N=p,n} |C_{ik}(N)|^2}{\sum_{j=\pm,0} \sum_{N=p,n} |C_{ij}|^2} \tag{2.88}$$

with

$$\begin{aligned} C_{++}(p) &= 1 & C_{--}(p) &= \frac{1}{3} \\ C_{++}(n) &= \frac{1}{3} & C_{--}(n) &= 1 \\ C_{+0}(n) &= \frac{\sqrt{2}}{3} & C_{-0}(p) &= \frac{\sqrt{2}}{3} \\ C_{00}(p) &= \frac{2}{3} & C_{0+}(p) &= \frac{\sqrt{2}}{3} \\ C_{00}(n) &= \frac{2}{3} & C_{0-}(n) &= \frac{\sqrt{2}}{3} \end{aligned} \tag{2.89}$$

corresponding to the reactions (2.64)–(2.70). We identify the matrices P_{ij} and Q_{ij} and obtain the following matrix elements of Q:

$$Q = \begin{pmatrix} \frac{5}{6} & \frac{1}{6} & 0 \\ \frac{1}{6} & \frac{2}{3} & \frac{1}{6} \\ 0 & \frac{1}{6} & \frac{5}{6} \end{pmatrix} . \tag{2.90}$$

The eigenvalues and eigenvectors are obtained by a simple calculation:

$$q_1 = \begin{pmatrix} 1 \\ 1 \\ 1 \end{pmatrix}, \lambda_1 = 1 \tag{2.91}$$

$$q_2 = \begin{pmatrix} 1 \\ 0 \\ -1 \end{pmatrix}, \lambda_2 = \frac{5}{6} \tag{2.92}$$

$$q_3 = \begin{pmatrix} 1 \\ -2 \\ 1 \end{pmatrix}, \lambda_3 = \frac{1}{2} \tag{2.93}$$

and the decomposition of q_I is:

$$\begin{aligned} q_I &= \sum_{k=1}^{3} C_k q_k, \\ C_1 &= \frac{1}{3}\big[q_I(\pi^+) + q_I(\pi^0) + q_I(\pi^-)\big] \\ C_2 &= \frac{1}{2}\big[q_I(\pi^+) - q_I(\pi^-)\big] \\ C_3 &= -\frac{1}{3}q_I(\pi^0) + \frac{1}{6}\big[q_I(\pi^+) + q_I(\pi^-)\big]. \end{aligned} \tag{2.94}$$

Note that the matrix Q is normalized so that each column and row sums to one which means that the number of particles is constant. Hence, the largest eigenvalue λ_1 will be one and the corresponding eigenvector q_1 will be the only state surviving in a sufficiently large medium of length L (many rescatterings), because of the exponential decay law ($e^{-(1-\lambda)\kappa L}$), see subsection 2.3.5.

Using Eqs. (2.84) and (2.94) we find the following connection between the charge exchange matrix elements and the transition probabilities in Eq. (2.86):

$$\begin{aligned} A_p\,(1-c-d) &= \frac{1}{3}f(1) + \frac{1}{2}f(5/6) + \frac{1}{2}f(1/2) \\ A_p\,d &= \frac{1}{3}f(1) - \frac{1}{3}f(1/2) \\ A_p\,c &= \frac{1}{3}f(1) - \frac{1}{2}f(5/6) + \frac{1}{6}f(1/2). \end{aligned} \tag{2.95}$$

Finally, we get the results for matrix elements c, d and A_p from Eq. (2.95):

$$\begin{aligned} A_p &= g(W, Q^2)\, a, \\ c &= \frac{1}{3} - \frac{1}{2}\frac{f(5/6)}{f(1)} + \frac{1}{6}\frac{f(1/2)}{f(1)} \\ d &= \frac{1}{3}\left(1 - \frac{f(1/2)}{f(1)}\right), \end{aligned} \tag{2.96}$$

where $f(\lambda_k)$ denotes the transmission coefficient for the state with eigenvalue λ_k and $g(W, Q^2)$ is calculated explicitly in subsection 2.3.7.

2.3.5 Determination of the Function $f(\lambda)$

From now, we omit the index k for λ because it plays no role. As mentioned already in the previous subsections, $f(\lambda)$ contains the dynamics of the pion multiple scattering in the nucleus for the λ eigenvalues and can be interpreted as the expected number of pions which eventually escape from the nuclear medium either moving to the right (f_+) or to the left (f_-), normalized so that the integrated initial pion density is one. In order to calculate $f(\lambda)$, we assumed that all scattering into the forward hemisphere is along the forward direction and all scattering into the back hemisphere is along the same line in the backward direction. Therefore it is a one-dimensional scattering process. The expected number of pions to escape in either direction in the one-dimensional case is given by:

$$f(\lambda, L(b)) = f_+(\lambda, L(b)) + f_-(\lambda, L(b)). \tag{2.97}$$

Here, b is the impact parameter and $L(b)$ is the effective length where we have to average over $L(b)$ in the nucleus. It was shown that approximating the multiple-scattering with scattering in the forward and backward directions provides a very accurate approximation [30]. Thus what is important is the effective profile of the nucleus that the pions see. This allows to write:

$$f(\lambda) = \frac{\int_0^\infty \mathrm{d}b\, bL(b) f(\lambda, L(b))}{\int_0^\infty \mathrm{d}b\, bL(b)}, \tag{2.98}$$

where the effective length $L(b)$ is defined as:

$$L(b) = \frac{1}{\rho(0)} \int_{-\infty}^{+\infty} \mathrm{d}z\, \rho(\sqrt{z^2 + b^2})\ . \tag{2.99}$$

In the case of ${}_8O^{16}$, the effective length $L(b)$ is given by:

$$L(b) = R\sqrt{\pi} \exp\left(-b^2/R^2\right)\left(1 + C\left(\frac{1}{2} + \frac{b^2}{R^2}\right)\right)\ . \tag{2.100}$$

For ${}_{18}Ar^{40}$ and ${}_{26}Fe^{56}$ the effective length $L(b)$ is written as:

$$L(b) = \int_{-\infty}^{+\infty} \mathrm{d}z \, \frac{1}{1 + e^{\frac{\sqrt{z^2+b^2}-C}{C_1}}} \, . \tag{2.101}$$

In order to solve this integration we replace $z = bu$:

$$L(b) = 2\int_{0}^{+\infty} b\mathrm{d}u \, \frac{1}{1 + e^{\frac{b}{C_1}\sqrt{1+u^2}-\frac{C}{C_1}}} \tag{2.102}$$

and substitute the new variable $x = \frac{b}{C_1}\sqrt{1+u^2} - \frac{C}{C_1}$ in Eq. (2.102). After some calculations, we have the integration:

$$L(b) = 2C_1 \int_{\frac{b-C}{C_1}}^{+\infty} \mathrm{d}x \, \frac{x + \frac{C}{C_1}}{\sqrt{(x+\frac{C}{C_1})^2 - \frac{b^2}{C_1^2}}} \frac{e^{-x}}{1+e^{-x}}. \tag{2.103}$$

Since we can not integrate Eq. (2.98) directly, we calculate this numerically using the Laguerre integration from [60]. It is given by:

$$\int_{0}^{+\infty} e^{-x} f(x) dx = \sum_{i=1}^{n} \mathrm{w}_i f(x_i), \tag{2.104}$$

where $\mathrm{w_i}$ denotes the weight. Replacing the variable x by $x + x_0$ in Eq. (2.104) we get the following result:

$$\int_{x_0}^{+\infty} e^{-x} f(x) dx = e^{-x_0} \sum_{i=1}^{n} \mathrm{w}_i f(x_i + x_0), \tag{2.105}$$

Comparing the Eqs. (2.103) and (2.105) we can extract the following function $f(x)$ for our case:

$$f(x) = 2\,C_1 \, \frac{x + \frac{C}{C_1}}{\sqrt{(x+\frac{C}{C_1})^2 - \frac{b^2}{C_1^2}}} \frac{1}{1+e^{-x}} \tag{2.106}$$

and

$$f(x + x_0) = 2\,C_1 \, \frac{x + D}{\sqrt{x(x+D)}} \frac{1}{1 + e^{-(x+D-\frac{C}{C_1})}} \tag{2.107}$$

with $D = \frac{b}{C_1}$ and $x_0 = \frac{b-C}{C_1}$. Finally, the effective length for ${}_{18}Ar^{40}$ and ${}_{26}Fe^{56}$ is written in the following way:

$$L(b) = 2\,C_1 \sum_{i=1}^{n} \mathrm{w}_i \frac{x_i + D}{\sqrt{x_i(x_i+2D)}} \frac{e^{-(D-\frac{C}{C_1})}}{1+e^{-(x_i+D-\frac{C}{C_1})}}. \tag{2.108}$$

The numerical values for the x_i in Eq. (2.108) are taken from [60]. The other double integration in the denominator in Eq. (2.98) for ${}_{18}Ar^{40}$ and ${}_{26}Fe^{56}$ is carried out in appendix B.

The appropriate expression for the function $f(\lambda, L(b))$ has been derived in Ref. [30] both for the case of a one-dimensional multiple scattering problem and for the case of a spherical one. The two solutions have then been compared showing excellent agreement over the entire range of parameters. Therefore, in our case, we calculate $f(\lambda, L(b))$ adopting the approximate expression for the one-dimensional problem.

The solution of the one-dimensional problem of finding $f(\lambda, L(b))$ depends on the absorption and $\pi N\,(I = \frac{3}{2})$ elastic scattering cross sections, σ_{abs} and $\sigma_{\pi^+ p}$, respectively, obtained from experiment.

To describe $f(\lambda, L(b))$ we need the inverse interaction length κ and the direction reversal probability $\mu_\pm$. We assume that all pions are equal because the effects of the pion charges are contained already in the charge exchange matrix Q. For this reason, the pion-nucleon elastic scattering is taken by :

$$\sigma_{\pi N} = \frac{1}{3}\sigma_{\pi^+ p}. \tag{2.109}$$

Pions can be scattered and absorbed during their journey in the nucleus. We express this process in terms of the charge density connected with the inverse interaction length κ and the absorption and scattering cross sections in the following way:

$$\begin{aligned} \kappa &= \rho(0)\sigma_{tot}(W), \\ \sigma_{tot}(W) &= \sigma_{abs}(W) + \frac{1}{3}\sigma_{\pi^+ p}(W)\big[h_+(W) + h_-(W)\big], \end{aligned} \tag{2.110}$$

where:

$$\begin{aligned} h_+ &= \frac{1}{2}\int_0^{\frac{\pi}{2}} \mathrm{d}\phi\,(1 + 3\cos^2\phi)\sin\phi\, h(W,\phi) \\ h_- &= \frac{1}{2}\int_{\frac{\pi}{2}}^{\pi} \mathrm{d}\phi\,(1 + 3\cos^2\phi)\sin\phi\, h(W,\phi). \end{aligned} \tag{2.111}$$

For the cross sections σ_{abs} we used the first older parameterization (A) from [61]:

$$(A) : \sigma_{abs}(W) = \begin{cases} 0, & T_\pi < 110\,\mathrm{MeV}\ , \\ 22\,\mathrm{mb}\,\frac{T_\pi - 110\,\mathrm{MeV}}{290\,\mathrm{MeV}}, & T_\pi > 110\,\mathrm{MeV} \end{cases} \tag{2.112}$$

with the kinetic energy of the pion:

$$T_\pi = \frac{W^2 - (M_N + m_\pi)^2}{2M_N}.$$

A more recent parameterization (B) of σ_{abs} is given by [62]:

$$(B) : \sigma_{abs}(W) = \begin{cases} 30\,\text{mb}\,\frac{T_\pi}{200\,\text{MeV}}, & T_\pi < 200\,\text{MeV}, \\ 51.3\,\text{mb}\,(1 - \frac{T_\pi}{500\,\text{MeV}}), & 200\,\text{MeV} < T_\pi < 500\,\text{MeV}\ . \end{cases} \tag{2.113}$$

The elastic cross section for the πN scattering $\sigma_{\pi^+ p}$ is combined by the Δ resonance cross section and a constant non-resonant background:

$$\sigma_{\pi^+ p} = \sigma_{(3,3)}(W) + 20\,\text{mb}. \tag{2.114}$$

Using the Roper parameterization [63] we get the cross section $\sigma_{(3,3)}(W)$:

$$\sigma_{(3,3)}(W) = \sigma_{\max} \frac{q_r^2}{q^2} \frac{\frac{\Gamma^2}{4}}{(q^0 - q_r^0)^2 + \frac{\Gamma^2}{4}} \tag{2.115}$$

with

$$\begin{aligned} q_r^0 &= 1.921\, m_\pi, \\ q_r &= 1.640\, m_\pi\ , \\ \sigma_{\max} &= \frac{8\pi}{q_r^2} \approx 185\,\text{mb}\ , \\ q^0 &= \frac{W^2 - M_N^2 + m_\pi^2}{2W}\ , \\ q &= \sqrt{(q^0)^2 - m_\pi^2}, \\ \Gamma &= \frac{1.262\, q^3}{m_\pi (q^0 + q_r^0)(1 + 0.504 \frac{q^2}{m_\pi^2})}\ . \end{aligned} \tag{2.116}$$

The direction reversal probability $\mu_\pm$ can be derived from the projections $h_\pm$ of the pion-nucleon elastic cross section $\mathrm{d}\sigma_{\pi N}/\mathrm{d}\Omega$ in Eq. (2.72) on the forward- and backward-hemisphere of the Pauli factor $h(W, \phi)$:

$$\mu_\pm = \frac{1}{3} \sigma_{\pi^+ p}(W) \frac{h_\pm}{\sigma_{tot}}, \tag{2.117}$$

where $h_\pm$ is given in Eq. (2.111).

The Pauli factor in the pion-nucleon scattering $h(W, \phi)$ is given explicitly in section 2.3.7.

2.3.6 One Dimensional Multiple Scattering in Nuclei

We define the probability for a particle to transverse the distance $x-y$ in a medium with inverse interaction length κ as $e^{-\kappa(x-y)}$. The probability of interacting after that distance is $\kappa \mathrm{d}x$. Thus the combined probability of going from y to x and interacting in $\mathrm{d}x$ is given by:

$$\begin{aligned} P(x|y)\mathrm{d}x &= \kappa e^{-\kappa(x-y)}\mathrm{d}x, \quad x > y \\ &= \kappa e^{-\kappa(x-y)}\theta(x-y)\mathrm{d}x. \end{aligned} \tag{2.118}$$

In the following subsections we consider the forward and backward scattering and its special case, the only forward scattering.

Forward and Backward Scattering Case

For our multiple scattering problem we consider the probability $P(xj|yi)dx$, containing a pion which is after $n-1$ collisions at a place yi ($i = l$ (left), r (right)) and after n collision in an interval $\mathrm{d}x$ at x moving in the direction j. The four relevant probabilities are:

$$\begin{aligned} P(xr|yr) &= \mu_+ \kappa e^{-\kappa(x-y)}\theta(x-y)\ , \\ P(xl|yr) &= \mu_- \kappa e^{-\kappa(x-y)}\theta(x-y)\ , \\ P(xl|yl) &= \mu_+ \kappa e^{-\kappa(y-x)}\theta(y-x)\ , \\ P(xr|yl) &= \mu_- \kappa e^{-\kappa(y-x)}\theta(y-x) \end{aligned} \tag{2.119}$$

with the step function θ. We have also introduced the parameters $\mu_\pm$ denoting the probability that the scattering is forward or backward.

Since the composition laws for these probabilities correspond to the quantum mechanical composition laws for probability amplitudes we adopt the Dirac notation for the convenience as follows:

$$\begin{aligned} \langle xj|P|yi\rangle &= P(xj|yi) \\ \langle xj|P^2|yi\rangle &= \int_0^L \mathrm{d}z \sum_{k=r,l} \langle xj|P|zk\rangle\langle zk|P|yi\rangle \\ \langle xj|P^n|yi\rangle &= \int_0^L \mathrm{d}z \sum_{k=r,l} \langle xj|P|zk\rangle\langle zk|P^{n-1}|yi\rangle. \end{aligned} \tag{2.120}$$

To evaluate the magnitude $N^{(n)}$ we defined $\rho^{(0)}(yi)$ as the initial pion density at the position y in direction i. Therefore, the pion density $\rho^{(n)}(xj)$ at the position x in direction j after n-collisions is given by:

$$\rho^{(n)}(xj) = \int_0^L \mathrm{d}y \sum_{i=r,l} \langle xj|P^n|yi\rangle \rho^{(0)}(yi), \tag{2.121}$$

where the initial pion density $\rho^{(0)}(yi)$ is normalized to one:

$$\rho^{(0)}(yi) = \frac{1}{L}\delta_{i,r}. \tag{2.122}$$

The number of pions $N^{(n)}$, which escape the medium after n-interactions, is equal to the pion number, which exist in medium after n-interactions minus the number of such pions, which interact once more in the medium. Then, the pion number $N^{(n)}$ is:

$$\begin{aligned} N^{(n)} &= \int_0^L \mathrm{d}x(\rho^{(n)}(xr) + \rho^{(n)}(xl)) \\ &\quad - \int_0^L \mathrm{d}x\Big(\int_0^x \mathrm{d}z\kappa e^{-\kappa(x-z)}\rho^{(n)}(xl) + \int_x^L \mathrm{d}z\kappa e^{-\kappa(z-x)}\rho^{(n)}(xr)\Big). \end{aligned} \tag{2.123}$$

A more compact notation for Eqs. (2.119)–(2.123) is introduced by:

$$\begin{aligned} \langle zi|xj\rangle &= \delta(z-x)\delta_{ij}\ , \\ \langle z|P_{tot}|xr\rangle &= \kappa e^{-\kappa(z-x)}\theta(z-x)\ , \\ \langle z|P_{tot}|xl\rangle &= \kappa e^{-\kappa(x-z)}\theta(x-z)\ . \end{aligned} \tag{2.124}$$

We rewrite the Eqs. (2.121)–(2.123) using this compact notation and insert Eq. (2.123) into Eq. (2.81):

$$\begin{aligned} f(\lambda, L(b)) &= \sum_{n=0}^{\infty} \lambda^n N^{(n)} \\ &= \frac{1}{L}\int_0^L \int_0^L \int_0^L \mathrm{d}x\mathrm{d}y\mathrm{d}z \langle xj|(1-\lambda P)^{-1}|yr\rangle \times \\ &\quad \big[\big(\delta(z-x) - \langle z|P_{tot}|xl\rangle\big) + \big(\delta(z-x) - \langle z|P_{tot}|xr\rangle\big)\big], \end{aligned} \tag{2.125}$$

where the following identity has been used:

$$\sum_{n=0}^{\infty} \lambda^n \rho^{(n)}(xj) = \frac{1}{L}\int_0^L \mathrm{d}y \langle xj| \sum_{n=0}^{\infty} \lambda^n P^n |yr\rangle$$

$$= \frac{1}{L}\int_0^L \mathrm{d}y\langle xj|(1-\lambda P)^{-1}|yr\rangle \tag{2.126}$$

with $j = r, l$. Furthermore, we can simplify Eq. (2.125) as:

$$\begin{aligned}\delta(z-x) - \langle z|P_{tot}|xj\rangle &= (1-\frac{1}{\sigma_+ + \sigma_-})\sum_{i=r,l}\langle zi|xj\rangle \\ &\quad + \frac{1}{\sigma_+ + \sigma_-}\sum_{i=r,l}\langle zi|(1-\lambda P)|xj\rangle \end{aligned}\tag{2.127}$$

with $\sigma_\pm = \lambda\mu_\pm$. After substituting Eq. (2.127) into Eq. (2.125) we obtain:

$$\begin{aligned} f(\lambda, L(b)) &= \frac{1}{L}\sum_{j=r,l}\int_0^L\int_0^L\int_0^L \mathrm{d}x\mathrm{d}y\mathrm{d}z\langle xj|(1-\lambda P)^{-1}|yr\rangle \times \\ &\quad \big[\delta(z-x) - \langle z|P_{tot}|xj\rangle\big] \\ &= \frac{1}{L}\sum_{j=r,l}\sum_{i=r,l}\int_0^L\int_0^L\int_0^L \mathrm{d}x\mathrm{d}y\mathrm{d}z\big[\langle xj|(1-\lambda P)^{-1}|yr\rangle \times \\ &\quad (1-\frac{1}{\sigma_+ + \sigma_-})\delta(z-x)\delta_{ij} + \frac{1}{\sigma_+ + \sigma_-}\langle zi|(1-\lambda P)|xj\rangle \times \\ &\quad \langle xj|(1-\lambda P)^{-1}|yr\rangle\big] \end{aligned}\tag{2.128}$$

with

$$\begin{aligned}\sum_{i=r,l}\langle zi|yr\rangle &= \sum_{j=r,l}\sum_{i=r,l}\int_0^L \mathrm{d}x\langle zi|(1-\lambda P)|xj\rangle\langle xj|(1-\lambda P)^{-1}|yr\rangle \\ &= \int_0^L \mathrm{d}z\delta(z-y). \end{aligned}\tag{2.129}$$

Finally, substituting Eq. (2.129) into Eq. (2.128) $f(\lambda, l(b))$ is obtained as follows:

$$f(\lambda, l(b)) = (1-\frac{1}{\sigma_+ + \sigma_-})\langle(1-\lambda P)^{-1}\rangle_{av} + \frac{1}{\sigma_+ + \sigma_-}, \tag{2.130}$$

where the averaged inverse operator $\langle(1-\lambda P)^{-1}\rangle_{av}$ is defined as:

$$\langle(1-\lambda P)^{-1}\rangle_{av} = \frac{1}{L}\sum_{i=r,l}\int_0^L\int_0^L \mathrm{d}y\mathrm{d}z\langle zi|(1-\lambda P)^{-1}|yr\rangle. \tag{2.131}$$

In order to obtain the inverse operator we make an ansatz in the following way:

$$\langle zi|(1-\lambda P)^{-1}|yj\rangle = \delta(z-y)\delta_{ij} + F(zi|yj), \tag{2.132}$$

where $f(yj)$ is defined by:

$$f(yj) = \sum_{i=r,l} \int_0^L \mathrm{d}z F(zi|yj). \tag{2.133}$$

With this ansatz we have the expression of the inverse operator (2.131) in the following way:

$$\begin{aligned} \langle (1-\lambda P)^{-1} \rangle_{av} &= 1 + \frac{1}{L} \int_0^L \mathrm{d}y f(yr) \\ &= 1 + \frac{1}{L} \int_0^L \mathrm{d}y f(yl). \end{aligned} \tag{2.134}$$

Therefore the evaluation of $f(\lambda, L(b))$ is reduced to the calculation of $f(yj)$. We obtain $f(yj)$ using the identity in Eq. (2.129):

$$\begin{aligned} \int_0^L \mathrm{d}z \delta(z-y) &= \int_0^L \mathrm{d}z \Big\{ \sum_{i=,r,l} \sum_{j=r,l} \int_0^L \mathrm{d}x \langle zi|(1-\lambda P)^{-1}|xj\rangle\langle xj|(1-\lambda P)|yk\rangle \Big\} \\ &= \int_0^L \mathrm{d}z \Big\{ \sum_{i=,r,l} \sum_{j=r,l} \int_0^L \mathrm{d}x \big[(\delta_{ij}\delta(z-x) + F(zi|yj))(\delta_{jk}\delta(x-y) \\ &\quad - \langle xj|\lambda P|yk\rangle) \big] \Big\} \\ \to 1 &= \sum_{i=r,l} \int_0^L \mathrm{d}z \Big\{ \delta(z-y)\delta_{ik} + F(zi|yk) - \langle zi|\lambda P|yk\rangle \\ &\quad - \sum_{j=r,l} \int_0^L \mathrm{d}x F(zi|xj)\langle xj|\lambda P|yk\rangle \Big\} \\ \to 1 &= 1 + f(yk) - g(yk) - \sum_{j=r,l} \int_0^L \mathrm{d}x f(xj)\langle xj|\lambda P|yk\rangle \ . \end{aligned} \tag{2.135}$$

This relation implies that $f(yk)$ satisfies the following integral equation:

$$f(yk) = g(yk) + \sum_{i=r,l} \int_0^L \mathrm{d}z f(zi)\langle zi|\lambda P|yk\rangle \tag{2.136}$$

with

$$g(yk) \equiv \sum_{i=r,l} \int_0^L \mathrm{d}z \langle zi|\lambda P|yk\rangle. \tag{2.137}$$

It is very useful to consider the reflection symmetry to solve the integration in Eq. (2.137). This symmetry is obtained when we go back to Eq. (2.119) for $P(xi|yj)$ and substitute $z \to L - y$ in (2.137):

$$f(yr) = f((L-y)l),$$

$$\begin{aligned} f(yl) &= f((L-y)r), \\ g(yr) &= g((L-y)l), \\ g(yl) &= g((L-y)r). \end{aligned} \tag{2.138}$$

Using the symmetry and substituting Eq. (2.119) into Eq. (2.137), we get a single integral equation:

$$f(yl) = \underbrace{(\sigma_+ + \sigma_-)(1 - e^{-\kappa y})}_{g(yl)} + \int_0^y \mathrm{d}z \big[\kappa\sigma_+ f(zl) + \kappa\sigma_- f((L-z)l)\big] e^{-\kappa(y-z)}. \tag{2.139}$$

Evaluating $e^{-\kappa x}\big[\frac{\mathrm{d}}{\mathrm{d}y}(e^{\kappa y} f(yl))\big]$ one finds the following differential equation:

$$\kappa f(yl) + f'(yl) = (\sigma_+ + \sigma_-)\kappa + \kappa\sigma_+ f(yl) + \kappa\sigma_- f((L-y)l) \tag{2.140}$$

with the boundary condition $f(0l) = 0$. The solution of this differential equation consists of two parts, a homogeneous and an inhomogeneous solution:

$$f(yl) = \frac{\sigma_+ + \sigma_-}{1 - (\sigma_+ + \sigma_-)}\Big[1 - \frac{h(y)}{h(0)}\Big]. \tag{2.141}$$

The first term (inhomogeneous solution) in (2.141) cancels the $\kappa(\sigma_+ + \sigma_-)$ and the remaining terms (homogeneous part) give the equation:

$$\begin{aligned} -\kappa\frac{h(y)}{h(0)} - \frac{h'(y)}{h(0)} &= -\kappa\sigma_+\frac{h(y)}{h(0)} - \kappa\sigma_-\frac{h(L-y)}{h(0)} \\ \Rightarrow \kappa h(y) + h'(y) &= \kappa\sigma_+ h(y) + \kappa\sigma_- h(L-y). \end{aligned} \tag{2.142}$$

In order to solve (2.142) we take the exponential ansatz:

$$h(y) = e^{\kappa\sigma y} + \mu e^{-\kappa\sigma y}. \tag{2.143}$$

With this ansatz we find the following solution:

$$\begin{aligned} \sigma &= \sqrt{(1-\sigma_+)^2 - \sigma_-^2}, \\ \mu &= \frac{\sigma + 1 - \sigma_+}{\sigma_-} e^{\kappa\sigma L}. \end{aligned} \tag{2.144}$$

In order to obtain the exact expression of $\langle(1-\lambda P)^{-1}\rangle_{av}$ in (2.134) we substitute Eq. (2.141) into Eq. (2.134) and find the following results for $f(\lambda, L(b))$ in Eq. (2.130):

$$f(\lambda, L(b)) = f_+(\lambda, L(b)) + f_-(\lambda, L(b))$$

$$= \frac{e^{\kappa\sigma L}-1}{\kappa\sigma L}\frac{1+\mu e^{-\kappa\sigma L}}{1+\mu}. \tag{2.145}$$

The expected numbers $f_\pm(\lambda, L(b))$ of pions emerging from the medium either moving to the right (no over-all direction reversal) or to the left (over-all direction reversal) are obtained when $f(\lambda, L(b))$ is regarded as a function of the direction-reversal probability μ_-. Only even powers of $(\mu_-)^n$ to $f_+(\lambda, L(b))$ and odd powers to $f_-(\lambda, L(b))$ can contribute in the summation over n. Therefore we have the following relations:

$$\begin{aligned} f(\mu_-, L(b)) &= f_+(\mu_-, L(b)) + f_-(\mu_-, L(b)), \\ f(-\mu_-, L(b)) &= f_+(-\mu_-, L(b)) - f_-(-\mu_-, L(b)). \end{aligned} \tag{2.146}$$

From this it follows directly:

$$\begin{aligned} f_+(\lambda, L(b)) &= \frac{f(\mu_-, L(b)) + f(-\mu_-, L(b))}{2} \\ &= \frac{e^{\kappa\sigma L}-1}{\kappa\sigma L}\frac{\mu^2 e^{-\kappa\sigma L}-1}{\mu^2-1}, \\ f_-(\lambda, L(b)) &= \frac{f(\mu_-, L(b)) - f(-\mu_-, L(b))}{2} \\ &= \frac{e^{\kappa\sigma L}-1}{\kappa\sigma L}\frac{\mu(1-e^{-\kappa\sigma L})}{\mu^2-1}. \end{aligned} \tag{2.147}$$

We discuss the case $\sigma_\pm = 0$ in appendix C.

Scattering Only in the Forward Direction

We discuss in this subsubsection the forward scattering case, i.e. $\mu_- = 0$, $\sigma_- = 0$ and $\mu_+ = 1$ as a check on the forward and backward scattering and start with an interaction whose inverse interaction length is κ and thus $P(x|y) = \kappa e^{-\kappa(x-y)}\theta(x-y)$ is probability of going from y to x and interaction at x with charge exchange λ.

In order to obtain the inverse operator $\langle x|(1-\lambda P)^{-1}|y\rangle$ we use the following identity from the previous subsubsection

$$\delta(x-y) = \int_0^L \mathrm{d}z \langle x|(1-\lambda P)^{-1}|z\rangle\langle z|(1-\lambda P)|y\rangle. \tag{2.148}$$

Substituting the ansatz for the inverse operator: $\langle x|(1-\lambda P)^{-1}|z\rangle \equiv \delta(x-z) + F(x|z)$ with $F(x|z) = 0$ for $z > x$ into (2.148) we obtain the following result:

$$\delta(x-y) = \int \mathrm{d}z\big[\delta(x-z) + F(x|z)\big]\big[\delta(z-y) - \lambda\kappa e^{-\kappa(z-y)}\theta(z-y)\big]$$

$$\Rightarrow F(x|y) = \lambda\kappa e^{-\kappa(x-y)} + \lambda\kappa \int_y^x \mathrm{d}z F(x|z) e^{-\kappa(x-y)}. \tag{2.149}$$

$F(x|y)$ is rewritten as follows:

$$\begin{aligned} F(x|y) &= \lambda\kappa e^{\kappa y}\big[e^{-\kappa x} + \int_y^x \mathrm{d}z F(x|z) e^{-\kappa z}\big] \\ &= \lambda\kappa e^{\kappa y} g(x|y) \end{aligned} \tag{2.150}$$

with the definition:

$$g(x|y) = \big[e^{-\kappa x} + \lambda\kappa \int_y^x \mathrm{d}z g(x|z)\big]. \tag{2.151}$$

For $x = y$ the integral vanishes and $g(x|x) = e^{-\kappa x}$. We take an ansatz of $g(x|y)$ in the following way:

$$g(x|y) = e^{-\alpha y} e^{-\beta x} = e^{-\alpha y - (\kappa-\alpha)x}, \tag{2.152}$$

because $\alpha + \beta = \kappa$ due to $g(x|x) = e^{-\kappa x}$. Using this, $F(x|y)$ from Eq. (2.150) is expressed by:

$$F(x|y) = \lambda\kappa e^{(\lambda-1)\kappa(x-y)} \tag{2.153}$$

with the substitution $\alpha = \lambda\kappa$. Thus, the inverse operator is obtained as follows:

$$\langle x|(1-\lambda P)^{-1}|y\rangle = \delta(x-y) + \lambda\kappa e^{(\lambda-1)\kappa(x-y)}. \tag{2.154}$$

After integrating this equation the final result for the inverse operator gives:

$$\langle (1-\lambda P)^{-1}\rangle_{av} = 1 + \frac{\lambda}{\lambda-1}(e^{(\lambda-1)\kappa L} - 1). \tag{2.155}$$

Finally, $f_+(\lambda, L(b))$ from Eq. (2.130) is:

$$\begin{aligned} f_+(\lambda, L(b)) &= (1-\frac{1}{\lambda})\Big[1 + \frac{\lambda}{\lambda-1}(e^{(\lambda-1)\kappa L} - 1)\Big] + \frac{1}{\lambda} \\ &= e^{-(1-\lambda)\kappa L}. \end{aligned} \tag{2.156}$$

We find that the effect of the multiple scattering is to produce an effective interaction constant $(1-\lambda)\kappa$. This is the complete modification from multiple scattering.

The last expression makes sense because for $\lambda = 1$ is $f_+(\lambda, L(b)) = 1$, i.e. the particles just all come out, and for $\lambda < 1$ is $f_+(\lambda, L(b)) < 1$ and for $L \to \infty$ is $f_+(\lambda, L(b)) \to 0$, i.e. after infinite many rescattering they all go to the $\lambda = 1$ state.

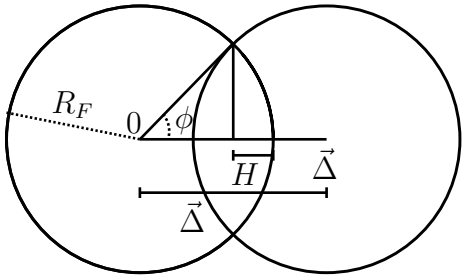

Figure 2.15: Fermi spheres in phase space: The segment of nucleons which can contribute, for given momentum transfer $\vec{\Delta}$ to the nucleus, is the fraction of the volume of a Fermi sphere of radius R_F centered at 0 which lies outside a second sphere of radius R_F centered at $\vec{\Delta}$. H, ϕ denote the height and the angle, respectively. The overlapped region denotes the forbidden volume (FV) due to the Pauli principle.

2.3.7 Pauli Factors

In order to calculate the Pauli factor we use the simple Fermi gas model. It assumes that the nucleons in the nucleus form a gas of weakly interacting fermions. In the ground state of the system the nucleons fill all energy states (labeled by the momentum) within the Fermi sphere with Fermi momentum R_F. Due to the Pauli exclusion principle an excited nucleon necessarily needs to have a momentum outside the Fermi sphere, since all states inside the sphere are already occupied. The radius of the Fermi sphere is from [64] and reads:

$$R_F = R_p = R_n \approx 1.6 m_\pi. \tag{2.157}$$

Then, the segment of nucleons which can contribute, for given momentum transfer $\vec{\Delta}$ to the nucleus, is the fraction of the volume of a Fermi sphere of radius R_F centered at 0 which lies outside a second sphere of radius R_F centered at $\vec{\Delta}$. Due to the Pauli principle $\vec{\Delta}$ should not overlap the two spheres in phase space. The forbidden (overlapped) region corresponds to two times the volume of a sphere fraction with the radius R_F and the height H. The so-called forbidden volume (FV) in Fig. 2.15 is:

$$\begin{aligned} FV &= 2\Big[\frac{1}{3}\pi H^2(3R_F - H)\Big] \\ &= \frac{4}{3}\pi R_F^3\Big[1 - \frac{3|\vec{\Delta}|}{4R_F} + \frac{|\vec{\Delta}|^3}{16R_F^3}\Big], \end{aligned} \tag{2.158}$$

where $H = R_F - \frac{|\vec{\Delta}|}{2} = R_F(1-\cos\phi)$. Then, the Pauli factor h is defined as the fraction of the allowed phase space referred to the whole volume $\frac{4\pi R^3}{3}$:

$$h(\eta) = \begin{cases} \frac{3}{4}\eta - \frac{1}{16}\eta^3, & \eta < 2 \\ 1, & \eta \geq 2 \end{cases} \tag{2.159}$$

with

$$\eta = \frac{|\vec{\Delta}|}{R_F} \approx \frac{2q}{R_F}\sin(\frac{\phi}{2}). \tag{2.160}$$

Pauli Production Factor $g(W, Q^2)$

Inspecting Fig. 2.2, the momentum transfer $\vec{\Delta} := \vec{p}_{N'} - \vec{p}_N$ is given in the $\pi N'$-CMS by $\vec{\Delta} = \vec{q} - \vec{p}_\pi$. In order to facilitate the comparison with the literature [30] we adopt the following notation: $\vec{q} \to \vec{k}$, $\vec{p}_\pi \to \vec{q}$, i.e. $\vec{\Delta} = \vec{k} - \vec{q}$. It is easy to derive the following expressions for these momenta in the $\pi N'$-CMS in dependence of W and Q^2:

$$\begin{aligned} k^0 &= \frac{W^2 - M_N^2 - Q^2}{2W}, \\ k &\equiv |\vec{k}| = \sqrt{(k^0)^2 + Q^2} \end{aligned} \tag{2.161}$$

$$\begin{aligned} q^0 &= \frac{W^2 - M_N^2 + m_\pi^2}{2W}, \\ q &\equiv |\vec{q}| = \sqrt{(q^0)^2 - m_\pi^2}\ , \end{aligned} \tag{2.162}$$

where the latter two equations can also be found in Eq. (2.116).

To calculate the Pauli production factor $g(W, Q^2)$ we average the Pauli factor $h(\eta)$ over the solid angle as follows:

$$g(W, Q^2) = \frac{\int \mathrm{d}\Omega\, h(\eta)}{\int \mathrm{d}\Omega} = \frac{R_F^2}{2\ q\ k}\int_{\eta(+1)}^{\eta(-1)} \mathrm{d}\eta\, \eta\, h(\eta), \tag{2.163}$$

where $\eta = \eta(\cos\phi)$. We distinguish the following three cases for the integration in Eq. (2.163):

$$\begin{aligned} &(1) \quad \eta(-1) > \eta(+1) \geq 2 \quad \longleftrightarrow \quad 2R_F \leq k - q, \\ &(2) \quad \eta(+1) < \eta(-1) \leq 2 \quad \longleftrightarrow \quad 2R_F \geq k + q, \\ &(3) \quad \eta(+1) \leq 2 \leq \eta(-1) \quad \longleftrightarrow \quad k - q \leq 2R_F \leq k + q, \end{aligned} \tag{2.164}$$

resulting in:

$$g(W,Q^2)=\begin{cases}1, & 2R_F\le k-q,\\ \frac{1}{2k}\left[\frac{3k^2+q^2}{2R_F}-\frac{5k^4+q^4+10k^2q^2}{40R_F^3}\right], & k+q\le 2R_F,\\ \frac{1}{4qk}\left[(q+k)^2-\frac{4}{5}R_F^2-\frac{(k-q)^3}{2R_F}+\frac{(k-q)^5}{40R_F^3}\right], & k-q\le 2R_F\le k+q\ .\end{cases} \tag{2.165}$$

Pauli Factors in the πN Scattering

Since the approximation (2.160) is not doing well in the case $\eta\approx 2$, i.e. $h(\eta)\approx 1$, we take the invariant mass W as follows:

$$W^2=2m_N E_\pi+m_N^2+m_\pi^2. \tag{2.166}$$

Performing the integration Eq. (2.111) we get:

$$\begin{aligned}
\alpha\le 1, \quad & \begin{cases} h_+=\alpha\frac{1}{\sqrt{2}}\frac{59}{70}-\alpha^3\frac{1}{\sqrt{2}}\frac{29}{420}\\ h_-=\alpha\frac{136-59\sqrt{2}}{70}-\alpha^3\frac{176-29\sqrt{2}}{420}\end{cases}\\
1\le\alpha\le\sqrt{2}, \quad & \begin{cases} h_+=\alpha\frac{1}{\sqrt{2}}\frac{59}{70}-\alpha^3\frac{1}{\sqrt{2}}\frac{29}{420}\\ h_-=2-\alpha^{-2}\frac{4}{5}+\alpha^{-4}\frac{18}{35}-\alpha^{-6}\frac{4}{21}-\alpha\frac{1}{\sqrt{2}}\frac{59}{70}+\alpha^3\frac{1}{\sqrt{2}}\frac{29}{420}\end{cases}\\
\sqrt{2}\le\alpha, \quad & \begin{cases} h_+=1-\alpha^{-2}\frac{4}{5}+\alpha^{-4}\frac{18}{35}-\alpha^{-6}\frac{4}{21}\\ h_-=1\end{cases}
\end{aligned} \tag{2.167}$$

with

$$\alpha=\frac{q}{R_F}. \tag{2.168}$$

2.3.8 Averaging Approximation

It is important to notice that, while the Pauli production factor depends on both W and Q^2, the function $f(\lambda)$ depends only on W and this dependence is very weak. Therefore, as it has been already verified in Ref. [30], it is reasonable to average the charge exchange

parameters over the leading W-dependence by defining an averaged function $\bar{f}(\lambda)$ in the following way:

$$\bar{f}(\lambda) = \frac{\int \mathrm{d}W\, q(W)^{-1}\sigma_{3,3}(W) f(\lambda)}{\int \mathrm{d}W\, q(W)^{-1}\sigma_{3,3}(W)}, \tag{2.169}$$

where $\sigma_{3,3}(W)$ is the pion-nucleon scattering cross section and $q(W)$ is the pion momentum. For the definitions of $\sigma_{3,3}(W)$ and $q(W)$ see subsection 2.3.5.

2.3.9 Results

Using the model outlined in the previous subsections, we evaluated the nuclear corrections for leptonic pion production on three different nuclei: oxygen, argon and iron. As described in the previous sections, the nuclear corrections are based on three effects: absorption, charge exchange and the Pauli factor. In the following we examine the importance of these three contributions to the nuclear corrections. Furthermore, in order to estimate the uncertainties due to the theoretical description of absorption effects we compare the two different models given in Eq. (2.112) (model (A)) and Eq. (2.113) (model (B)). Note that throughout this thesis all results (all figures, Table 2.2) have been calculated using model (A) if not stated otherwise.

In Table 2.2 the average charge exchange parameters $\bar{f}(\lambda)$ are listed for the three different targets. As expected the values of $\bar{f}(\lambda)$ are smaller for heavier targets in accordance with the expectation that charge exchange and absorption are larger in heavier targets. Note, however, that $\bar{f}(\lambda)$ depends on the charge exchange and the absorption in a non-trivial manner as can be seen by inspecting subsections 2.3.5 and 2.3.6 and Eq. (2.169).

${}_ZT^A$	$\bar{f}(1/2)$	$\bar{f}(5/6)$	$\bar{f}(1)$
${}_8O^{16}$	0.418	0.587	0.811
${}_{18}Ar^{40}$	0.284	0.420	0.648
${}_{26}Fe^{56}$	0.261	0.393	0.625

Table 2.2: $\bar{f}(\lambda)$ with $\lambda = 1/2, 5/6$ and 1 for ${}_8O^{16}$, ${}_{18}Ar^{40}$ and ${}_{26}Fe^{56}$.

In order to disentangle charge exchange effects from absorption effects and the dependence on the absorption model we have calculated $\bar{f}(\lambda)$ for an oxygen target for three different scenarios, see Table 2.3: no absorption, absorption model (A) and model (B)

(always including charge exchange and the Pauli factor). that the values of $\bar{f}(\lambda)$ with absorption (B) are considerably smaller than in the case of absorption (A). Furthermore, $\bar{f}(1)$ is affected by the absorption (A) by about 20%.

${}_8O^{16}$	all nucl. corr. no absorption	all nucl. corr. absorption (A)	all nucl. corr. absorption (B)
$\bar{f}(1/2)$	0.448	0.418	0.346
$\bar{f}(5/6)$	0.659	0.587	0.439
$\bar{f}(1)$	1.0	0.811	0.523

Table 2.3: $\bar{f}(\lambda)$ with $\lambda = 1/2$, 5/6 and 1 for ${}_8O^{16}$ without absorption, with absorption (A) and (B), separately.

Next we show in Table 2.4 the Q^2-dependence of the Pauli factor $g(W, Q^2)$ at fixed $W = 1.2$ GeV which is independent of the nuclear target and the absorption. As can be seen, the reduction of the cross section due to the Pauli exclusion principle is smaller for larger values of Q^2 since more phase space is available. Eventually at $Q^2 = 0.35$ GeV^2 there is no more reduction of the cross section due to the Pauli exclusion principle

Q^2	$g(1.2\,\mathrm{GeV}, Q^2)$
0.00	0.825
0.05	0.888
0.10	0.931
0.15	0.960
0.20	0.978
0.25	0.989
0.30	0.996
0.35	1.000
0.40	1.000

Table 2.4: Pauli production factor $g(W, Q^2)$ in dependence of Q^2 evaluated at fixed $W = 1.2\,\mathrm{GeV}$.

The charge exchange matrices M for oxygen, argon and iron are given by [3]:

$$M({}_8O^{16}) = A_p \begin{pmatrix} 0.782 & 0.161 & 0.057 \\ 0.161 & 0.677 & 0.161 \\ 0.057 & 0.161 & 0.782 \end{pmatrix} \tag{2.170}$$

$$M({}_{18}Ar^{40}) = A_p \begin{pmatrix} 0.731 & 0.187 & 0.082 \\ 0.187 & 0.625 & 0.187 \\ 0.082 & 0.187 & 0.731 \end{pmatrix} \tag{2.171}$$

$$M({}_{26}Fe^{56}) = A_p \begin{pmatrix} 0.718 & 0.194 & 0.088 \\ 0.194 & 0.612 & 0.194 \\ 0.088 & 0.194 & 0.718 \end{pmatrix} . \tag{2.172}$$

As can be seen, the dominant entries are on the main diagonal and decrease (more charge exchange!) with increasing target mass. An example of how to utilize the charge exchange matrices M, a detailed calculation and discussion of the ratio $r = (\sigma(\pi^+) + \sigma(\pi^-))/\sigma(\pi^0)$ of charged current cross sections for propane and halon targets utilized by the CERN Gargamelle experiment [65], can be found in appendix D.

The Pauli factor and the charge exchange matrix M for oxygen have been compared with the corresponding quantities previously evaluated in Refs. [30, 40, 41] and have been found to be in good agreement with each other. Unfortunately, no comparison with previous calculations or experimental data is possible for argon and iron.

To study the effects of absorption we plotted in Fig. 2.16 total cross sections (more precisely the dominant resonance contributions) for CC (anti-)neutrino scattering off oxygen targets. Figs. 2.16 a) and b) deal with π^+ and π^0 production, respectively, in ν scattering. Note that no negatively charged pions are produced in neutrino (free) nucleon scattering. Of course, due to charge exchange effects in nuclei also a small fraction of π^- is generated which we do not plot here. Figs. 2.16 c) considers the case of π^- production in $\bar{\nu}$ scattering. Again curves for the subdominant π^0 and π^+ production are not shown. In each figure the solid, dashed, dash-dotted, thick and thin dotted lines represent respectively the cross sections including nuclear corrections except absorption, including all nuclear corrections utilizing absorption model (A) and (B), taking into account only the Pauli production factor g, and neglecting any nuclear corrections. Note that the solid curves

[3] As can be inferred from Eq. (2.84) the charge exchange matrices M exhibit a high degree of symmetry. (The values in each row and column add up to 1 and M is symmetric w.r.t. to both diagonals.)

have been calculated using modified charge exchange matrices which can be calculated with help of the matrices including absorption effects according to model (A) given in Eq. (2.170) and Table 2.2. One can make the following observations:

- The reduction of the free cross section due to the Pauli factor is very small.
- The charge exchange effect reduces the dominant free cross sections (π^+ in neutrino production, π^- in anti-neutrino production) by about 25-30%. On the other hand, the smaller cross sections (π^0, π^- in ν scattering and π^0, π^+ in $\bar{\nu}$ scattering) are enlarged due to the charge exchange. The π^0 cross section shown in Fig. 2.16 b) is increased by about 30% taking into account nuclear corrections.
- The absorption effect leads to a further reduction of roughly 10-15% model (A) and 40% model (B) in the $\pi^\pm$ case. In the π^0 case we find a reduction of about 30% in model (A) and 50 % in model (B).
- Finally, the total nuclear effect in the $\pi^\pm$ cases can be as large as 40 to 60% depending on the absorption model. In the π^0 case the charge exchange and absorption effect compensate each other resulting in almost no reduction employing model (A) and a decrease of about 25% in case of model (B).

Note that Merenyi et. al. [66] give a best fit for the effective pion absorption and charge exchange probabilities:

$$\begin{aligned} P_\pi(\text{absorption}) &= 0.22 \pm 0.05 \\ P_\pi(\text{charge exchange}) &= 0.10 \pm 0.08. \end{aligned}$$

The difference to our values can be partly understood if one notices that this group assumed that each pion undergoes only either a charge exchange or an absorption process whereas we consider both cases simultaneously.

Finally, we turn to the neutral current case. The differential cross sections, evaluated in sec. 2.2 for free nucleon targets, have been used here together with the charge exchange matrix M to obtain the differential cross sections for nuclear targets. These cross sections have been integrated over W and Q^2 keeping the neutrino energy fixed at 1 GeV in order to obtain the pion energy spectra appearing in Figs. 2.17–2.19.

Fig. 2.17 displays the pion energy distributions for positive, neutral and negative pions for NC neutrino scattering produced on oxygen targets. In each figure the solid line

represents the initial distribution without any nuclear correction, the dashed line represents the same distribution after the application of the Pauli factor in the production, and the dotted line represents the final distribution after applying all the nuclear corrections discussed in the previous subsections. Similarly, Fig. 2.18 and Fig. 2.19 display the corresponding pion distributions produced on argon and iron targets, respectively.

From these figures it is clear that, while the reduction of the cross section due to the Pauli production factor is the same for all the processes investigated in this thesis, the nuclear corrections related to the pion charge exchange and pion absorption are larger for neutral pions than for the positive or negative ones. Furthermore, these corrections turn out to be larger for heavier nuclei. Finally, the magnitude of the nuclear corrections decreases with increasing pion energy.

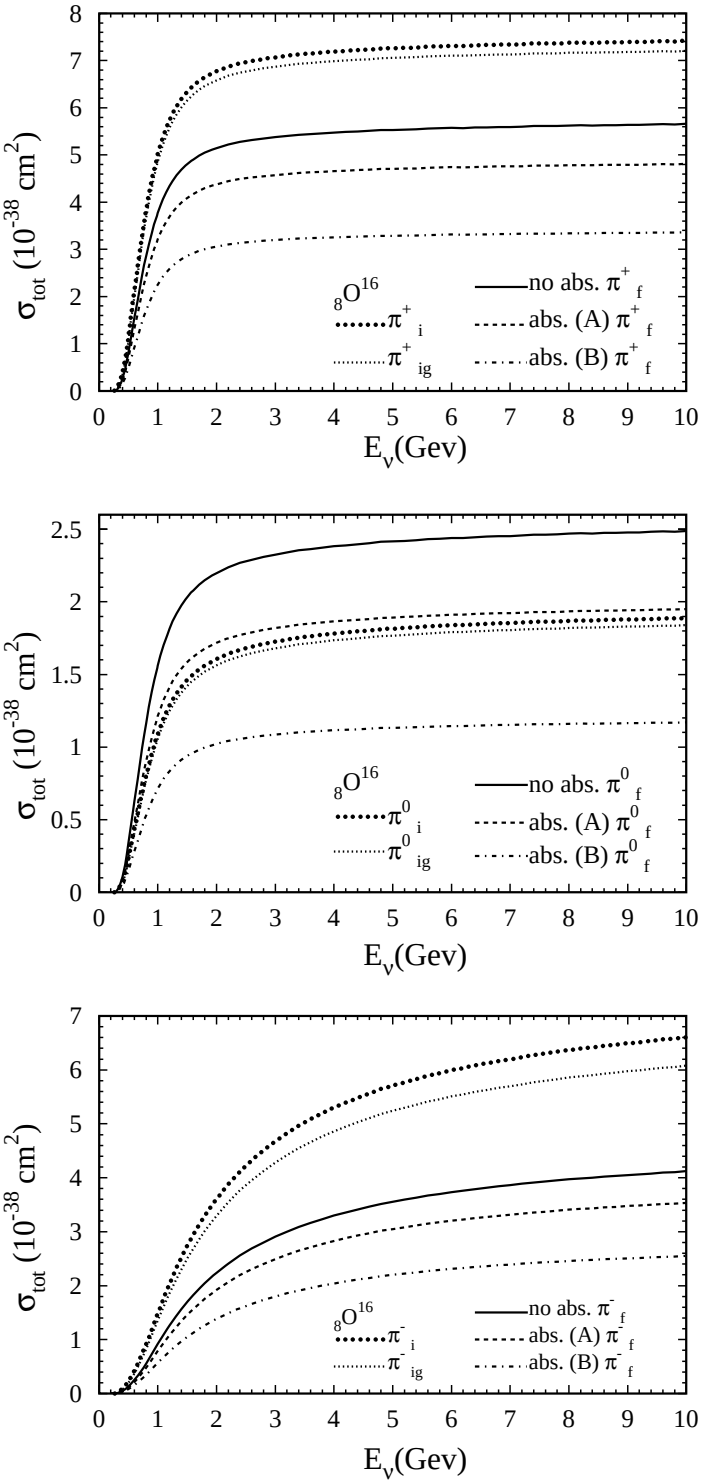

Figure 2.16: Total cross sections (resonance contributions) in CC (anti-)neutrino scattering off oxygen targets. Shown are in a) and b) cross sections for π^+ and π^0 production in ν scattering and in c) the cross sections for π^- production in $\bar{\nu}$ scattering. The solid, dashed, dash-dotted, thick and thin dotted lines represent, respectively, the cross sections including nuclear corrections except absorption, including all nuclear corrections utilizing absorption model (A) and (B), taking into account only the Pauli production factor g, and neglecting any nuclear corrections.

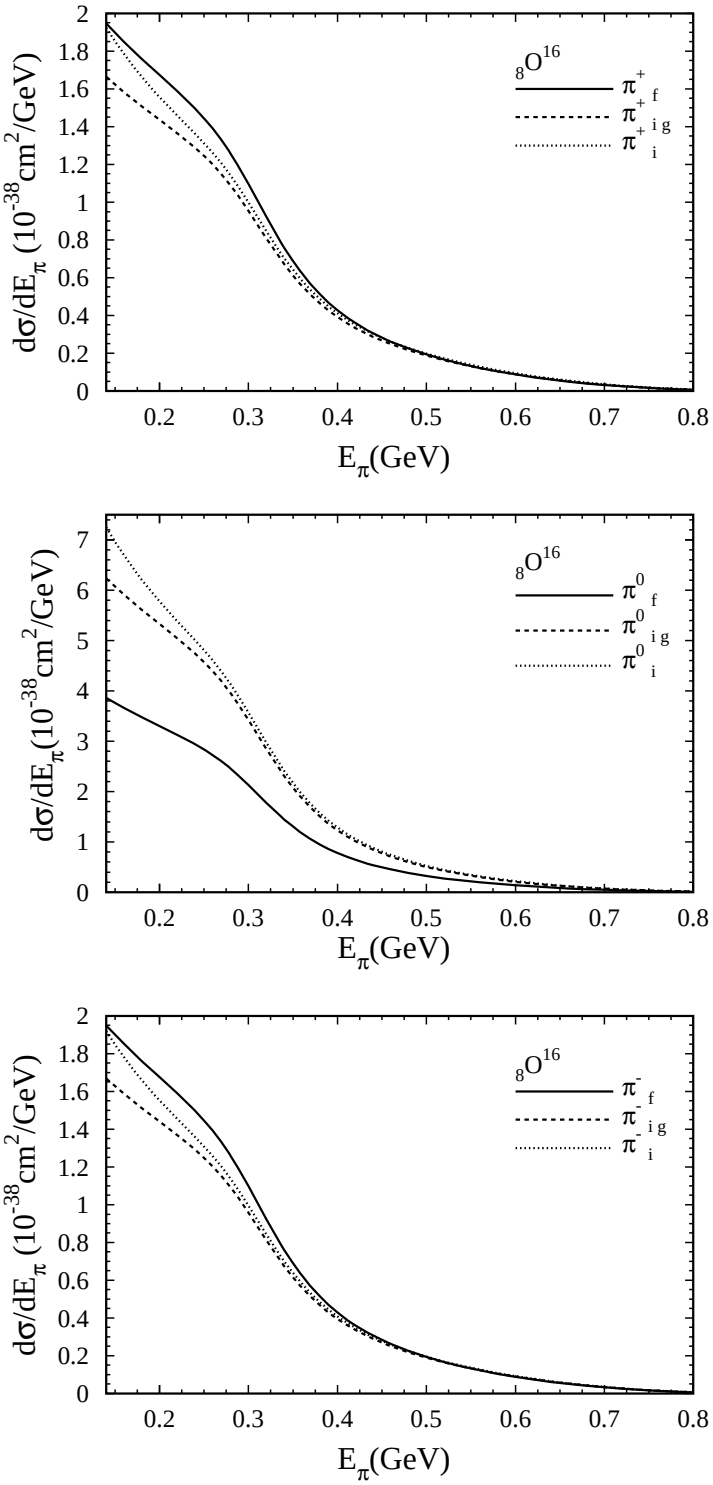

Figure 2.17: Pion energy distribution for a) positively charged pions b) neutral pions c) negatively charged pions produced for NC scattering of neutrinos on oxygen targets. The solid, dashed and dotted lines represent respectively the pion energy distribution including all nuclear corrections, including only the Pauli production factor g and without any nuclear correction.

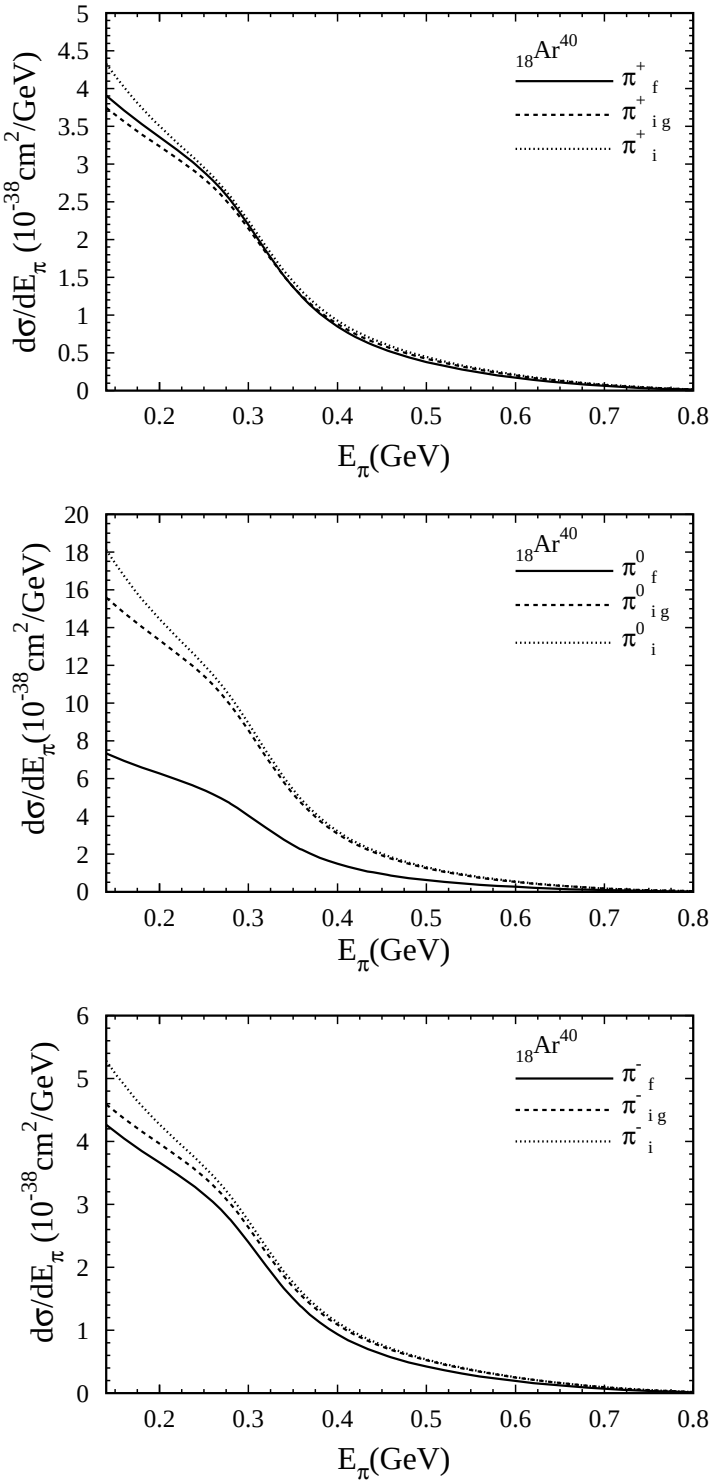

Figure 2.18: The same as in Fig. 2.17 for an argon target.

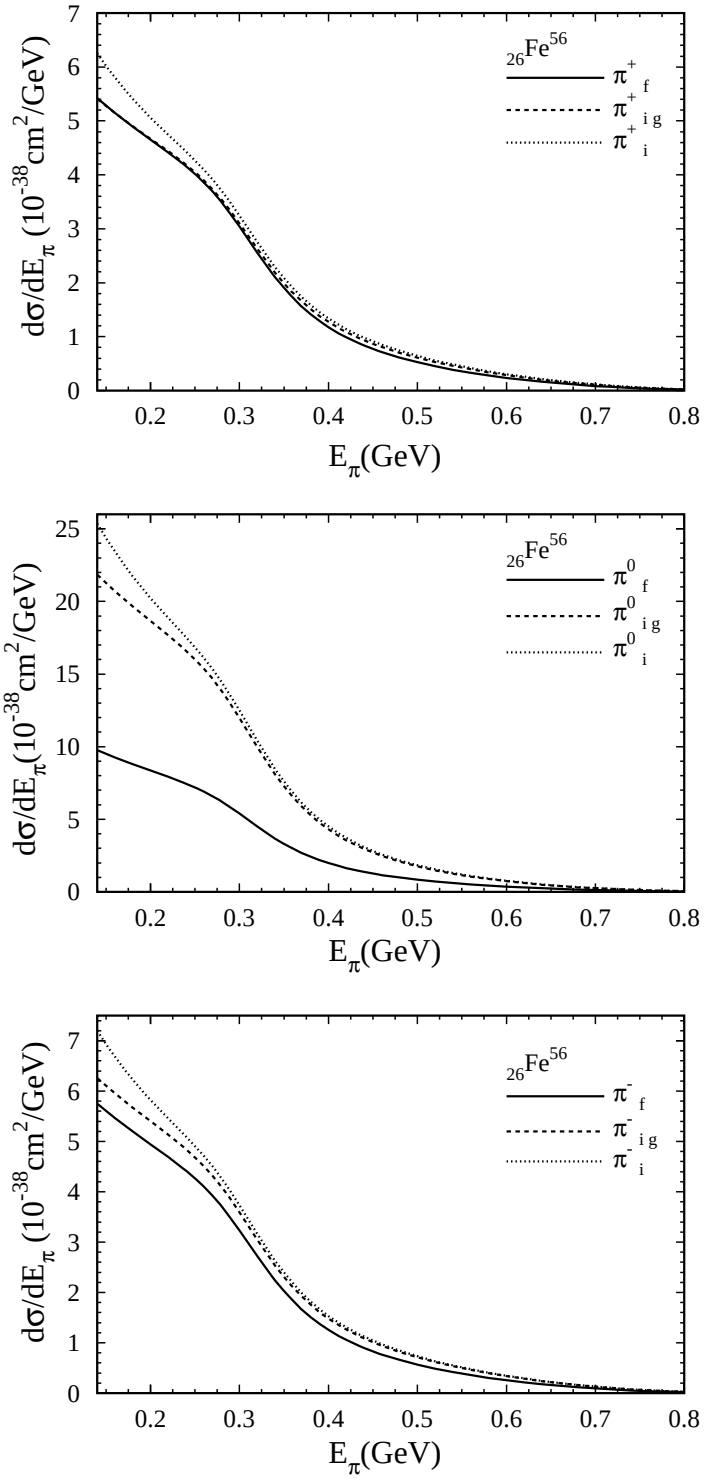

Figure 2.19: The same as in Fig. 2.17 for an iron target.

2.4 Conclusions

Several long-baseline neutrino experiments plan to study low energy neutrino reactions. Their main aim is the observation and better understanding of neutrino-oscillations. A necessary input is the understanding of these reactions in free protons and neutrons, as well as the modifications brought about when the nucleons are bound in relatively heavy nuclei.

In order to work in a coherent framework we calculated the cross sections on free protons and neutrons. The theory for the production of the $\Delta(1232)\mathrm{P}_{33}$ resonance is well understood and our results for the total cross section agree with the experimental data. The same holds for other channels where $I = \frac{1}{2}$ resonances also contribute. The comparisons appear in figs. 2.3–2.12, where it is evident that the accuracy of the measurements is subject to large improvements. Thus it is highly desirable that the new experiments use the nearby detector in order to measure the various cross sections. This refers to charged and neutral currents interactions on free protons and neutrons. The main uncertainties described in this part of the thesis are the functional form and parameters of the form factors and the interference between $I = \frac{3}{2}$ and $I = \frac{1}{2}$ resonances. We expect that the effects from these uncertainties are small.

More important are changes which are brought about in the scattering of neutrinos in heavy nuclei. It is very likely that the far away detectors will use heavy materials as targets in order to enhance their counting rates. The heavy materials will bring in corrections comparable to oscillations. In this work we used an old model for nuclear corrections [30] and calculated the effects on the produced $\pi^{\pm,0}$. In section 2.3 we reviewed details of the main features of the model.

At first, we calculated the CC cross sections in order to examine the absorption and charge exchange effects in nuclei targets using two different absorption models, see Fig. 2.16. We found that the total nuclear corrections in the $\pi^{\pm}$ case are about $40 - 60\%$ depending on the absorption model. In the π^0 case the corrections ranged between 0 and 25% again depending on the absorption model.

Futhermore, we decided that an interesting and important parameter in the experiments is the energy of the emerging pion. For the NC case, we plotted in figures 2.17–2.19 the pion spectra as function of their energy and found that the largest correction appears in the spectrum of the $\pi^{0\prime}$s. The reduction of the signal for neutral pions with energies

of approximately 200 MeV is substantial: of the order of 40%. Processes with nuclear corrections as large as the ones found in this study require special attention.

Several strategies suggest themselves. One should use the same material for the front and the far away detector and study the spectra as a function of E_π. Then should be compared the results from the two detectors with quasi-elastic scattering. In case that the experiments are forced to use different materials detailed calculations for the two materials will point to similarities and possible differences between the two targets.

Chapter 3

Neutrino Interactions in Oscillation Experiments

3.1 Introduction

Oscillation experiments [5–7] provide evidence for non-vanishing neutrino masses. Prominent among them is the reduction of the fluxes of atmospheric muon neutrinos and solar electron neutrinos. To measure precisely the parameters $\delta m^2 \simeq 10^{-2} - 10^{-3}\,\mathrm{eV}^2$ and $\sin^2 2\theta$, as well as to better understand the neutrino oscillation there are Long Baseline (LBL) experiments, like K2K, [67], JHF-Kamioka [25][1], MINOS [19], OPERA [21] and ICANOE [20], under construction and others being planned or running. The interest of LBL experiments lies mainly on the $\nu_\mu \to \nu_\tau$ channel, since it is already known from the CHOOZ experiment [69] that the possibility of $\nu_\mu \to \nu_e$ oscillation is very much suppressed. In the LBL experiments several reactions contribute to neutrino nucleon reactions, namely deep inelastic scattering (DIS), quasi-elastic (QE) and resonance (RES) reactions. The latter two are low energy reactions, which are however still significant in the kinematic range of the new experiments with neutrino energies $E_\nu \simeq 4 - 30$ GeV. Therefore, these contributions should be included in the theoretical description of charged current reactions for τ appearance

$$\nu_\tau + N \to \tau^- + X, \tag{3.1}$$

[1]Quasi-elastic and resonance reactions are important at the K2K and JHF-Kamioka experiments in Japan because of the low neutrino energy ($E_\nu \simeq 1$ GeV), see [25, 68]. Since the beam energy is less than the threshold for the production of τ-leptons (3.5 GeV) we do not consider them here.

with $N = p, n$. In addition, we think it is useful to look at the various CC channels of ν_τ, searching for additional signatures which will help to confirm the reactions, since the expected number of τ-events will be small. For this reason, we calculate the total cross sections and the number of events, N_τ, for the deep inelastic, the quasi-elastic and the resonance channels of CC reactions. In addition, we consider NC reactions since they are important for establishing or eliminating oscillations into sterile neutrinos which are not completely excluded yet. In the previous chapter we have already discussed the single pion production and the associated nuclear corrections of the resonances. Here we examine the DIS and QE channels including nuclear contributions as well. These results will be used to evaluate the number of events, N_τ, for a heavy target like ${}_{26}\mathrm{Fe}^{56}$. For completeness, we also present anti-neutrino nucleon interactions of NC and CC reactions for QE and DIS with and without nuclear corrections.

This chapter is organized as follows:

In section 3.2 we present the formalism and the evaluation of the charged and neutral current total cross section for deep inelastic scattering, quasi-elastic scattering and the resonance channels. In section 3.3 we explain theoretical aspects of the nuclear effects for the charged and neutral current total cross sections. Then we summarize our results for all the type of reactions including nuclear corrections in section 3.4. In section 3.5 we give the number of events, N_τ, with and without nuclear corrections for CC and NC channels for the OPERA experiment. Several conclusions and their importance for the experiments are included in section 3.6. The results of this chapter should be useful for LBL experiments [19–21, 25, 67] and those being discussed for the neutrino factory [26].

3.2 General Formalism

In this section we explain the main equations and the form factors used to calculate the cross section for DIS, QE and RES in (anti-)neutrino-nucleon interactions. Although the main contribution comes from DIS, we include also QE and RES because their contribution is still important in the energy region of LBL experiments. In the following, we outline the calculation of the cross sections for DIS and QE scattering, while the resonance reactions have already been discussed in chapter 2.

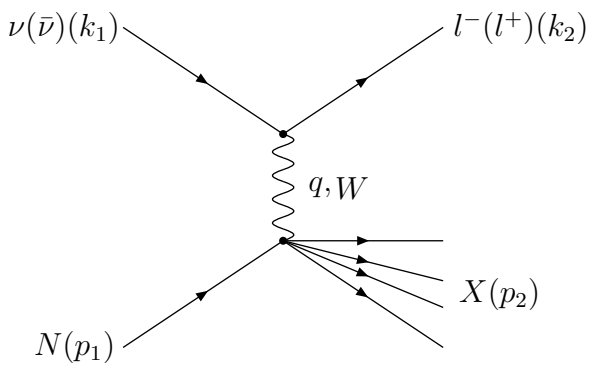

Figure 3.1: The Feynman diagram for the DIS charged current reaction $\nu_l(\bar{\nu}_l)(k_1) + N(p_1) \rightarrow l^-(l^+)(k_2) + X(p_2)$.

3.2.1 Deep Inelastic Scattering

In this subsection we present the theoretical framework for the calculation of $\nu(\bar{\nu})$-nucleon DIS cross sections. The CC channels are given by the following equation (see the Feynman diagram in Fig. 3.1):

$$\nu_l(\bar{\nu}_l)(k_1) + N(p_1) \rightarrow l^-(l^+)(k_2) + X(p_2). \tag{3.2}$$

The NC channels are:

$$\nu_l(\bar{\nu}_l)(k_1) + N(p_1) \rightarrow \nu_l(\bar{\nu}_l)(k_2) + X(p_2), \tag{3.3}$$

where N is a nucleon and $l = \mu, \tau$ and X is the system of outgoing hadrons. The double-differential cross section $\mathrm{d}\sigma/\mathrm{d}x\mathrm{d}y$ can be expressed in terms of a leptonic tensor $L^{\mu\nu}$ and a hadronic tensor $W_{\mu\nu}$:

$$\frac{\mathrm{d}\sigma}{\mathrm{d}x\mathrm{d}y} = \frac{G_F^2 y}{16\pi}\kappa^2 L^{\mu\nu}W_{\mu\nu}, \tag{3.4}$$

where $\kappa = \frac{M_W^2}{Q^2+M_W^2}$ for the CC case, G_F is the Fermi constant, M_W is the W-boson mass and $y = \frac{\nu}{E_\nu}$. In the case of NC we have $\kappa = \frac{M_Z^2}{Q^2+M_Z^2}$ with M_Z the Z-boson mass.

The leptonic tensor $L^{\mu\nu}$ is:

$$L^{\mu\nu} = 2\mathrm{Tr}[(\not{k}_2 + m_l)\gamma^\mu(1-\gamma_5)\not{k}_1\gamma^\nu], \tag{3.5}$$

with the lepton mass m_l, denoting m_τ or m_μ in the CC case. In the NC case we have $m_l = 0$. Note that, since in NC neutrino scattering $C_V = C_A$ we find in both cases, CC

and NC, a $\gamma^\mu(1-\gamma_5)$ structure in the leptonic tensor. Following Ref. [70] the general hadronic tensor $W_{\mu\nu}$ is defined by:

$$\begin{aligned} W_{\mu\nu} &= -g_{\mu\nu}F_1(x,Q^2) + \frac{p_{1\mu}p_{1\nu}}{p_1\cdot q}F_2(x,Q^2) - i\epsilon_{\mu\nu\rho\sigma}\frac{p_1^\rho q^\sigma}{2p_1\cdot q}F_3(x,Q^2) \\ &+ \frac{q_\mu q_\nu}{p_1\cdot q}F_4(x,Q^2) + (p_{1\mu}q_\nu + p_{1\nu}q_\mu)F_5(x,Q^2). \end{aligned} \tag{3.6}$$

Here $\epsilon_{\mu\nu\rho\sigma}$ is the total antisymmetric tensor with $\epsilon_{0123} = +1$. The $F_i\,(i = 1...5)$ are the structure functions in neutrino-nucleon deep inelastic scattering. We have derived the following expression for the differential cross section in the case of $m_l \neq 0$:

$$\begin{aligned} \frac{\mathrm{d}\sigma^{\nu,\bar\nu}}{\mathrm{d}x\mathrm{d}y} &= \frac{G_F^2 M_N E_\nu}{\pi}\Big[y\Big(xy + \frac{m_l^2}{2E_\nu M_N}\Big)F_1 + \Big(1 - y - \frac{M_N xy}{2E_\nu} - \frac{m_l^2}{4E_\nu^2}\Big)F_2 \\ &\pm\Big(xy(1-\frac{y}{2}) - y\frac{m_l^2}{4M_N E_\nu}\Big)F_3 + \Big(xy\frac{m_l^2}{2M_N E_\nu} + \frac{m_l^4}{4M_N^2 E_\nu^2}\Big)F_4 - \frac{m_l^2}{2M_N E_\nu}F_5\Big], \end{aligned} \tag{3.7}$$

where $x = \frac{Q^2}{2M_N\nu}$ with $\nu = E_\nu - E_l$, $Q^2 = 2M_N E_\nu xy$, $M_N$with $N = p, n$ the nucleon mass and the $\pm F_3$ signs correspond to the $\nu(\bar\nu)$-nucleon scattering.

To obtain the structure functions for the proton and the neutron for charged and neutral channels we used the quark parton model (QPM). We treated the proton and the neutron separately in order to account for non-isoscalar targets. Above the threshold for charm production the structure functions for charged current $\nu(\bar\nu)$-proton scattering are:

$$\begin{aligned} F_2^{CC}(\nu p) &= 2x[d + s + \bar u + \bar c] \\ xF_3^{CC}(\nu p) &= 2x[d + s - \bar u - \bar c] \\ F_2^{CC}(\bar\nu p) &= 2x[u + c + \bar d + \bar s] \\ xF_3^{CC}(\bar\nu p) &= 2x[u + c - \bar d - \bar s] \end{aligned} \tag{3.8}$$

and for $\nu(\bar\nu)$-neutron scattering:

$$\begin{aligned} F_2^{CC}(\nu n) &= 2x[u + s + \bar d + \bar c] \\ xF_3^{CC}(\nu n) &= 2x[u + s - \bar d - \bar c] \\ F_2^{CC}(\bar\nu n) &= 2x[d + c + \bar u + \bar s] \\ xF_3^{CC}(\bar\nu n) &= 2x[d + c - \bar u - \bar s]. \end{aligned} \tag{3.9}$$

Below the threshold for charm production the corresponding structure functions for the proton are:

$$F_2^{CC}(\nu p) = 2x[d\cos^2\theta_c + s\sin^2\theta_c + \bar u + \bar c]$$

$$\begin{aligned} xF_3^{CC}(\nu p) &= 2x[d\cos^2\theta_c + s\sin^2\theta_c - \bar{u} - \bar{c}] \\ F_2^{CC}(\bar{\nu} p) &= 2x[u\cos^2\theta_c + c\sin^2\theta_c + \bar{d} + \bar{s}] \\ xF_3^{CC}(\bar{\nu} p) &= 2x[u\cos^2\theta_c + c\sin^2\theta_c - \bar{d} - \bar{s}] \end{aligned} \tag{3.10}$$

and for the neutron

$$\begin{aligned} F_2^{CC}(\nu n) &= 2x[u\cos^2\theta_c + s\sin^2\theta_c + \bar{d} + \bar{c}] \\ xF_3^{CC}(\nu n) &= 2x[u\cos^2\theta_c + s\sin^2\theta_c - \bar{d} - \bar{c}] \\ F_2^{CC}(\bar{\nu} n) &= 2x[d\cos^2\theta_c + c\sin^2\theta_c + \bar{u} + \bar{s}] \\ xF_3^{CC}(\bar{\nu} n) &= 2x[d\cos^2\theta_c + c\sin^2\theta_c - \bar{u} - \bar{s}], \end{aligned} \tag{3.11}$$

with Cabibbo angle $\cos\theta_c = 0.9755$ [45]. Notice that the contribution of the threshold effect for charm production is small ($\simeq 5\%$) and negligible.

The neutral current reactions for $\nu(\bar{\nu})$-proton scattering depend on:

$$\begin{aligned} F_2^{NC}(\nu p, \bar{\nu} p) &= 2x((g_L^2 + g_R^2)[u + c + \bar{u} + \bar{c}] + (g_L'^2 + g_R'^2)[d + s + \bar{d} + \bar{s}]) \\ xF_3^{NC}(\nu p, \bar{\nu} p) &= 2x((g_L^2 - g_R^2)[u + c - \bar{u} - \bar{c}] + (g_L'^2 - g_R'^2)[d + s - \bar{d} - \bar{s}]) \end{aligned}$$

and for the neutron

$$\begin{aligned} F_2^{NC}(\nu n, \bar{\nu} n) &= 2x((g_L^2 + g_R^2)[d + c + \bar{d} + \bar{c}] + (g_L'^2 + g_R'^2)[u + s + \bar{u} + \bar{s}]) \\ xF_3^{NC}(\nu n, \bar{\nu} n) &= 2x((g_L^2 - g_R^2)[d + c - \bar{d} - \bar{c}] + (g_L'^2 - g_R'^2)[u + s - \bar{u} - \bar{s}]), \end{aligned} \tag{3.12}$$

where $g_L = \frac{1}{2} - \frac{2}{3}\sin^2\theta_W$, $g_R = -\frac{2}{3}\sin^2\theta_W$ and $g'_L = -\frac{1}{2} + \frac{1}{3}\sin^2\theta_W$, $g'_R = \frac{1}{3}\sin^2\theta_W$ with the Weinberg angle $\sin^2\theta_W = 0.23117$ [45]. To calculate the total cross section we integrate $\frac{\mathrm{d}\sigma}{\mathrm{d}x\mathrm{d}y}$ for the muon case in the range $0 \leq x \leq 1$ and $0 \leq y \leq 1$. For the tau case we use the limits [71]:

$$\begin{aligned} &\frac{m_\tau^2}{2M_N(E_\nu - m_\tau)} \leq x \leq 1 \\ &a - b \leq y \leq a + b, \end{aligned} \tag{3.13}$$

where a and b are defined the following way:

$$\begin{aligned} a &= \frac{1 - m_\tau^2(\frac{1}{2M_N E_\nu x} + \frac{1}{2E_\nu^2})}{2(1 + \frac{M_N x}{2E_\nu})} \\ b &= \frac{\sqrt{(1 - \frac{m_\tau^2}{2M_N E_\nu x})^2 - \frac{m_\tau^2}{E_\nu^2}}}{2(1 + \frac{M_N x}{2E_\nu})}. \end{aligned} \tag{3.14}$$

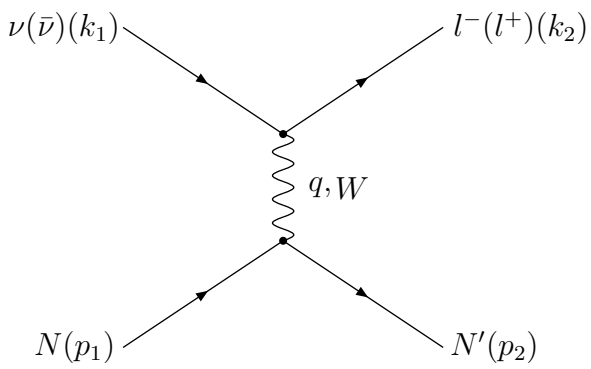

Figure 3.2: The Feynman diagram for the QE charged current reaction $\nu_l(\bar{\nu}_l)(k_1) + N(p_1) \rightarrow l^-(l^+)(k_2) + N'(p_2)$.

The derivation of Eq. (3.13) is presented in appendix E.

For the quark distributions we use the CTEQ5 leading order (LO) parton distributions [72]. The Callan-Gross relation relates F_2 to F_1:

$$2xF_1 = F_2. \tag{3.15}$$

Furthermore, we use for F_4 and F_5 the Albright-Jarlskog relations [71]:

$$F_4 = 0 \tag{3.16}$$

$$xF_5 = F_2. \tag{3.17}$$

3.2.2 Quasi-Elastic Scattering

Following Ref. [35] we calculated the charged current and neutral current channels of $\nu(\bar{\nu}) - N$ reactions:

$$\nu_l(\bar{\nu}_l)(k_1) + N(p_1) \rightarrow l^-(l^+)(k_2) + N'(p_2) \qquad \text{(CC)} \tag{3.18}$$

$$\nu_l(\bar{\nu}_l)(k_1) + N(p_1) \rightarrow \nu_l(\bar{\nu}_l)(k_2) + N'(p_2) \qquad \text{(NC)}. \tag{3.19}$$

The Feynman diagram for the QE charged current reaction Eq. (3.18) is depicted in Fig. 3.2. Notice that the neutral current reaction on neutron targets is in practice not measurable, even though its cross section is comparable to the proton reaction. The matrix element of the quasi-elastic reactions can be defined as follows:

$$\mathcal{M} = \frac{ig^2 \cos\theta_c}{4} \frac{g_{\mu\nu}}{q^2 - M_W^2} \bar{u}(k_2)\gamma^\mu(1-\gamma_5)u(k_1)\bar{u}(p_2)\Gamma^\nu u(p_1). \tag{3.20}$$

Γ^ν is given by:

$$\begin{aligned}\Gamma^\nu &= \gamma^\nu F_1^V(q^2) + i\sigma^{\nu\alpha}\frac{q_\alpha \xi F_2^V(q^2)}{2M_N} \\ &\quad + \frac{q^\nu F_3^V(q^2)}{M_N} + \gamma^\nu\gamma_5 F_A(q^2) + \frac{q^\nu\gamma_5 F_p(q^2)}{M_N} + \frac{\gamma_5(p_1+p_2)^\nu}{M_N}F_3^A(q^2), \qquad (3.21)\end{aligned}$$

where F_i^V $(i = 1, 2, 3)$, F_A, F_3^A, F_p are the weak form factors of the nucleon. The form factors are in general complex, but general principles eliminate two of them and require the rest to be real. First, F_i^V, F_A, F_p and F_3^A are real because of time reversal invariance. Second, F_1^V, F_2^V, F_A and F_p are real but F_3^A and F_3^V are imaginary because of charge symmetry. Thus $F_3^A = F_3^V = 0$ (no second class currents) from these two constraints. The conserved vector current (CVC) hypothesis establishes the following relations between the weak form factors and the electromagnetic form factors: $F_1^V(q^2) = F_1^p(q^2) - F_1^n(q^2)$ and $\xi F_2^V(q^2) = \mu_p F_2^p(q^2) - \mu_n F_2^n(q^2)$ with $\xi = \mu_p - \mu_n = 3.706$, $k_p = \mu_p - 1 = 1.793$ and $k_n = \mu_n = -1.913$. k_p and k_n are the anomalous magnetic moments of proton and neutron and $F_1^{p,n}$ and $F_2^{p,n}$ are the electromagnetic Dirac-Pauli isovector form factors of proton and neutron. $F_1^V(q^2)$ and $F_2^V(q^2)$ can be expressed in terms of the Sachs form factors:

$$F_1^V(q^2) = \frac{G_E^V(q^2) - \frac{q^2}{4M_N^2}G_M^V(q^2)}{1 - \frac{q^2}{4M_N^2}} \qquad (3.22)$$

$$\xi F_2^V(q^2) = \frac{G_M^V(q^2) - G_E^V(q^2)}{1 - \frac{q^2}{4M_N^2}}, \qquad (3.23)$$

where

$$G_E^V(q^2) = \frac{1}{(1 - \frac{q^2}{M_V^2})^2} \qquad (3.24)$$

$$G_M^V(q^2) = \frac{1+\xi}{(1 - \frac{q^2}{M_V^2})^2} \qquad (3.25)$$

with a vector mass $M_V = 0.84$ GeV. The axial vector form factor is given by:

$$F_A(q^2) = \frac{F_A(0)}{(1 - \frac{q^2}{M_A^2})^2} \qquad (3.26)$$

with an axial vector mass $M_A = 1.0$ GeV and $F_A(q^2 = 0) = -1.23$. A reasonable approximation for all q^2 is given by:

$$F_p(q^2) = 2M_N^2\frac{F_A(q^2)}{m_\pi^2 - q^2} \qquad (3.27)$$

with the pion mass $m_\pi = 0.14$ GeV.

For NC reactions, we replace the charged current form factors with the neutral current form factors. In the electroweak theory the charged current form factors are related to the neutral current form factors as follows:

$$(F_1^V)^{NC}(q^2) = \frac{1}{2}F_1^V(q^2) - 2\sin^2\theta_W F_1^p(q^2) \tag{3.28}$$

$$\xi(F_2^V)^{NC}(q^2) = \frac{1}{2}\xi F_2^V(q^2) - 2\sin^2\theta_W\,(\mu_p - 1)F_2^p(q^2) \tag{3.29}$$

$$F_A^{NC}(q^2) = \frac{1}{2}F_A(q^2) \tag{3.30}$$

$$F_p^{NC}(q^2) = \frac{2M_N^2 F_A^{NC}(q^2)}{(m_\pi^2 - q^2)}, \tag{3.31}$$

where

$$F_1^N(q^2) = \frac{G_E^N(q^2) - \frac{q^2 G_M^N(q^2)}{4M_N^2}}{1 - \frac{q^2}{4M_N^2}}, \quad \mu_N F_2^N(q^2) = \frac{G_M^N(q^2) - G_E^N(q^2)}{1 - \frac{q^2}{4M_N^2}}, \tag{3.32}$$

$$G_E^N(q^2) = \frac{G_E^N(0)}{(1 - \frac{q^2}{M_V^2})^2}, \quad G_M^N(q^2) = \frac{G_M^N(0)}{(1 - \frac{q^2}{M_V^2})^2}\ . \tag{3.33}$$

At $q^2 = 0$ the form factors are normalized by the following conditions:

$$G_E^p(0) = 1, \quad G_E^n(0) = 0,$$
$$G_M^{p,n}(0) = \mu_{p,n}, \quad F_A^{NC}(0) = -0.615.$$

After some standard but tedious algebra we arrive at the differential cross section:

$$\begin{aligned}\frac{\mathrm{d}\sigma}{d|q^2|} = \frac{G_F^2\cos^2\theta_c}{8\pi E_\nu^2}\Bigg[&(F_1^V)^2\frac{q^4 - 4M_N^2(m_l^2 - q^2) - m_l^4}{4M_N^2} \\ &+(\xi F_2^V)^2\frac{4M_N^2(q^4 - m_l^4) - q^4(m_l^2 - q^2)}{16M_N^4} + (F_A)^2\frac{q^4 + 4M_N^2(m_l^2 - q^2) - m_l^4}{4M_N^2} \\ &-(F_p)^2\frac{m_l^2 q^2(-q^2 + m_l^2)}{4M_N^4} + F_1^V\xi F_2^V\frac{2q^4 + q^2 m_l^2 + m_l^4}{2M_N^2} \\ &-F_A F_P\frac{m_l^2(-q^2 + m_l^2)}{2M_N^2} + F_A(F_1^V + \xi F_2^V)q^2\frac{(s-u)}{M_N^2} \\ &+\Big((F_1^V)^2 - \frac{(\xi F_2^V)^2 q^2}{4M_N^2} + (F_A)^2\Big)\frac{(s-u)^2}{4M_N^2}\Bigg],\end{aligned} \tag{3.34}$$

with $s - u = 4E_\nu M_N + q^2 - m_l^2$. For the anti-neutrino nucleon reactions in QE channels we replace the term $F_A(F_1^V + \xi F_2^V)$ by $-F_A(F_1^V + \xi F_2^V)$.

3.2.3 Resonance Production

In the previous chapter we discussed in detail the neutral current differential cross section for the production of resonances on various materials and included nuclear effects. In this subsection we include in addition the $\nu_\tau(\bar{\nu}_\tau)$-nucleon interactions of charged current channels, like:

$$\nu_\tau(\bar{\nu}_\tau) + p \to \tau^-(\tau^+) + p + \pi^+(\pi^-) \tag{3.35}$$

$$\nu_\tau(\bar{\nu}_\tau) + n \to \tau^-(\tau^+) + n + \pi^+(\pi^-) \tag{3.36}$$

$$\nu_\tau(\bar{\nu}_\tau) + n(p) \to \tau^-(\tau^+) + p(n) + \pi^0, \tag{3.37}$$

where $m_\tau = 1.78$ GeV and calculate the differential cross sections with respect to the pion energy as well as the total cross sections. We present the results for various incoming neutrino energies and include nuclear corrections for the different nuclei, using the same kinematics as in chapter 2.

3.3 Nuclear Effects

As mentioned already the heavy nuclei of the targets bring in additional effects. We discuss them separately for the various reactions, considering ${}_{26}\mathrm{Fe}^{56}$ as a typical target. We investigate in this section nuclear effects for the DIS and QE reactions. In addition, having already considered the charged and neutral current processes for the muon case in chapter 2, we extend these studies here to the tau case.

3.3.1 Deep Inelastic Scattering

For the nuclear corrections in deep inelastic scattering we use two different sets of nuclear parton distributions, the χ^2-analysis of Ref. [27] as well as the EKS98 parameterization [28, 29]. The EKS98 nuclear parton distributions are determined by a DGLAP evolution of input distributions given at an initial scale $Q_0^2 = 2.25$ GeV^2 in the x range $10^{-6} \leq x \leq 1$. These input distributions have been fixed using the data from lepton-nucleus (lA) DIS and Drell-Yan (DY) measurements from proton-nucleus (pA) collisions with conservation of momentum and baryon number as constraints. Their nuclear modifications in different regions of the variable x comprise:

- shadowing: a depletion at $x \lesssim 0.1$,

- anti-shadowing: an excess at $0.1 \lesssim x \lesssim 0.3$,
- EMC effect: a depletion at $0.3 \lesssim x \lesssim 0.7$,
- Fermi motion: an excess towards $x \to 1$ and beyond.

The first method is based on a χ^2-analysis of data, which have been taken from deep inelastic electron and muon scattering and provides nuclear structure functions at the initial scale $Q_0^2 = 1.0$ GeV^2 in the x range $10^{-9} \leq x \leq 1$. The χ^2-analysis does not contain a charm distribution. Their results are quite sensitive on the Bjorken variable x and there is a slight difference between the χ^2-analysis from Ref. [27] and the EKS98 parameterization [28, 29]. However, the difference occurs mainly in the sea quark distribution and is only noticeable in the small x region.

3.3.2 Quasi-Elastic Scattering

Important nuclear effects for the quasi-elastic scattering arise from the Pauli principle, rescattering and absorption of recoiling hadrons and from the Fermi motion. We use only the Pauli principle since it is the most important nuclear effect and neglect the other two, see Refs. [73–75] for a detailed discussion. We calculate the Pauli factor of the quasi-elastic scattering according to Refs. [35, 76, 77]. We multiply the Pauli factor $g = 1 - N^{-1}D$ with the total cross section for QE where:

$$D = \begin{cases} Z & \text{for } 2x < u - v \\ 0.5A\Big(1 - \frac{3x(u^2+v^2)}{4} + \frac{x^3}{3} - \frac{3(u^2-v^2)^2}{32x}\Big) & \text{for } u - v < 2x < u + v \\ 0 & \text{for } 2x > u + v, \end{cases} \tag{3.38}$$

where

$$x = \frac{|\mathbf{q}|}{2k_F}, \quad u = \Big(\frac{2N}{A}\Big)^{\frac{1}{3}}, \quad v = \Big(\frac{2Z}{A}\Big)^{\frac{1}{3}}. \tag{3.39}$$

The Fermi momentum $k_F = 1.36$ fm^{-1} is taken from Ref. [64]. N, Z, and A are neutron, proton, and nucleon number, respectively. The three-momentum transfer $|\mathbf{q}|$ is defined by $|\mathbf{q}| = \frac{q^2}{2M_N}\sqrt{1 - \frac{4M_N^2}{q^2}}$. For protons we just replace N by Z.

3.4 Results

We present results for ν_μ and ν_τ induced reactions. All ν_τ charged current reactions show an evident τ-lepton threshold with the cross sections becoming large and noticeable for beam energies above $5-6$ GeV. The neutral current reactions do not show any threshold but they are smaller than the ν_μ reactions by a factor of approximately ten.

The energy dependence is the second difference: The QE and RES total cross sections reach constant asymptotic values at high energies, while the DIS cross section rises linearly with energy. For this reason we plot for DIS the ratios σ/E_ν or $\sigma/(G_F^2 m_N E_\nu/\pi)$. Immediately above the threshold for ν_τ the DIS process dominates over the QE and RES, while below $E_\nu < 5$ GeV the sum of QE and RES is approximately 50% of the total cross section. We discuss next each of the reactions separately.

3.4.1 Deep Inelastic Scattering

In Fig. 3.3 we show the total cross sections for the reactions $\nu_\mu(\bar{\nu}_\mu) + N \to \mu^-(\mu^+) + X$ with nuclear corrections using the EKS98 parameterization [28, 29] (solid line) and without nuclear corrections (dashed line) as a function of neutrino energy. More precisely, we plot the slopes vs energy. We see that the curves start with a constant slope and remain so up to 350 GeV. We also include the experimental data from various groups [48, 78–89]. The data are closer to the curves which include nuclear effects.

Fig. 3.4 shows the reaction $\nu_\tau + N \to \tau^- + X$ where the threshold dependence from the mass of the τ-lepton is now evident. For comparison we included the ν_μ cross section. The ν_μ and ν_τ induced reactions will merge into each other at an energy of 1 TeV, which is unrealistic for LBL experiments. Such energetic neutrinos may be detectable in Antares [90], Nestor [91], Amanda [92], and Baikal [93].

For comparison with other reactions we plot in Figs. 3.5 and 3.6 the slope of the ν_μ and ν_τ CC cross sections for the sum of the three types of reactions. For the ν_μ CC case (Fig. 3.5), it is clear that the QE and RES dominate up to $E_\nu \lesssim 1.3\,\text{GeV}$. DIS is dominant for $E_\nu \gtrsim 1.3\,\text{GeV}$ and the total cross section rises linearly. Our curve and data agree very well. For the ν_τ case (Fig. 3.6), we also note that at high energies DIS dominates. The QE and RES give a noticeable contribution around 5 GeV where a kink in the slope is visible.

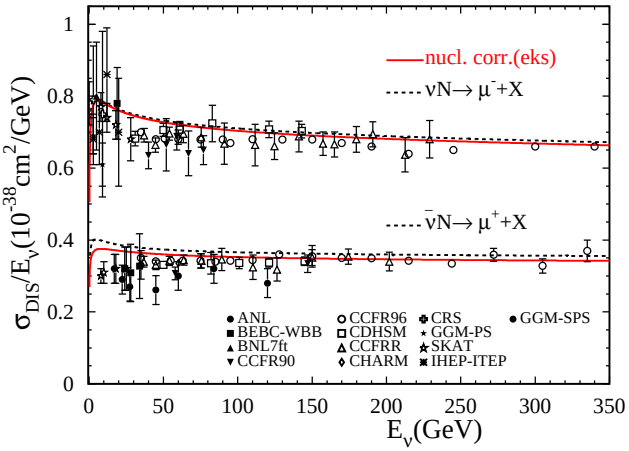

Figure 3.3: The cross section of DIS for $\nu_\mu + N \to \mu^- + X$ and $\bar{\nu}_\mu + N \to \mu^+ + X$ plotted versus the incoming neutrino energy for an isoscalar target with the normalization of $1/E_\nu$. The solid and dashed curves represent the cross section of DIS with nuclear corrections of EKS98 parameterization [28, 29] and without nuclear corrections. The data points have been taken from ANL [48], BEBC-WBB [78], BNL7ft [79], CCFR90 [80], CCFR96 [81], CCFRR [82], CDHSW [83], CHARM [84], CRS [85], GGM-PS [86], GGM-SPS [87], IHEP-ITEP [88], SKAT [89].

In Fig. 3.7 we show ν_τ induced cross sections for charged and neutral currents. The energy scale is now expanded to show clearly the threshold effect. Our results agree well with those in Ref. [68]. We notice that the slope of the neutral current reactions remains constant also for low energies, while the production of τ-leptons begins between $4-5$ GeV and their strength reaches large values above 8 GeV. The high energy values of charged and neutral current reactions are comparable.

Figs. 3.8 and 3.9 show the slope of cross sections for an iron target. We included in this case the nuclear corrections which turn out to be small (of order $5-7\%$). The main characteristic is the threshold dependence of the charged current reactions. Thus if the experiments can measure neutral current reactions for low energies, $E_\nu < 5$ GeV, they should observe a linear energy dependence of the events coming from ν_μ and ν_τ neutrinos, because even after the oscillation $\nu_\mu \to \nu_\tau$ their contributions are equal. If, on the other hand, the oscillation is $\nu_\mu \to \nu_s$ then there should be a decrease of the cross section in the far away detector, since the sterile neutrinos do not contribute. This decrease should be a function of E_ν and should be maximal when $\frac{\delta m^2 L}{4E_\nu} \approx \frac{\pi}{2}$.

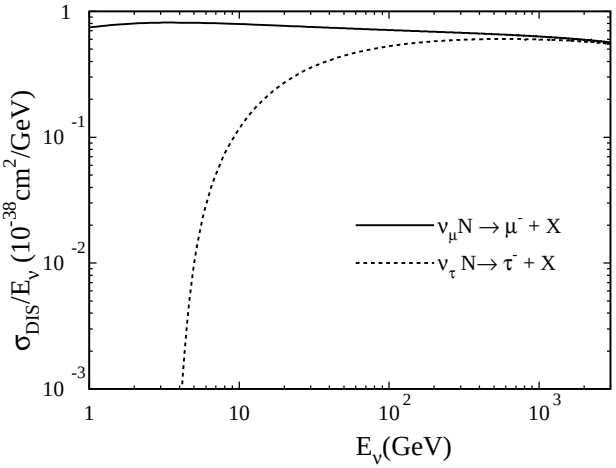

Figure 3.4: The cross section of DIS for $\nu_\tau + N \to \tau^- + X$ and $\nu_\mu + N \to \mu^- + X$ for an isoscalar target plotted versus the incoming neutrino energy with the normalization of $1/E_\nu$.

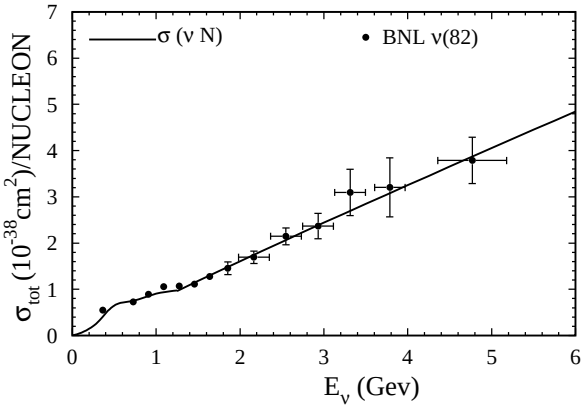

Figure 3.5: All the types of ν_μ charged current cross sections for an isoscalar target plotted as a function of neutrino energy with the normalization of 1/nucleon. The data points are taken from [79].

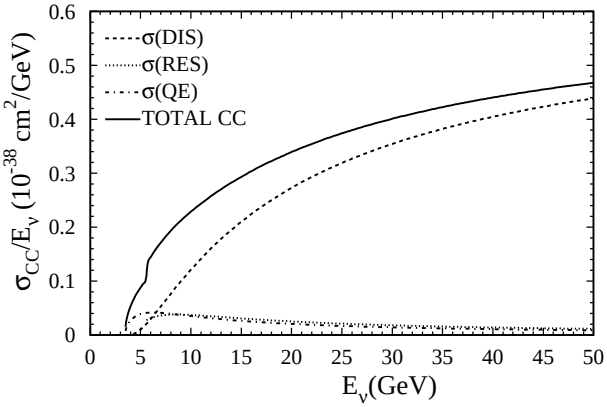

Figure 3.6: All the types of ν_τ charged current cross sections for an isoscalar target plotted as a function of neutrino energy with the normalization of $1/E_\nu$.

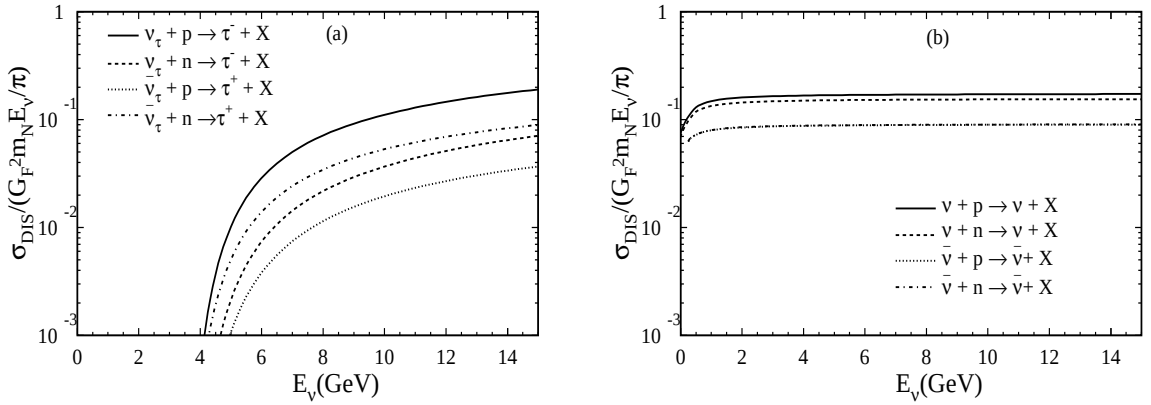

Figure 3.7: The cross section of DIS for (a) $\nu_\tau(\bar{\nu}_\tau) + N \to \tau^-(\tau^+) + X$ and (b) $\nu(\bar{\nu}) + N \to \nu(\bar{\nu}) + X$ plotted versus the incoming neutrino energy, normalized by $G_F^2 m_N E_\nu/\pi$.

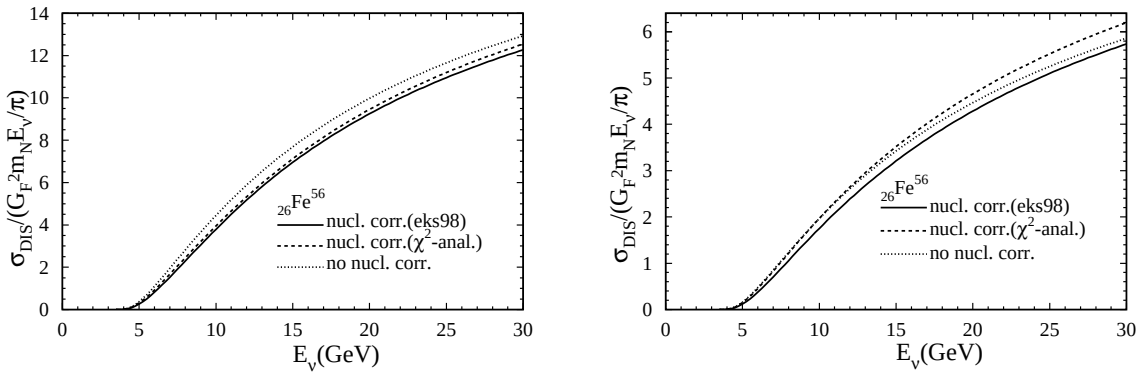

Figure 3.8: The cross section of (a) ν_τ and (b) $\bar{\nu}_\tau$ charged current reactions for DIS on iron targets versus the incoming neutrino energy, normalized by $G_F^2 m_N E_\nu/\pi$. The solid, dashed and dotted curves represent the cross section of DIS with nuclear corrections of EKS98 parameterization [28, 29] and χ^2 analysis [27] and without nuclear correction.

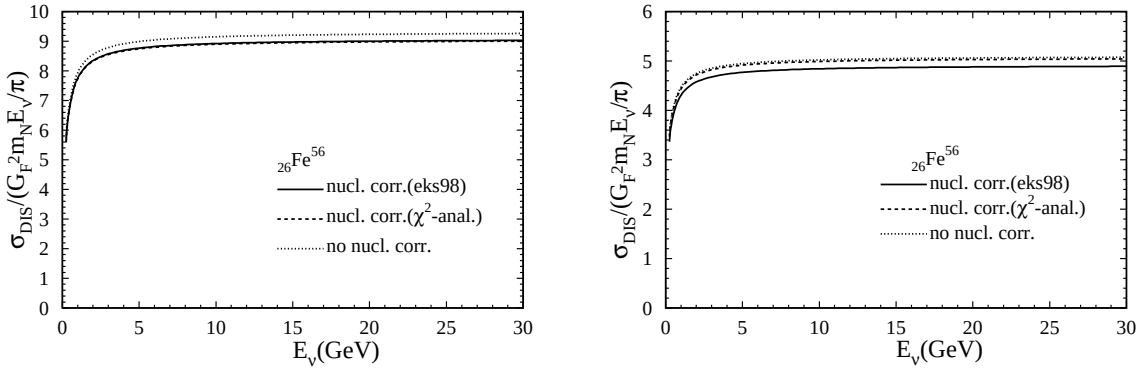

Figure 3.9: The same as in Fig. 3.8 for (a) ν and (b) $\bar{\nu}$ neutral current reactions.

3.4.2 Quasi-Elastic Scattering

In Figs. 3.10–3.12 we present our results for QE scattering. Figs. 3.10 show cross sections on free protons induced by ν_μ and $\bar{\nu}_\mu$'s. The cross sections reach a constant asymptotic value at an energy of 2 GeV. We included also the Pauli factor whose effect is small. The data are closer to the curves which include the Pauli factor. In Figs. 3.11 we show the charged current cross section induced by ν_τ's. The threshold dependence is again prominent and the cross sections have an energy dependence even at $E_{\nu_\tau} \approx 10$ GeV. The Pauli factor effect is in this case small, bringing a decrease of about 10%. Finally, the neutral current cross sections rise quickly to their asymptotic values (Figs. 3.12) which are approximately 10% of the ν_μ CC cross section. Thus the threshold effects can distinguish between ν_μ and ν_τ interactions. The neutral current events should not show a threshold effect if the oscillation is $\nu_\mu \to \nu_\tau$ and there should be no τ-leptons if the oscillation is $\nu_\mu \to \nu_s$.

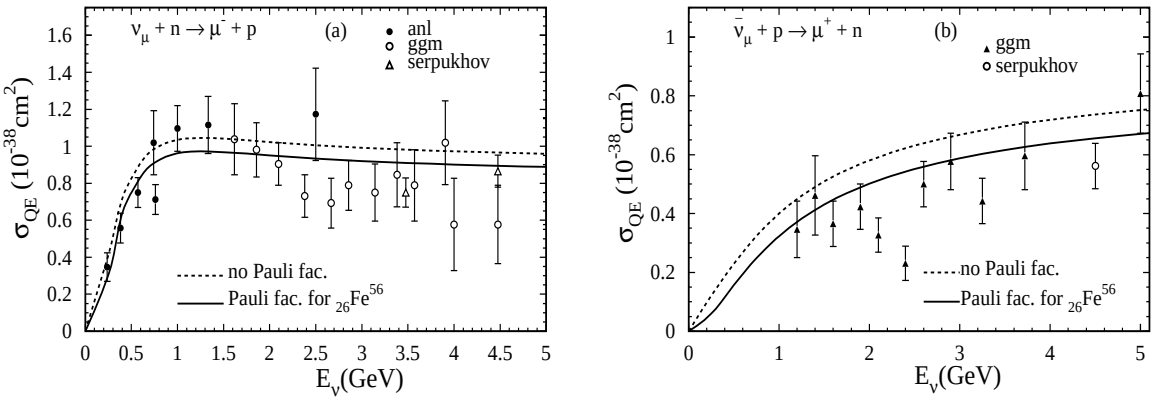

Figure 3.10: The cross section of QE for (a) $\nu_\mu + n \to \mu^- + p$ and (b) $\bar{\nu}_\mu + p \to \mu^+ + n$ process plotted versus the incoming neutrino energy with and without Pauli factor. The data points are taken from ANL [94], GGM [95] and Serpukhov [96].

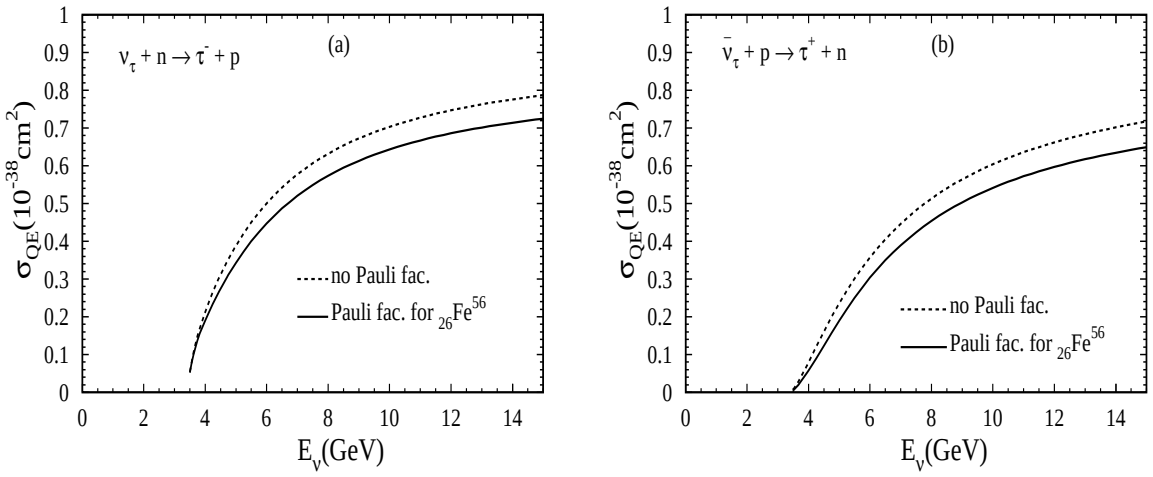

Figure 3.11: The cross section of QE for the (a) $\nu_\tau + n \to \tau^- + p$ and (b) $\bar{\nu}_\tau + p \to \tau^+ + n$ process plotted versus the incoming neutrino energy with and without Pauli factor.

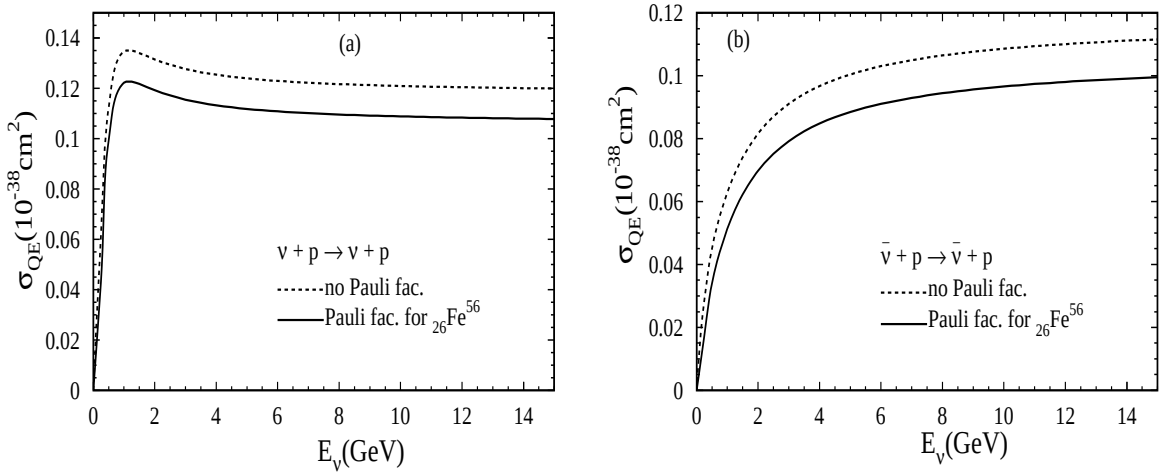

Figure 3.12: The same as in Fig. 3.11 for the (a) $\nu + p \to \nu + p$ and (b) $\bar{\nu}_\tau + p \to \bar{\nu} + p$ process.

3.4.3 Resonance Production

Resonance production induced by ν_μ neutrinos was studied in chapter 2. Here we extend our analysis to the production of τ's and their associated threshold effects. Resonance production provides an additional signature, because in this case there is also a pion in the final state. For CC reactions the signal will be a lepton and a charged pion in the final state, while the neutral currents will search for a single pion. The nuclear effects are expected to be larger because the pions have a chance of rescattering within the nucleus [30]. Fig. 3.13 (a) shows the various channels produced in the reactions

$$\nu_\tau + N \rightarrow \tau^- + N + \pi^{+,0} \tag{3.40}$$

and the corresponding reactions with anti-neutrinos are shown in Fig. 3.13 (b). The threshold is again at $E_\nu \approx 5.6$ GeV. The cross sections grow rapidly now, reaching their asymptotic values at $E_\nu \approx 15$ GeV. For a heavy target like iron the same features appear, but now there are nuclear effects like rescattering and charge-exchange, bringing a substantial reduction: a factor of 2 for π^+ (Fig. 3.14 (a)) and a change of 30 % for π^0 (Fig. 3.14 (b)) in ν_τ scattering. As already mentioned in chapter 2, due to charge exchange effects in nuclei also a small fraction of π^- is generated which we do not plot here. Similarly there is a reduction by a factor ~ 2 for π^- in the reaction in $\bar{\nu}_\tau$ scattering shown in Fig. 3.15. Again curves for the subdominant π^0 and π^+ production are not shown.

Finally, we plot in Figs. 3.16–3.21 differential pion energy spectra for various targets. Again, we consider the same cases, i.e. production of $\pi^{\pm,0}$ in CC scattering of ν_τ and $\bar{\nu}_\tau$ as in Fig. 3.14 and the remarks made there apply here as well. The pion spectra are significantly reduced by nuclear corrections reflecting the rescattering of the pions. In some cases the reduction is a whole factor of 2. It is also interesting to note that the reaction of the various channels is different than in the case of NC.

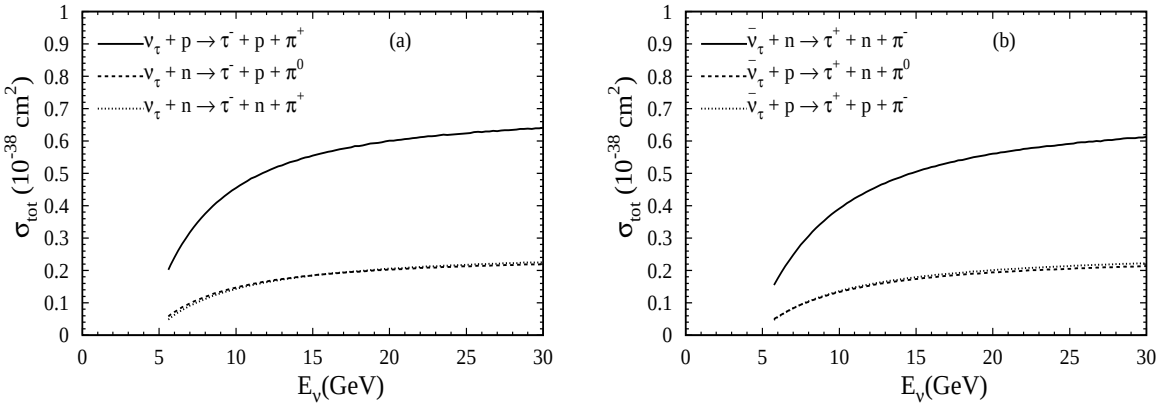

Figure 3.13: The cross section of RES for (a) $\nu_\tau + N \to \tau^- + N + \pi^{+,0}$ and (b) $\bar{\nu}_\tau + N \to \tau^+ + N + \pi^{-,0}$ plotted versus the incoming neutrino energy.

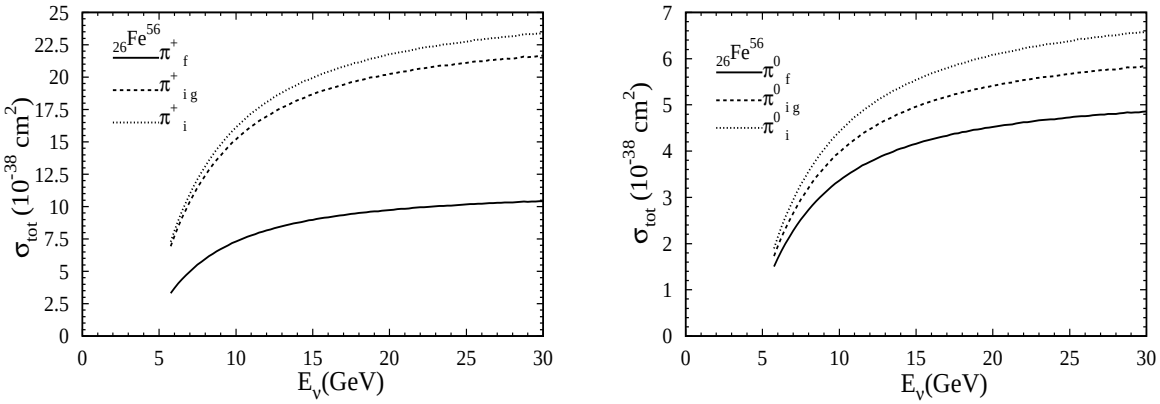

Figure 3.14: Total cross sections (resonance contributions) in CC τ-neutrino scattering off oxygen targets. Shown are in a) and b) cross sections for π^+ and π^0 production in ν_τ scattering. The solid, dashed and dotted lines represent all nuclear corrections, including only the Pauli production factor g and without any nuclear correction, respectively.

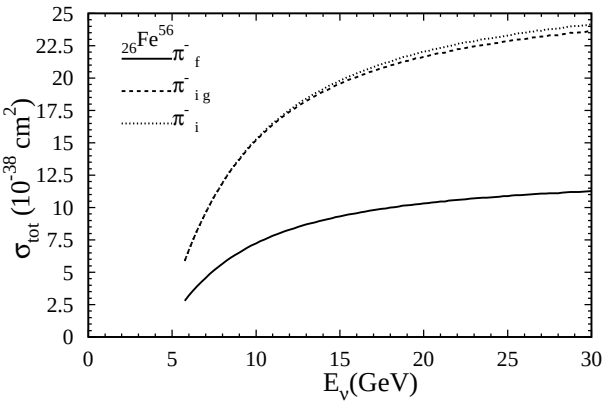

Figure 3.15: The same as in Fig. 3.14 is shown in the cross sections for π^- production in $\bar{\nu}_\tau$ scattering.

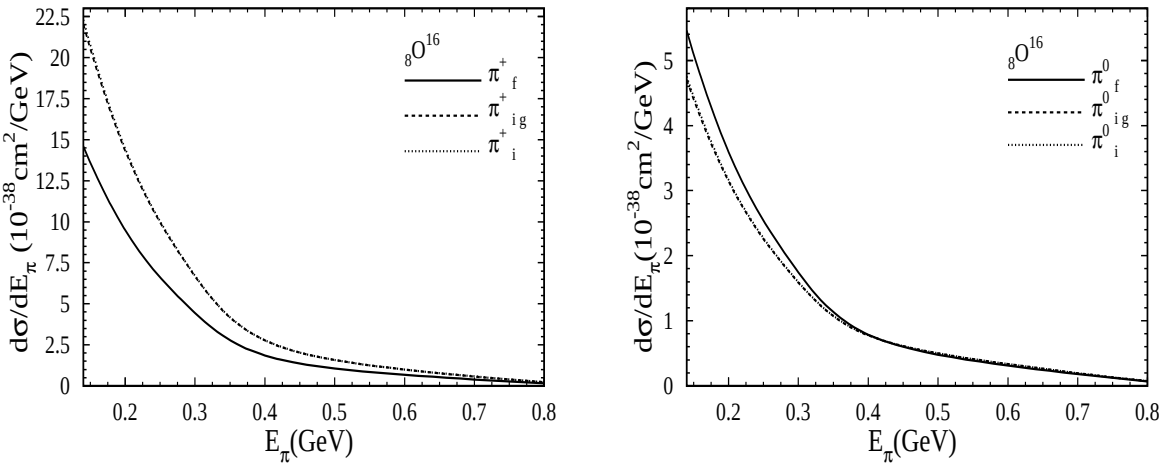

Figure 3.16: Pion energy distributions (the dominant resonance contributions) in CC τ-neutrino scattering off oxygen targets. Shown are in a) and b) pion energy distributions for π^+ and π^0 production in ν_τ scattering. The solid, dashed and dotted lines represent respectively the pion energy distributions including all nuclear corrections, including only the Pauli production factor g and without any nuclear correction.

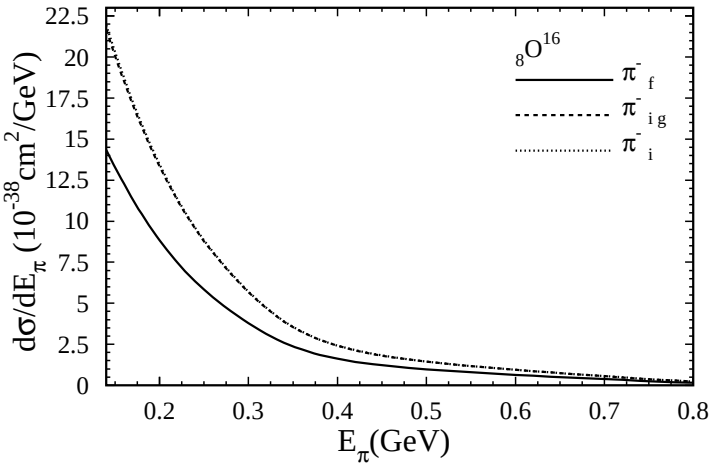

Figure 3.17: The same as in Fig. 3.16 is plotted for π^- production in $\bar{\nu}_\tau$ scattering.

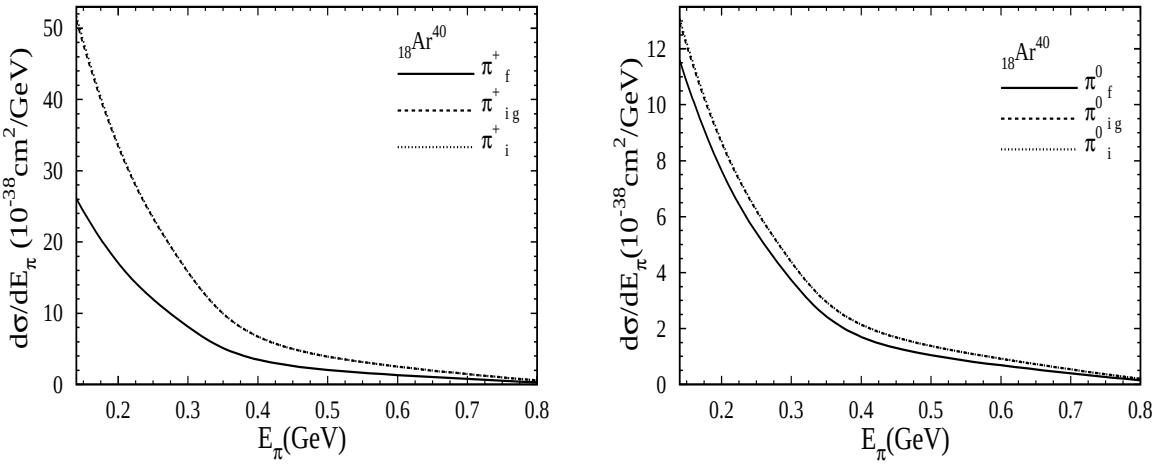

Figure 3.18: The same as in Fig. 3.16 for an argon target.

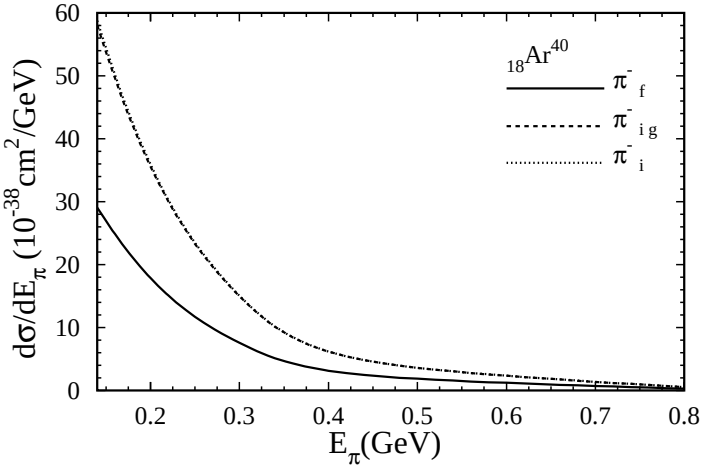

Figure 3.19: The same as in Fig. 3.17 for an argon target.

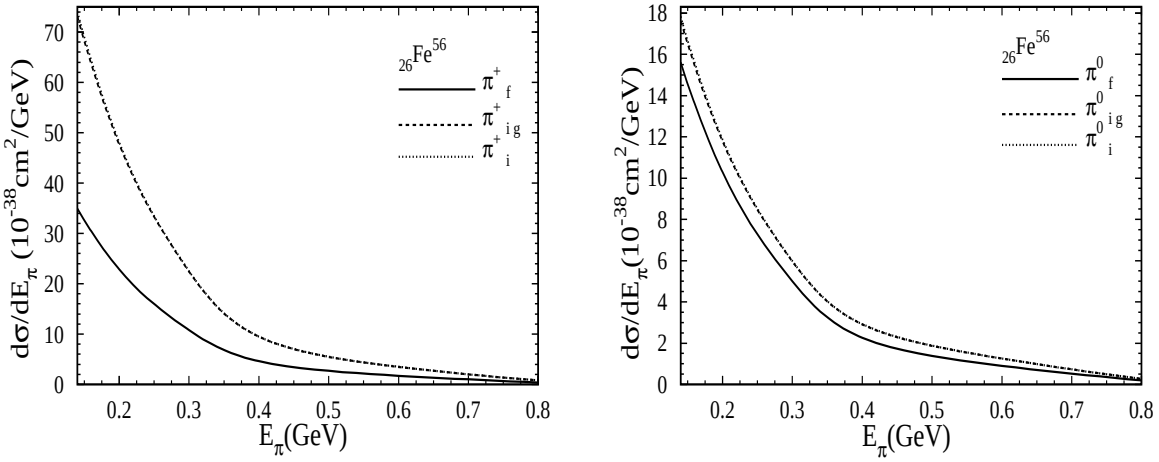

Figure 3.20: The same as in Fig. 3.16 for an iron target.

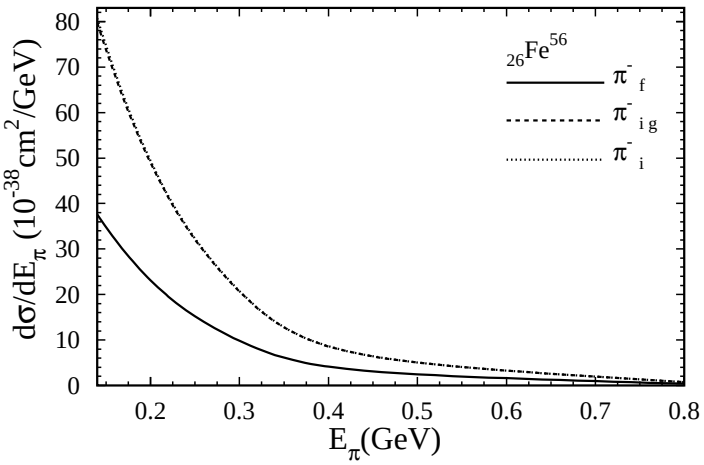

Figure 3.21: The same as in Fig. 3.17 for an iron target.

3.5 Event Rates

We calculated the τ-lepton event rates of the total cross section (RES+QE+DIS), concentrating on the OPERA LBL experiment [21]. The number of observable ν_τ charged current events, N_τ, using the CERN-NGS neutrino beam is given by the following equation:

$$N_\tau = A \int \phi_{\nu_\mu}(E_\nu) P_{osc}(\nu_\mu \to \nu_\tau) \sigma^{CC}_{\nu_\tau}(E_\nu) Br(\tau \to \text{lepton(l)}, \text{hadron(h)}) \epsilon(E_\nu) dE_\nu, \quad (3.41)$$

where ϕ_{ν_μ} is the muon neutrino flux at the Gran Sasso detector which we took from [97] and $\sigma^{CC}_{\nu_\tau}$ is the charged current total cross section for the ν_τ from our theoretical calculation. For the neutral current total cross section we replace $\sigma^{CC}_{\nu_\tau}$ by σ^{NC}_{ν}. The neutrino flux is appropriately normalized so that A is the total number of active protons plus neutrons in the target. It is referred to as the active target mass A and is given by $A = N_A \times 10^9 \times M_d \times N_p \times N_y$, where N_A is Avogadro's number. We take the detector mass $M_d = 1$ kton, the number of years for data taking $N_y = 4$ and the number of protons on target per year $N_p = 4.5 \times 10^{19}$ pot/year. In the two flavor mixing scheme we took the probability of $\nu_\mu \to \nu_\tau$ given by the following equation:

$$P_{osc}(\nu_\mu \to \nu_\tau) = \sin^2 2\theta \sin^2 \Big(\frac{1.27 \delta m^2 L}{E_\nu}\Big), \quad (3.42)$$

with $\sin^2 2\theta = 1$ and the distance L from CERN to Gran Sasso Laboratory is 730 km. We considered the neutrino energy range as 1 GeV $\leq E_\nu \leq$ 30 GeV and took $\delta m^2 = 10^{-3} - 10^{-2}\,\text{eV}^2$. We adopted the branching ratios $Br(\tau \to \text{lepton(l)}, \text{hadron(h)})$ and the detector efficiency ϵ of the ν_τ events from Ref. [98]. We did not consider background because the number of such events is expected to be very small, as can be seen from [21].

3.5.1 Results

We present the number of events, N_τ, for charged currents (Tables 3.1 and 3.2) and for neutral currents (Tables 3.3 and 3.4). In order to distinguish the various channels we give events for DIS, separately, and also the sum of DIS+QE+RES. Table 3.1 shows the number of charged current events for the oscillation parameters at two confidence levels with $\delta m^2 \simeq 10^{-3} - 5 \cdot 10^{-3}\,\text{eV}^2$ and $\sin^2 2\theta \geq 0.89$ taken from a recent global analysis [9]. In the first column is the total number of events without nuclear corrections. The second column shows events for DIS with nuclear corrections and the third one the total number

		N_τ	$N_\tau(nucl.forDIS)$	$N_\tau(nucl.forDIS+RES+QE)$
$90\%C.L.$	min	4.06	2.72	3.56
	max	30.72	20.92	26.67
$99\%C.L.$	min	2.33	1.55	2.04
	max	41.13	28.66	35.71

Table 3.1: The number of events N_τ at OPERA for the cross section for DIS and for the total cross section (QE+RES+DIS) with and without nuclear corrections. The table is for charged current channels with the 90% and 99% C.L. parameter set at the value $\delta m^2 \simeq 10^{-3} - 5 \cdot 10^{-3}\,\mathrm{eV}^2$ and $\sin^2 2\theta \geq 0.89$ of [9].

$\delta m^2(eV^2)$	N_τ	$N_\tau(nucl.forDIS)$	$N_\tau(nucl.forDIS+RES+QE)$
1.5×10^{-3}	2.69	1.8	2.36
3.0×10^{-3}	11.34	7.62	9.87
3.5×10^{-3}	15.57	10.49	13.53
4.5×10^{-3}	25.80	17.51	22.39
5.0×10^{-3}	31.72	21.60	27.53

Table 3.2: The number of events N_τ at OPERA for the cross section for DIS and for the total cross section (QE+RES+DIS) with and without nuclear corrections. These are charged current channels with $\sin^2 2\theta = 1$ and various δm^2.

of events with nuclear corrections. Table 3.2 shows charged currents events as a function of δm^2. The various columns include events classified in the same way as in Table 3.1.

In Tables 3.3 and 3.4 we present the neutral currents events. Table 3.3 includes the number of events again for two confidence levels and the various columns have the same meaning as above. Finally, Table 3.4 shows the number of events as a function of δm^2. The event numbers for charged current channels in Refs. [98, 99] are in reasonable agreement with our results. For the total number of events in QE+RES+DIS the reduction from nuclear corrections is $10-15\%$, mainly because nuclear corrections are significant for the resonance channels. Nuclear effects reduce RES and QE processes, but remain negligible for DIS processes. The contribution of QE and RES production to τ-appearance events, in charged currents, is approximately $20-24\%$ and, in neutral currents, about $13-15\%$.

		N_τ	$N_\tau(nucl.forDIS)$	$N_\tau(nucl.forDIS+RES+QE)$
$90\%C.L.$	min	6.89	5.26	6.15
	max	42.34	33.56	37.91
$99\%C.L.$	min	4.10	3.11	3.66
	max	55.21	43.98	49.46

Table 3.3: The number of events N_τ at OPERA for the cross section for DIS and for the total cross section (QE+RES+DIS) with and without nuclear corrections. These are neutral current channels with the 90% and 99% C.L parameter set at the value $\delta m^2 \simeq 10^{-3} - 5 \cdot 10^{-3}\,\mathrm{eV}^2$ and $\sin^2 2\theta \geq 0.89$ of [9].

$\delta m^2(eV^2)$	N_τ	$N_\tau(nucl.forDIS)$	$N_\tau(nucl.forDIS+RES+QE)$
1.5×10^{-3}	4.72	3.58	4.21
3.0×10^{-3}	17.45	13.54	15.59
3.5×10^{-3}	23.11	18.05	20.66
4.5×10^{-3}	36.26	28.63	32.45
5.0×10^{-3}	43.66	34.62	39.1

Table 3.4: The number of events N_τ at OPERA for the cross section for DIS and for the total cross section (QE+RES+DIS) with and without nuclear corrections. These are neutral current channels with $\sin^2 2\theta = 1$ and various δm^2.

3.6 Conclusions

Neutrino oscillation experiments face the problem that the number of events is very small. This limitation is more severe for τ-appearance experiments, which motivated to design experiments with heavy nuclei as targets. The number of events will now increase substantially, given by $(A-Z)\sigma_n + Z\sigma_p$ with $\sigma_{p,n}$ being the cross sections on free protons and neutrons, respectively. This substantial increase is slightly complicated by nuclear target effects. In this paper we calculated several cross sections and showed how the nuclear effects can be understood and compensated for.

The role of the various reactions is distinct. For energies $E_\nu < 2.5$ GeV the μ^- - production and neutral current reactions receive comparable contributions from three types of reactions: quasi-elastic, resonance production and deep inelastic scattering. The analysis of the data must include all three of them and try to identify unique signatures:

- In quasi-elastic scattering there is a single nucleon in the final state, which is unique but hard to detect.
- In resonance production there is a nucleon and a pion, whose decay gives a unique signature. The produced pions may be further identified and confirmed by their specific energy spectra as plotted in Figs. 3.16–3.21.
- For $E_\nu > 2.5$ GeV deep inelastic scattering dominates the ν_μ reactions. For comparison, the τ-lepton events have a characteristic threshold dependence.

There are no τ-leptons produced for $E_\nu < 5.6$ GeV. For the ν_τ beams quasi-elastic and resonance production are important for energies E_ν up to 6.5 GeV to 7.0 GeV. Above this energy (see Fig. 3.6) the deep inelastic reaction dominates.

In the resonance region our results of the nuclear effects for neutral currents were presented in chapter 2. In this section we extended the calculations to τ-appearance experiments and we can summarize them as follows:

- Nuclear effects are very small for deep inelastic reactions and can be neglected.
- For quasi-elastic scattering the main effect is the Pauli suppression factor, which reduces the rates by 10–12 % (See Figs. 3.11 and 3.12).
- Nuclear corrections are substantial in single-pion production at the resonance region. They vary from channel to channel and for this reason we produced Figs. 3.13–3.15 showing the production cross sections and Figs. 3.16–3.21 showing the pion spectra. A striking feature in all of the cross sections is the τ-lepton threshold.

We also made an extensive search of earlier publications trying to find data for possible experimental comparisons. In spite of our efforts we could not find data for a meaningful test of nuclear corrections. Thus it is advisable for the nearby detectors of the LBL experiments to collect data on heavy nuclei and test the models [30, 38]. The required comparisons are evident from this thesis and the article [30].

Chapter 4

Summary

The future long base line experiments will look for neutrino oscillations and are constructed with nuclei targets. The neutrino energies will be typically at most 10 GeV. Therefore it is important to study neutrino induced, both, charged and neutral current cross sections relevant for neutrino oscillation experiments including nuclear modifications.

In Part I of this thesis we have presented all relevant formulas and cross sections for the scattering of muon- and tau neutrinos on free nucleons, taking into account the τ-lepton threshold effects. There are three types of reactions contributing to these cross sections: deep inelastic scattering, quasi-elastic scattering and single pion production in the resonance region. Furthermore, using these results for free nucleon targets, we have evaluated the nuclear effects occurring in heavy nuclei targets.

The role of deep inelastic scattering, quasi-elastic scattering and resonance production is distinguished by the neutrino energy range. In the low neutrino energy range ($E_\nu < 2.5$ GeV) all three types of the reactions have comparable contributions, while deep inelastic scattering dominates in the high neutrino energy range. Due to threshold effects, tau leptons are produced above the neutrino energy $E_\nu > 5.6$ GeV. Still the contributions of quasi-elastic scattering and resonance production are important for E_ν up to 7.0 GeV.

The nuclear effects are sizable and large in the resonance production reactions and moderate slightly for the quasi-elastic scattering, while they are small in deep inelastic scattering.

Finally, we have calculated the τ event rates for the OPERA long base line experiment with and without any nuclear corrections.

Our results will be useful studying single pion production and for investigating neutrino oscillations in future experiments.

Part II

The Nonperturbative Dispersive Sector in Strong (Quasi-)Abelian Fields

Chapter 5

Introduction and Survey

It has been well known for some time that the effects of the fermionic quantum fluctuations in space–time uniform Abelian gauge fields can be effectively integrated out, resulting in a one–loop effective action [100–106]. The results have been formulated also for the covariant homogeneous, thus quasi–Abelian, fields of the $SU(2)$ gauge group [107], and for specific nonhomogeneous magnetic field configurations [108]. All the results can be extended to the case of the quantum fluctuations of scalar particles. The problems arising when genuinely non–Abelian fields with translationally invariant gauge–invariants are present [e.g., in $SU(3)_c$] were discussed, e.g., in Refs. [109, 110].

The quantum fluctuations of the strong gauge field itself (photons, or gluons) modify additionally those Lagrangian densities induced by the fermionic quantum fluctuations. Such two-loop effects have been successfully derived by Ritus [111] for homogeneous Abelian fields, and further discussed by others [112, 113]. In QED, such two–loop effects in the coupling constant change the one–loop result by at most a few per cent. We will omit them in our investigation.

There are basically two classes of phenomena associated with the presence of intense gauge fields.

Firstly, they can produce pairs of particles. For the case of strong Abelian homogeneous electric fields this was shown by Sauter [114] by investigating solutions of the Dirac equation in the corresponding potential [1], and by Schwinger [102] by using methods of action integral, Green's functions and proper time. Differential probabilities for pair cre-

[1] A related problem was first considered even earlier by Klein [115] who investigated solutions of the Dirac equation with a high vertical barrier potential (Klein's paradox).

ation were investigated in Refs. [116] and [117]. In the latter reference, the quasi–Abelian model was applied to an investigation of the quark pair production in chromoelectric flux tubes. Experimental evidence related with the pair production in a strong QED (laser) field was reported in Ref. [118].

The pair production has its origin in the imaginary (absorptive) part of the effective Lagrangian induced by the fermionic quantum fluctuations in the strong field. That part is entirely nonperturbative in nature, because the production effects are $\sim\exp(-\text{const.}/g)$ and thus cannot be expanded in positive powers of the field–to–fermion coupling constant g.

On the other hand, the other class of phenomena is associated with the real (dispersive) part of the induced effective Lagrangian. In QED, this class includes the following phenomena that affect a low energy ($\omega \ll m_e$) photon wave entering the region of the strong background field: photon splitting, change of the photon speed, and birefringence. Studies on the theoretical aspects of these phenomena can be found in Refs. [119–123]. The experimental aspects of birefringence in strong magnetic fields are discussed in [124, 125]. The dispersive part of the induced action leads in principle to those corrections of the classical Maxwell equations which originate from the (fermionic) quantum fluctuations.

Our investigation in the second part of this thesis, while dealing with the dispersive part of the induced action, is somewhat different from these works. We concentrate on the concept of separating the nonperturbative from the perturbative contributions in the induced dispersive action when the product of the (quasi)electric field $\mathcal{E}$ and the coupling constant g is large: $g\mathcal{E}/m^2 \gtrsim 1$, where m is the fermion mass. Subsequently, we numerically investigate the two contributions. Afterwards, we use the discussed quantities as a "laboratory" for testing and investigating the efficiency of methods of quasianalytic continuation. The latter methods, involving the (modified) Borel-Padé approximants, allow us to obtain approximately the nonperturbative contributions from the approximate knowledge of the perturbative contributions and by employing the Cauchy principal value prescription in the inverse Borel transformation (Laplace–Borel integral). These considerations can give us insights into the problems of extraction of nonperturbative physics from the knowledge of perturbative physics in gauge theories, in particular in various versions of QCD.

Alternatively, the Weniger (delta sequence) method has been proposed by the authors of Ref. [126] for the resummation of truncated perturbation series (TPS) in quantum field

theories. They presented numerical evidence suggesting that this method works better than the Padé approximants when we resum a function with singularities in the Borel plane but not on the positive axis. We compare the efficiency of the Borel-Padé method with the Borel-Weniger method for resummation of TPS in some physically significant scenarios. The scenarios we are referring to are those when the function, which we want to find through a resummation, is known to have a certain singularity structure in the Borel plane. If there are singularities on the positive axis of the Borel plane, then we implicitly assume that in such cases we either know the correct prescription for integration in the Laplace-Borel integral, or we simply adhere to a certain adopted prescription.

The outline of Part II will be as follows.
Chapter 6 is constructed by:

- In section 6.1 we present the derivation of the Euler-Heisenberg Lagrangian density in a homogeneous strong (quasi) Abelian field using the path-integral formalism.
- In section 6.2, we argue how to perform the mentioned separation into the perturbative and nonperturbative contributions for arbitrary strength of the field in the one-loop case. After identifying the two contributions, we investigate numerically their values for various values of the field parameter $\tilde{a} \sim g\mathcal{E}/m^2$.
- In section 6.3 we then carry out an analogous analysis for the induced energy density, that is in principle observable.
- In section 6.4 we then numerically investigate, for the induced Lagrangian and energy densities, (quasi)analytic continuation from the perturbative into the nonperturbative sectors, employing the method of Borel–Padé for the induced Lagrangian and a modified Borel–Padé for the induced energy density. We encounter integrations over renormalon poles, whose origin is nonperturbative, and we show how to carry it out.
- In section 6.5 we illustrate the efficiency of the Borel-Padé and Borel-Weniger method on the Euler-Heisenberg Lagrangian density and the Bjorken polarized sum rule, and compare some numerical results for both methods.

Chapter 7 summarizes our results and conclusions.

Chapter 6

The Nonperturbative Dispersive Sector in Strong (Quasi-)Abelian Fields

6.1 Derivation of the Euler-Heisenberg Lagrangian Density

In this section we calculate the Euler-Heisenberg Lagrangian density in an arbitrarily strong homogeneous (quasi-) Abelian field according to [106] and [127] involving the path-integral method to the probability density and considering one-dimensional harmonic oscillators to evaluate the traces.

6.1.1 Probability Density

The probability density per unit time for producing a fermion-antifermion pair ($w = \frac{\mathrm{d}P}{\mathrm{d}V\,\mathrm{d}t}$) is as follows:

$$w \equiv \frac{\mathrm{d}P}{\mathrm{d}x} = -\frac{1}{\Omega}\ln|S_0(A)|^2 = -\frac{2}{\Omega}\mathrm{Re}\ln S_0(A), \tag{6.1}$$

where $x = (x^0, \vec{x})$, Ω is the large four-dimensional space-time volume in the presence of the field, and $S_0(A)$ is the vacuum to vacuum amplitude in the presence of an external present electromagnetic field A. $S_0(A)$ can be conveniently described using path integrals in the following way:

$$S_0(A) \equiv \langle 0_{in}|\hat{S}(A)|0_{in}\rangle = \langle 0_{out}|0_{in}\rangle^{(A)} = \frac{Z(A)}{Z(0)}, \tag{6.2}$$

where

$$Z(A) = \int \mathrm{D}\bar{\Psi}\mathrm{D}\Psi e^{i\int \mathrm{d}^4x[i\bar{\Psi}(\not{\partial}+\mathrm{i}m+\mathrm{i}g\not{A})\Psi]}. \tag{6.3}$$

with the Grassmann variable Ψ, the field–to–fermion coupling parameter g (in electromagnetism it is the positron charge e_0), and the mass of the (lightest) fermion m.

Specifically, we take the field A as follows:

$$A_\mu = -\frac{1}{2}F_{\mu\nu}x^\nu, \tag{6.4}$$

where $F_{\mu\nu}$ is the antisymmetric tensor for the homogeneous electromagnetic field:

$$F^{\mu\nu} = \partial^\mu A^\nu - \partial^\nu A^\mu = \begin{bmatrix} 0 & -\mathcal{E}^1 & -\mathcal{E}^2 & -\mathcal{E}^3 \\ \mathcal{E}^1 & 0 & -\mathcal{B}^3 & \mathcal{B}^2 \\ \mathcal{E}^2 & \mathcal{B}^3 & 0 & -\mathcal{B}^1 \\ \mathcal{E}^3 & -\mathcal{B}^2 & \mathcal{B}^1 & 0 \end{bmatrix} . \tag{6.5}$$

For our purpose we take the electric field $\vec{\mathcal{E}} = (0,0,\mathcal{E})$ (with $\mathcal{E} > 0$), and the magnetic field $\vec{\mathcal{B}} = (0,0,\mathcal{B}_\parallel)$ without loss of the generality. Namely, there always exists a Lorentz boost such that in the boosted frame the electric and magnetic fields are aligned. The probability density (6.1), and in general $(1/\Omega)\ln S_0(A)$, are invariant under the boost. With help of Eq. (6.4) and a gauge transformation $G = \exp[g(-\mathcal{E}x^3x^0 + \mathcal{B}_\parallel x^2x^1)/4]$ the field A is obtained as:

$$A^\mu = (0,0,\mathcal{B}_\parallel x^1, -\mathcal{E}x^0) \ . \tag{6.6}$$

Using Eqs. (6.2-6.3), the probability density w in Eq. (6.1) can be expressed in the following way:

$$w = -\frac{1}{\Omega}\mathrm{Re}\left\{\mathrm{Tr}\ln\left[(\hat{\not{P}} - g\not{A})^2 - (m-\mathrm{i}\varepsilon)^2\right] - \mathrm{Tr}\ln\left[\hat{\not{P}}^2 - (m-\mathrm{i}\varepsilon)^2\right]\right\} \ , \tag{6.7}$$

where Tr denotes tracing over all relevant degrees of freedom. Using the identity

$$(\hat{\not{P}} - g\not{A})^2 = (\hat{P} - gA)^2 - \frac{g}{2}\sigma_{\mu\nu}F^{\mu\nu} \ , \tag{6.8}$$

where $\sigma_{\mu\nu} = \frac{\mathrm{i}}{2}[\gamma_\mu,\gamma_\nu]$ and the Schwinger integral representation for logarithms in terms of proper time s, we obtain from (6.7):

$$w \ = \ \mathrm{Re}\int_0^\infty \frac{\mathrm{d}s}{s}\exp\left[-\mathrm{i}s\left(m^2-\mathrm{i}\varepsilon\right)\right]\left\{\mathrm{Tr}\Big\langle x\Big|\exp\left[\mathrm{i}s\left(\hat{P}-gA(\hat{X})\right)^2\right]\times\right.$$

$$\exp\left[-\mathrm{i}s\,(g/2)\,\sigma_{\mu\nu}F^{\mu\nu}\right]\Big|x\Big\rangle - \mathrm{Tr}\left\langle x\left|\exp\left[\mathrm{i}s\hat{P}^2\right]\right|x\right\rangle\Bigg\}\,. \tag{6.9}$$

In order to obtain this result we canceled $\int \mathrm{d}^4x$ with the Ω in the denominator because w is independent of x. We have written $(m-\mathrm{i}\varepsilon)^2$ in Eq. (6.7) in the equivalent form $(m^2-\mathrm{i}\varepsilon)$, where the infinitesimal $\varepsilon=+0$ ensures convergence of the integral. Due to the homogeneity of the gauge field A, we can calculate Eq. (6.9) explicitly. In order to solve Eq. (6.9) we start to derive the trace term $\mathrm{Tr}\,e^{[-\mathrm{i}s(g/2)\sigma_{\mu\nu}F^{\mu\nu}]}$. The explicit calculation of $(\sigma_{\mu\nu}F^{\mu\nu})^2$, using the anticommutator relation $\frac{1}{2}\{\sigma_{\alpha\beta},\sigma_{\mu\nu}\} = g_{\alpha\mu}g_{\beta\nu} - g_{\alpha\nu}g_{\beta\mu} - i\varepsilon_{\alpha\beta\mu\nu}\gamma_5$ from [105], can be further evaluated:

$$\begin{aligned}(\sigma_{\mu\nu}F^{\mu\nu})^2 &= 4\left(\mathcal{E}\sigma_{30}+\mathcal{B}_{\parallel}\sigma_{21}\right)^2\\ &= 4\left[\left(-\vec{\mathcal{E}}^2+\vec{\mathcal{B}}^2\right)-2\mathrm{i}\gamma_5\left(\vec{\mathcal{E}}\cdot\vec{\mathcal{B}}\right)\right]\,.\end{aligned} \tag{6.10}$$

It is convenient to use the following Lorentz-invariant notation:

$$\mathcal{F} = \frac{1}{4}F^{\mu\nu}F_{\mu\nu} = \frac{1}{2}\left(\vec{\mathcal{B}}^2-\vec{\mathcal{E}}^2\right)\,, \tag{6.11}$$

$$\mathcal{G} = -\frac{1}{4}F^{\mu\nu}\tilde{F}_{\mu\nu} = \left(\vec{\mathcal{E}}\cdot\vec{\mathcal{B}}\right)\,, \tag{6.12}$$

where $\tilde{F}_{\mu\nu}\equiv\frac{1}{2}\varepsilon_{\mu\nu\alpha\beta}F^{\alpha\beta}$. We expand $\mathrm{Tr}\,\exp\left[-\mathrm{i}s(g/2)\sigma_{\mu\nu}F^{\mu\nu}\right]$ using relation in (6.10) and tracelessness of $\sigma_{\mu\nu},\gamma_5$ and of $\gamma_5\sigma_{\mu\nu}$:

$$\begin{aligned}\mathrm{Tr}\,\exp\left[-\mathrm{i}s(g/2)\sigma_{\mu\nu}F^{\mu\nu}\right] &= 4\Bigg\{1-\frac{g^2 2^1 s^2}{2!}\mathcal{F}+\frac{g^4 2^2 s^4}{4!}\left(\mathcal{F}^2-\mathcal{G}^2\right)+\ldots\\ &\quad+(-1)^n\frac{g^{2n}2^n s^{2n}}{(2n)!}[\mathcal{F}^n-\binom{n}{2}\mathcal{F}^{n-2}\mathcal{G}^2+\ldots\\ &\quad+(-1)^k\binom{n}{2k}\mathcal{F}^{n-2k}\mathcal{G}^{2k}+\ldots]+\ldots\Bigg\}\\ &= 2\Bigg\{(1+1)-\frac{g^2 2^1 s^2}{2!}\left[(\mathcal{F}-\mathrm{i}\mathcal{G})+(\mathcal{F}+\mathrm{i}\mathcal{G})\right]\\ &\quad+\frac{g^4 2^2 s^4}{4!}\left[(\mathcal{F}-\mathrm{i}\mathcal{G})^2+(\mathcal{F}+\mathrm{i}\mathcal{G})^2\right]+\ldots\\ &\quad+(-1)^n\frac{g_s^{2n}2^n s^{2n}}{(2n)!}\left[(\mathcal{F}-\mathrm{i}\mathcal{G})^n+(\mathcal{F}+\mathrm{i}\mathcal{G})^n\right]+\ldots\Bigg\}\\ &= 2\left\{\cos\left[gs\sqrt{2(\mathcal{F}-\mathrm{i}\mathcal{G})}\right]+\cos\left[gs\sqrt{2(\mathcal{F}+\mathrm{i}\mathcal{G})}\right]\right\}.\end{aligned} \tag{6.13}$$

We now set $2(\mathcal{F}\pm\mathrm{i}\mathcal{G})=(b\pm\mathrm{i}a)^2$, where the parameters a and b are Lorentz–invariant expressions characterizing the (quasi-)electric and the (quasi-)magnetic fields $\vec{\mathcal{E}}$ and $\vec{\mathcal{B}}$, respectively:

$$a = \left[+\vec{\mathcal{E}}^2-\vec{\mathcal{B}}^2+\sqrt{\left(\vec{\mathcal{E}}^2-\vec{\mathcal{B}}^2\right)^2+4\left(\vec{\mathcal{E}}\cdot\vec{\mathcal{B}}\right)^2}\right]^{1/2}/\sqrt{2}\,, \tag{6.14}$$

$$b = \left[-\vec{\mathcal{E}}^2+\vec{\mathcal{B}}^2+\sqrt{\left(\vec{\mathcal{E}}^2-\vec{\mathcal{B}}^2\right)^2+4\left(\vec{\mathcal{E}}\cdot\vec{\mathcal{B}}\right)^2}\right]^{1/2}/\sqrt{2}\,. \tag{6.15}$$

Therefore, we can rewrite (6.14) as

$$\begin{aligned}\mathrm{Tr}\,\exp\left[-\mathrm{i}s(g/2)\sigma_{\mu\nu}F^{\mu\nu}\right] &= 2\left\{\cos\left[(b-\mathrm{i}a)\,gs\right]+\cos\left[(b+\mathrm{i}a)\,gs\right]\right\}\\ &= 4\cosh\left(ags\right)\cos\left(bgs\right)\ .\end{aligned} \tag{6.16}$$

We note that $ab=|\vec{\mathcal{E}}\cdot\vec{\mathcal{B}}|$, and $a^2-b^2=\vec{\mathcal{E}}^2-\vec{\mathcal{B}}^2$. Further, $a\to|\vec{\mathcal{E}}|$ when $|\vec{\mathcal{B}}|\to 0$, and $b\to|\vec{\mathcal{B}}|$ when $|\vec{\mathcal{E}}|\to 0$. In the Lorentz frame where $\vec{\mathcal{B}}\|\vec{\mathcal{E}}$, we simply have: $a=|\vec{\mathcal{E}}|$ and $b=|\vec{\mathcal{B}}|$.

The other term on the right-hand side in Eq. (6.9) can be obtained using a unitary transformation $\hat{U}$ into a sum of two harmonic oscillator Hamiltonian densities:

$$\begin{aligned}\hat{U}\left[\hat{P}-gA(X)\right]^2\hat{U}^\dagger &= \left[\hat{P}^0\hat{P}^0-g^2a^2\hat{X}^0\hat{X}^0\right]-\left[\hat{P}^1\hat{P}^1+g^2b^2\hat{X}^1\hat{X}^1\right]\\ &= 2\mathcal{H}^{(1)}-2\mathcal{H}^{(2)},\end{aligned} \tag{6.17}$$

where $\mathcal{H}^{(1)}\equiv\left[\frac{1}{2}(\hat{P}^0\hat{P}^0-g^2a^2\hat{X}^0\hat{X}^0)\right]$ and $\mathcal{H}^{(2)}\equiv\left[\frac{1}{2}(\hat{P}^1\hat{P}^1+g^2b^2\hat{X}^1\hat{X}^1)\right]$.

The unitary operator $\hat{U}$ is constructed in appendix F. Inserting (6.17) and (6.16) into expression (6.9), and using unitarity of $\hat{U}$ and completeness of the four-momentum states $|q\rangle$, we obtain:

$$\begin{aligned}w=4\,\mathrm{Re}\int_0^\infty\frac{\mathrm{d}s}{s}\exp\left[-\mathrm{i}s\left(m^2-\mathrm{i}\varepsilon\right)\right]\Bigg\{&\cosh\left(ags\right)\cos\left(bgs\right)\times\\ &\iint\mathrm{d}^4q\mathrm{d}^4q'\left\langle x\left|\hat{U}^\dagger\right|q\right\rangle\left\langle q^2\middle|q'^2\right\rangle\left\langle q^3\middle|q'^3\right\rangle\left\langle q^0\left|\exp\left[2\mathrm{i}s\mathcal{H}^{(1)}\right]\right|q'^0\right\rangle\times\\ &\left\langle q^1\left|\exp\left[-2\mathrm{i}s\mathcal{H}^{(2)}\right]\right|q'^1\right\rangle\left\langle q'\left|\hat{U}\right|x\right\rangle\ -\ \ldots\Bigg\}\,,\end{aligned} \tag{6.18}$$

where the dots stand for the same expression but with no field ($a,b\mapsto 0$). We note that the integrations over q'^2 and q'^3 in (6.18) are trivial because $\langle q^j|q'^j\rangle=2\pi\delta(q^j-q'^j)$. Using

the relation $\langle x|q\rangle = \exp[-ix\cdot q]/(2\pi)^2$, the matrix elements are evaluated as follows:

$$\left\langle x\left|\hat{U}^\dagger\right|q\right\rangle = \frac{1}{(2\pi)^2}\exp(-iq\cdot x)\exp(-\frac{i}{gE}q^0q^3)\exp(-\frac{i}{gB_\parallel}q^1q^2) \tag{6.19}$$

and for $\left\langle q'|\hat{U}|x\right\rangle$ we replace $q^0 \mapsto q'^0$ and $q^1 \mapsto q'^1$ in the complex conjugate of the right-handed side of Eq. (6.19). It is subsequently shown that the integrations over q^2, q^3, q'^0 and q'^1 can be explicitly performed, leading to:

$$w = \frac{1}{4\pi^2}\mathrm{Re}\int_0^\infty \frac{\mathrm{d}s}{s}\exp\left[-\mathrm{i}s\left(m^2-\mathrm{i}\varepsilon\right)\right]\left\{4g^2a\,b\cosh\left(ags\right)\cos\left(bgs\right)\times\right.$$
$$\left.\int \mathrm{d}q^0\left\langle q^0\left|\exp\left[2\mathrm{i}s\mathcal{H}^{(1)}\right]\right|q^0\right\rangle\int \mathrm{d}q^1\left\langle q^1\left|\exp\left[-2\mathrm{i}s\mathcal{H}^{(2)}\right]\right|q^1\right\rangle - \ldots\right\}, \tag{6.20}$$

where dots denote the analogous term with zero fields. The expressions in the above parentheses in the exponents are in fact Hamiltonian densities for harmonic oscillators with mass parameter $m=1$ and with frequency parameters $\omega=\mathrm{i}ga$ and $\omega=gb$, respectively. Integration over dq^0 (dq^1) amounts to tracing over configuration space for exponents of these oscillators. Since the result of tracing is independent of the chosen basis, it is convenient to choose for the basis the known eigenstates of these oscillators. This leads to a discrete geometric sum, as shown explicitly in appendix G, and results in:

$$\begin{aligned} w &= \frac{1}{16\pi^2}\mathrm{Re}\int_{-\mathrm{i}\varepsilon'}^{\infty-\mathrm{i}\varepsilon'}\mathrm{d}z\frac{1}{\mathrm{i}\,z}\exp\left[-\mathrm{i}z\left(m^2-\mathrm{i}\varepsilon\right)\right]\times \\ &\quad\left\{\left[\frac{4g^2a\,b\cosh\left(agz\right)\cos\left(bgz\right)}{\sinh\left(agz\right)\sin\left(bgz\right)}\right]-\frac{4}{z^2}\right\}. \end{aligned} \tag{6.21}$$

The factor 4 in the last (zero-field) term in (6.21) arises from tracing over spinor degrees of freedom. In the above expression, when compared with (6.20), we moved the integration slightly (infinitesimally) below the positive real axis ($s\mapsto z=s-\mathrm{i}\varepsilon'$), in order to ensure that the geometric sum originating from tracing over $\mathrm{d}q^1$ (appendix G) converges. At this point, it is convenient to rewrite the above integral as an integral along the entire real axis. Namely, if we denote the integrand as $I_\varepsilon(z)$, it is straightforward to show that $I_\varepsilon(-z^*)=[I_{-\varepsilon}(z)]^*$. Therefore, we can replace $\mathrm{Re}I_\varepsilon(z)$ by $[I_\varepsilon(z)+I_{-\varepsilon}(-z^*)]/2$. If we perform in addition the limit $\varepsilon\to 0$, we obtain the final result:

$$w = \frac{1}{8\pi^2}\int_{-\infty-\mathrm{i}\varepsilon'}^{+\infty-\mathrm{i}\varepsilon'}\frac{\mathrm{d}z}{\mathrm{i}\,z}\exp\left(-\mathrm{i}zm^2\right)\left\{\left[\frac{g^2a\,b\cosh\left(agz\right)\cos\left(bgz\right)}{\sinh\left(agz\right)\sin\left(bgz\right)}\right]-\frac{1}{z^2}\right\}. \tag{6.22}$$

It should be noted that taking the limit $\varepsilon\to 0$ in the mass terms $m^2\pm\mathrm{i}\varepsilon$ appearing in the exponent is legitimate only if the resulting total integral above is convergent.

6.2 Induced Dispersive Lagrangian Density

The Euler-Heisenberg Lagrangian density $\delta\mathcal{L}$, which is the part induced by the quantum fluctuations of the fermions in an arbitrarily strong (quasi-)Abelian homogeneous field, is obtained from the vacuum–to–vacuum amplitude $S_0(A)$of Eq. (6.2) by the simple relation $\delta\mathcal{L} = (-i/\Omega)\ln S_0(A)$. As mentioned before, this expression is Lorentz-invariant as well. Comparison with Eq. (6.1) then tell us that we obtain $\delta\mathcal{L}$ from the probability density w, e.g., from Eq. (6.21), by removing 'Re' and by multiplying then by $(i/2)$. This gives us:

$$\begin{aligned}\delta\mathcal{L} &= \frac{1}{8\pi^2}\int_{-\mathrm{i}\epsilon}^{\infty-\mathrm{i}\epsilon}\frac{\mathrm{d}s}{s}\exp[-\mathrm{i}s(m^2-\mathrm{i}\varepsilon')]\times \\ &\left[g^2ab\coth(ags)\cot(bgs)-\frac{g^2}{3}(a^2-b^2)-1/s^2\right]\ . \end{aligned} \tag{6.23}$$

Note that the term $\propto (a^2-b^2)$ in (6.23) had to be added in order to cure a divergence. It can be shown to lead to field strength renormalization.

As denoted, the integration in (6.23) is performed along the positive real axis infinitesimally below it, avoiding in this way the poles on the real axis appearing due to the (Lorentz–invariant version of the) magnetic field b. If the path in (6.23) were above the real axis, then we would obtain a nonzero imaginary part of the Lagrangian density even in the pure magnetic field case. This would imply particle creation in this case, which is physically unacceptable. The path in (6.23) reproduces for the case of the pure magnetic field the known real density, and for the case of the pure electric field the known complex density [102]. The path in (6.23) is suggested also from the extension of the formal approach of Ref. [106] to the general $ab\neq 0$ case. Namely, when $ab\neq 0$, we need to evaluate in this approach two traces:

- One trace originating from $a\neq 0$ and discussed in [106] [their Eq. (4-116)].
- The other trace of the evolution operator of an harmonic oscillator, originating from $b\neq 0$ [127], of the form $\sum_{n=0}^{\infty}\exp[-2\mathrm{i}sgb(n+1/2)]$, $s>0$.

The latter trace becomes convergent after regularization $s\mapsto s-\mathrm{i}\epsilon$ $(\epsilon\to+0)$, i.e., the path in (6.23).

Performing a contour integration in the fourth quadrant of the complex proper–time

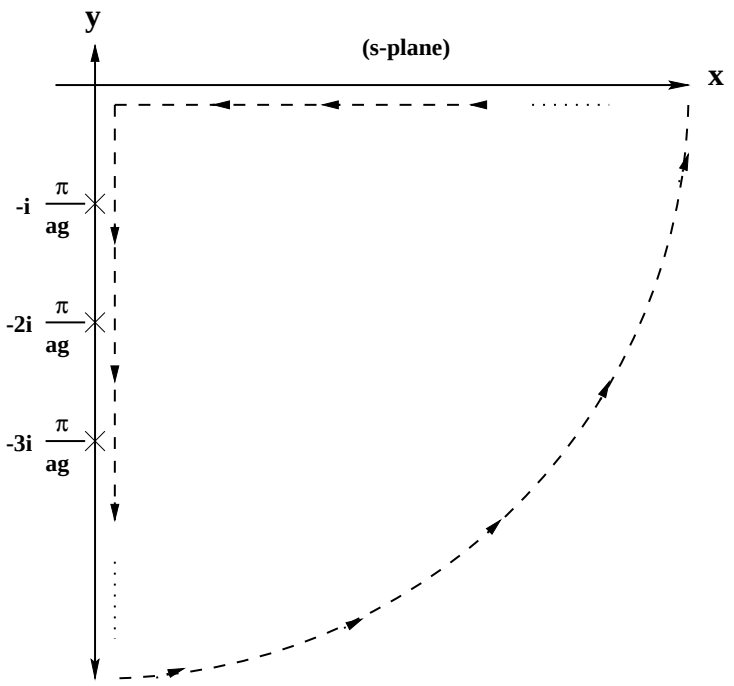

Figure 6.1: The contour integration, in the complex s–plane, needed to rewrite (6.23) in the form (6.24). The location of the poles is denoted explicitly.

s–plane (cf. Fig. 6.1), expression (6.23) can be rewritten as

$$\delta\mathcal{L} = -\frac{1}{8\pi^2}\int_{+0}^{\infty}\frac{\mathrm{d}z}{(z+\mathrm{i}\epsilon)}\mathrm{e}^{-zm^2}\times \left[g^2ab\cot\left(ag(z+\mathrm{i}\epsilon)\right)\coth\left(bg(z+\mathrm{i}\epsilon)\right)+\frac{g^2}{3}(a^2-b^2)-\frac{1}{(z+\mathrm{i}\epsilon)^2}\right], \quad (6.24)$$

where $s=-\mathrm{i}z+\epsilon$ now runs along the negative imaginary axis (and $\epsilon\to+0$). As seen from Fig. 6.1, the result (6.24) is actually independent of the precise path of variable s in (6.23), as long as s in (6.23) runs close to the positive axis towards $s=+\infty$ and passes each positive pole on the right, i.e. precisely the class of the paths satisfying the physical condition that pure magnetic fields can not produce particles. In (6.23) and (6.24), the familiar [100] counterterm $\propto(a^2$–$b^2)$ $[=(\mathcal{E}^2$–$\mathcal{B}^2)]$ is included which makes the integral finite. This divergent term leads to the renormalization of the field in the leading Lagrangian density $\mathcal{L}^{(0)}=(\mathcal{E}^2-\mathcal{B}^2)/2$. We now divide the integration region into intervals for the integration variable agz: $i_0=[0,\pi/2]$, $i_1=[\pi/2,3\pi/2]$, …, $i_n=[(n-1/2)\pi,(n+1/2)\pi]$, …. Each interval, except i_0, contains in its middle one pole of the integrand. The

corresponding series for the real (dispersive) part of the Lagrangian density is:

$$\mathrm{Re}\delta\tilde{\mathcal{L}} = \mathrm{Re}\delta\tilde{\mathcal{L}}_0 + \sum_{n=1}^{\infty}\mathrm{Re}\delta\tilde{\mathcal{L}}_n \ , \tag{6.25}$$

$$\mathrm{Re}\delta\tilde{\mathcal{L}}_0 = -\int_0^{\pi/2}\frac{\mathrm{d}w}{w}\exp\left(-\frac{w}{\tilde{a}}\right)\left[p\cot(w)\coth(pw)+\frac{1}{3}(1-p^2)-\frac{1}{w^2}\right] \ , \tag{6.26}$$

$$\begin{aligned}\mathrm{Re}\delta\tilde{\mathcal{L}}_n = &-\exp\left(-\frac{n\pi}{\tilde{a}}\right)\left\{\int_{-\pi/2}^{\pi/2}\mathrm{d}w\exp\left(-\frac{w}{\tilde{a}}\right)\left[\frac{p\cot(w)\coth(p(w+n\pi))}{(w+n\pi)}\right.\right.\\ &\left.-\frac{p}{w}\frac{\coth(pn\pi)}{n\pi}+\frac{(1-p^2)}{3(w+n\pi)}-\frac{1}{(w+n\pi)^3}\right]\\ &\left.+\mathrm{Re}\int_{-\pi/2}^{\pi/2}\mathrm{d}w\exp\left(-\frac{w}{\tilde{a}}\right)\frac{1}{(w+\mathrm{i}\epsilon')}\frac{p\coth(pn\pi)}{n\pi}\right\} \ , \quad (n\geq 1) \ . \end{aligned} \tag{6.27}$$

Here, $\epsilon'\equiv\epsilon ga\rightarrow +0$, and we used the notation

$$\tilde{a}\equiv\frac{ga}{m^2} \ , \qquad \tilde{b}\equiv\frac{gb}{m^2}, \qquad p\equiv\frac{b}{a}\equiv\frac{\tilde{b}}{\tilde{a}} \ , \qquad \delta\tilde{\mathcal{L}}\equiv\delta\mathcal{L}/\left(\frac{m^4\tilde{a}^2}{8\pi^2}\right) \ , \tag{6.28}$$

and we introduced the dimensionless integration variable $w\equiv agz$ when agz is in the interval i_0, and $w\equiv agz-n\pi$ when agz is in the interval i_n $(n\geq 1)$. In (6.27), we separated the integrand into a part that is entirely nonsingular in the integration region, and a part that is singular but gives a finite value of integration since the Cauchy principal ($\mathcal{P}$) value has to be taken. From a formal point of view, we note that $\delta\tilde{\mathcal{L}}_0$ doesn't "feel" the poles of the integrand as depicted in Fig. 6.1, while $\delta\tilde{\mathcal{L}}_n$ $(n\geq 1)$ "feels" the pole $s=-\mathrm{i}n\pi/(ag)$ via the principal value part in (6.27) that is proportional to:

$$\begin{aligned}\mathrm{Re}\int_{-\pi/2}^{\pi/2}\mathrm{d}w\frac{\exp(-w/\tilde{a})}{(w+\mathrm{i}\epsilon')} &\equiv \mathcal{P}\int_{-\pi/2}^{\pi/2}\frac{\mathrm{d}w}{w}\exp(-w/\tilde{a})\\ &= -\mathrm{E}_1\left(\frac{\pi}{2\tilde{a}}\right)-\mathrm{Ei}\left(\frac{\pi}{2\tilde{a}}\right)\\ &= \left\{\begin{array}{ll}-2\left[x+x^3/(3!\,3)+x^5/(5!\,5)+\cdots\right] & \text{if } \tilde{a}\gg 1\\ -(e^x/x)\left[1+(1/x)+\cdots\right] & \text{if } \tilde{a}\ll 1\end{array}\right\}\end{aligned} \tag{6.29}$$

with $x=\pi/(2\tilde{a})$. We note that the dispersive part of the induced Lagrangian density as normalized here (6.25)–(6.28) depends only on two dimensionless parameters – on parameter $p\equiv b/a$ which characterizes in a Lorentz–invariant manner the ratio of the strengths of the (quasi-)electric and (quasi-)magnetic fields [cf. (6.14)–(6.15)], and on parameter $\tilde{a}\equiv(ga)/m^2$ which characterizes the combined strengths of the (quasi-)electric

field parameter a, the field–to–fermion coupling g, and the squared fermion mass m^2. In the perturbative weak–field limit, $\tilde{a}$ is small. In this case, when reintroducing $z \equiv w/(ag)$ into (6.26) we get:

$$\begin{aligned} \mathrm{Re}\delta\tilde{\mathcal{L}}_0 &= -\frac{1}{8\pi^2}\int_0^{\pi/(2ag)} \frac{\mathrm{d}z}{z} \times \exp(-zm^2) \times \\ &\quad \left[g^2 ab \cot(agz)\coth(bgz) + \frac{g^2}{3}(a^2-b^2) - \frac{1}{z^2}\right]. \end{aligned} \tag{6.30}$$

One can see that the real part of expression (6.24) is approximately reproduced, since formally $\pi/(2ag) \to \infty$. In this case, the conventional perturbative expansion of the dispersive Lagrangian density in powers of g^2 (i.e., inverse powers of x) can be performed (cf. [100], [102]):

$$\delta\tilde{\mathcal{L}}^{\mathrm{pert.}}(\tilde{a};p) = \left(c_1 1!\,\tilde{a}^2 + c_3 3!\,\tilde{a}^4 + c_5 5!\,\tilde{a}^6 + \cdots\right) , \tag{6.31}$$

where the expansion coefficients are:

$$\begin{aligned} c_1 &= \frac{1}{45}\left[(1-p^2)^2 + 7p^2\right] , \\ c_3 &= \frac{1}{945}\left[2(1-p^2)^3 + 13p^2(1-p^2)\right] , \\ c_5 &= \frac{1}{14175}\left[3(1-p^2)^4 + 22p^2(1-p^2)^2 + 19p^4\right] , \text{ etc.} \end{aligned} \tag{6.32}$$

In the case of pure magnetic field (p.m.f), the corresponding expressions are simpler:

$$\begin{aligned} \delta\tilde{\mathcal{L}}(\tilde{b})_{\tilde{a}=0} &\equiv \frac{8\pi^2\delta\mathcal{L}_{a=0}}{m^4\tilde{b}^2} \\ &= \int_0^\infty dz \exp\left(-\frac{z}{\tilde{b}}\right)\frac{(-1)}{z}\left[\frac{\coth(z)}{z} - \frac{1}{3} - \frac{1}{z^2}\right] , \end{aligned} \tag{6.33}$$

and the conventional perturbative expansion is:

$$\delta\tilde{\mathcal{L}}^{\mathrm{pert.}}(\tilde{b})_{\tilde{a}=0} = \left[\tilde{c}_1 1!\,\tilde{b}^2 + \tilde{c}_3 3!\,\tilde{b}^4 + \cdots\right] \tag{6.34}$$

with coefficients

$$\tilde{c}_1 = \frac{1}{45}, \quad \tilde{c}_3 = -\frac{2}{945}, \ldots .$$

Expression (6.31) can be derived alternatively by purely perturbative methods – the terms $\sim\tilde{a}^{2n}$ can be obtained by calculating the one–fermion–loop Feynman diagram with $2n$ photon external legs of zero momenta. It is a divergent asymptotic series and gives

the usual perturbative corrections to the Maxwell equations [128]. On the other hand, the formal small–$\tilde{a}$ expansion of $\mathrm{Re}\delta\tilde{\mathcal{L}}_0$ of (6.26) [or equivalently: (6.30)] reproduces the terms (6.31) and yields in addition the terms $\sim\tilde{a}\exp(-\mathrm{const.}/\tilde{a})$. The latter terms may in principle be dangerous for the interpretation of $\mathrm{Re}\delta\tilde{\mathcal{L}}_0$ of (6.26) as the perturbative part of the induced density, since they are nonanalytic and could thus signal physical nonperturbative effects. However, in the appendix H we demonstrate that these terms are only an artifact of the abruptness of the infrared (IR) proper–time cutoff $z \leq 1/\Lambda_{\mathrm{IR}}^2$ ($\Lambda_{\mathrm{IR}}^2 = (2/\pi)m^2\tilde{a} \sim m^2\tilde{a}$). [1] These terms are therefore not of a physical nonperturbative origin. In the appendix H we further show that $\mathrm{Re}\delta\tilde{\mathcal{L}}_0$ of (6.26) should be reinterpreted as the limit with an infinitesimally softened IR cutoff, the latter limit being numerically the same but having no nonanalytic terms in the small–$\tilde{a}$ expansion. That expansion is then identical to (6.31).

On the other hand, the densities $\mathrm{Re}\delta\tilde{\mathcal{L}}_n$ ($n \geq 1$) of (6.27) represent the nonperturbative part of the induced dispersive density (6.25), for two reasons:

- The integration over the proper–time z runs here in the vicinity (in fact, across) the n'th pole of the integrand of (6.24). The poles of the integrand are in the nonperturbative regions. We recall that these poles are also the source of the nonzero imaginary (absorptive) part of the density leading to the fermion–antifermion pair creation, a clearly nonperturbative phenomenon.

- The densities $\mathrm{Re}\delta\tilde{\mathcal{L}}_n$ ($n \geq 1$), independent of the pole structure of their integrands, become appreciable only in the strong–field (large–$\tilde{a}$) regime while in the weak–field (small–$\tilde{a}$) region they decrease faster than any power of $\tilde{a}$, i.e., they do not contribute to the perturbative series (6.31). Each of the two integrals in the curly brackets of (6.27) behaves as $\sim\tilde{a}\exp[\pi/(2\tilde{a})]$ when $\tilde{a} \to +0$, and thus the entire $\mathrm{Re}\delta\tilde{\mathcal{L}}_n$ behaves as $\sim\tilde{a}\exp[-(n-1/2)\pi/\tilde{a}]$ ($n \geq 1$) in this limit. [2]

Therefore, the nonperturbative effects contained in $\mathrm{Re}\delta\tilde{\mathcal{L}}_n$ ($n \geq 1$) are of two types, one type being characterized by the poles of the integrand, and the other type by what we

[1] The energy cutoff $\Lambda_{\mathrm{IR}} \sim m\sqrt{\tilde{a}}$ is low in the case when the perturbative effects dominate (i.e., at $\tilde{a} < 1$), but is higher when the nonperturbative effects are significant (at $\tilde{a} > 1$). The nonperturbative effects here reside in the infrared (IR) sector of (fermionic) momenta $q < \Lambda_{\mathrm{IR}}$, and the effective contributing size of this sector gets larger when $\tilde{a}$ grows.

[2] If we do not take the Cauchy principal value in (6.27), but some other prescription (which in the case at hand would be wrong), $\mathrm{Re}\delta\tilde{\mathcal{L}}_n$ would behave as $\sim\exp[-n\pi/\tilde{a}]$.

may call strong–field effects. From the above discussion, it further follows that we have some freedom in choosing the IR proper–time cutoff: $z \leq 1/\Lambda^2_{\rm IR}$ is such that $\Lambda^2_{\rm IR} \sim m^2\tilde{a}$ and that all the possible poles must lie at z's above the cutoff $1/\Lambda^2_{\rm IR}$. We took $\Lambda^2_{\rm IR} = \kappa m^2\tilde{a}$ with $\kappa = 2/\pi$, but any κ satisfying $1/\pi < \kappa \sim 1$ would be acceptable as well.

From a somewhat different perspective, we can imagine transforming a truncated perturbation expansion for ${\rm Re}\delta\tilde{\mathcal{L}}^{\rm pert.}/\tilde{a}$ of (6.31) (with several terms) via the Borel–Padé approximation. The resulting integrand approximately reproduces the integrand of (6.24), including the poles structure. Thus the integration over the n'th pole, contained in ${\rm Re}\delta\tilde{\mathcal{L}}_n$ of (6.27), can be interpreted as the n'th renormalon in the density, i.e., a nonperturbative quantity. We will return to this point in sec. 6.4.4.

Thus, the densities (6.26) and (6.27) result in the fermion–induced perturbative and nonperturbative contributions, respectively, to the Maxwell equations. The fields were taken, strictly speaking, to be homogeneous in space and time. In practical terms, this means that they are not allowed to change significantly on the distance and time scales of the Compton wavelength of the fermion $1/m$. For electro–magnetic fields, m is the electron mass, and $1/m$ is about $4 \cdot 10^{-13}$ m, and $1.3 \cdot 10^{-21}$ s.

An indication of the relative size of the perturbative and nonperturbative fermion–induced corrections to the Maxwell equations can be obtained by comparing the corresponding contributions to the induced Lagrangian density. This is done in Figs. 6.2 and 6.3. Figures 6.2 (a) and 6.2 (b) show the dimensionless perturbative (6.26) and nonperturbative (6.27) induced Lagrangian densities, respectively, as functions of the (quasi-)electric field parameter $\tilde{a}$ (6.28), at four different fixed values $p \equiv \tilde{b}/\tilde{a}$ of the magnetic–to–electric field ratio. The case of the pure (quasi-)magnetic field (p.m.f.) is also included in the Figures, as function of $\tilde{b}$. For the p.m.f. case, we normalized the Lagrangian density in analogy with (6.28), i.e., $\delta\tilde{\mathcal{L}}$ is obtained in that case by dividing $\delta\mathcal{L}$ by $m^4\tilde{b}^2/(8\pi^2)$. The separation between the perturbative and the nonperturbative part was performed in the p.m.f. case analogously, i.e., the proper–time $z < \pi/(2bg)$ contributions were defined to be perturbative, and those from $z > \pi/(2bg)$ nonperturbative. We point out, however, that in the latter case the nonperturbative contributions do not involve the renormalon–type ("pole–type") effects, but only strong–field effects (cf. previous discussion). In Fig. 6.3, the corresponding ratios of the nonperturbative and perturbative induced densities are presented. [3] When moving beyond the perturbative region (i.e.,

[3]The total induced dispersive Lagrangian densities, and values of the truncated perturbation series

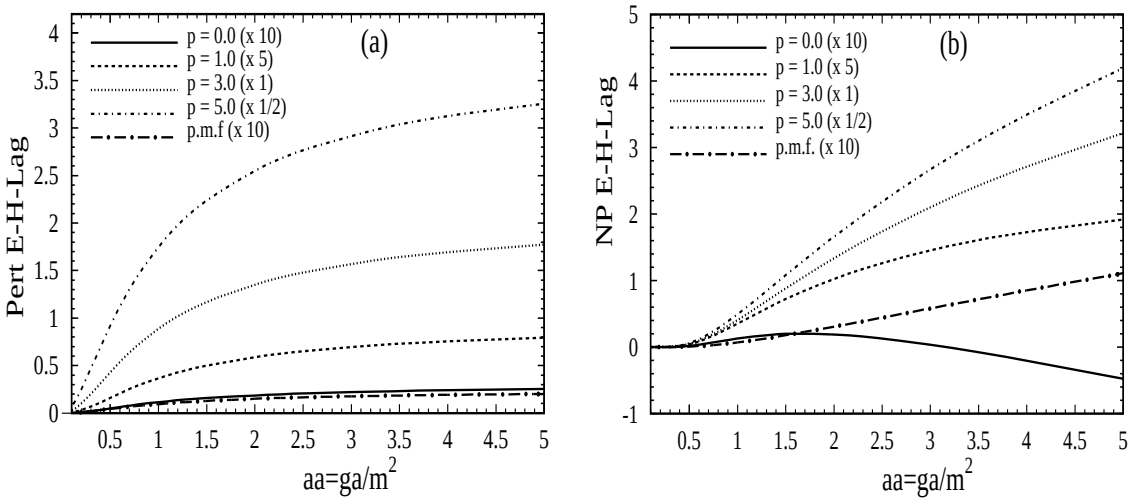

Figure 6.2: (a) Perturbative and (b) nonperturbative induced dispersive (Euler–Heisenberg) Lagrangian densities [cf. (6.26) and (6.27)] as functions of the (quasi-)electric field parameter $\tilde{a}$ (6.28), at various fixed values of the magnetic–to–electric field ratio $p = \tilde{b}/\tilde{a}$ (6.28). The actual values of the curves for $p \approx 0$, $p = 1.0$ and $p = 5.0$ have been multiplied here by factors 10, 5 and $1/2$, respectively, for better visibility. Included is also the case of the pure (quasi-)magnetic field (p.m.f.), for which the x-axis represents $\tilde{b} = gb/m^2$.

when $\tilde{a} \ll 1$), we see from these Figures that the nonperturbative parts in general become relatively significant and often even dominant.

Once we come into the nonperturbative regime ($\tilde{a} \gtrsim 1$), however, we must keep in mind that the pair creation, originating from the large absorptive part, will become so strong as to render the solutions of the corrected Maxwell equations unstable. We will quantify this fact in the next section in the case of the induced energy density in QED.

In Figs. 6.2 (a), (b), the densities were normalized according to (6.28), so that the tree–level reference values for the densities are:

$$\tilde{\mathcal{L}}^{(0)} \equiv \mathcal{L}^{(0)} / \left(\frac{m^4 \tilde{a}^2}{8\pi^2} \right) = \frac{4\pi^2}{g^2}(1 - p^2) \ . \tag{6.35}$$

Therefore, increasing only the coupling parameter g, while leaving the (quasi-)electric field a unchanged, results in correspondingly larger relative corrections originating from the induced parts, both nonperturbative and perturbative. In the special case of QED, on

(6.31) (including $\sim \tilde{a}^8$), are included in Figs. 6.6 in section 6.4.2.

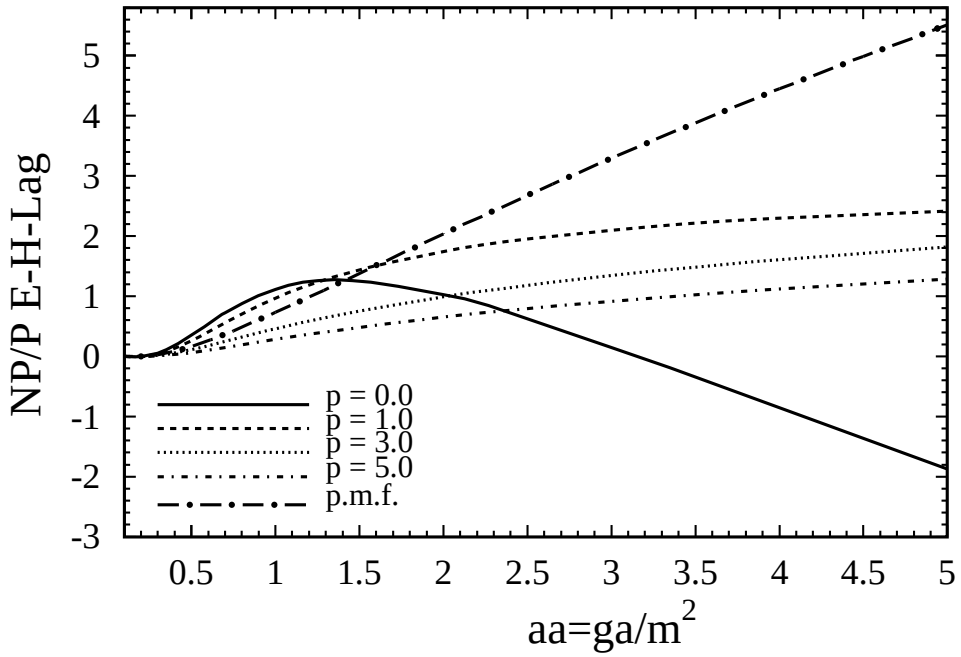

Figure 6.3: Ratios of the nonperturbative and the perturbative induced dispersive Lagrangian densities for the cases depicted in Figs. 6.2. For the p.m.f. case, the x-axis represents $\tilde{b}=gb/m^2$.

the other hand, $g=e_0$ is small ($\alpha=e_0^2/(4\pi)\approx 1/137$), and the overall induced Lagrangian density accounts usually for less than 0.5 permille of the total Lagrangian density when $\tilde{a}\leq 1$ (see the next section on related points).

6.3 Induced Energy Density

In this section, we discuss the induced energy densities. Energy density is in principle a measurable quantity. But, it is not Lorentz–invariant. If the (quasi-)electric and (quasi-) magnetic fields are mutually parallel, the various induced energy densities can be obtained directly from the corresponding induced Lagrangian densities:

$$\delta\mathcal{U}_k \;=\; a\frac{\partial \mathrm{Re}\delta\mathcal{L}_k}{\partial a}\bigg|_b - \mathrm{Re}\delta\mathcal{L}_k$$

$$\Rightarrow \quad \delta\tilde{\mathcal{U}}_k \;=\; \tilde{a}\frac{\partial \mathrm{Re}\delta\tilde{\mathcal{L}}_k}{\partial\tilde{a}}\bigg|_{\tilde{b}} + \mathrm{Re}\delta\tilde{\mathcal{L}}_k \quad (k=0,1,2,\ldots)\ , \tag{6.36}$$

where we denoted, in analogy with (6.28)

$$\delta\tilde{\mathcal{U}}_{(k)} \equiv \delta\mathcal{U}_{(k)}/\left(\frac{m^4\tilde{a}^2}{8\pi^2}\right)\ . \tag{6.37}$$

With the restriction to parallel fields $\vec{\mathcal{E}} \parallel \vec{\mathcal{B}}$ (i.e, $|\vec{\mathcal{E}}|=a$ and $|\vec{\mathcal{B}}|=b$) we do not lose the generality, since for any configuration of $\vec{\mathcal{E}}$ and $\vec{\mathcal{B}}$, there always exists a Lorentz boost, perpendicular to the plane of the fields, so that in the boosted frame the two fields are parallel. The corresponding perturbative and nonperturbative parts of the energy densities in such frames are:

$$\begin{aligned}
\mathrm{Re}\delta\tilde{\mathcal{U}}_0 \;=\; & -\int_0^{\pi/2}\frac{\mathrm{d}w}{w}\exp\left(-\frac{w}{\tilde{a}}\right)\Bigg\{\left(\frac{w}{\tilde{a}}-1\right)\left[p\cot(w)\coth(pw)+\frac{1}{3}(1-p^2)-\frac{1}{w^2}\right] \\
& +\left[p\cot(w)\coth(pw)+p^2\frac{w\cot(w)}{\sinh^2(pw)}+\frac{2}{3}-\frac{2}{w^2}\right]\Bigg\}\ ,\ (n=0)
\end{aligned} \tag{6.38}$$

$$\begin{aligned}
\mathrm{Re}\delta\tilde{\mathcal{U}}_n \;=\; & -\exp\left(-\frac{n\pi}{\tilde{a}}\right)\Bigg\{\int_{-\pi/2}^{\pi/2}\mathrm{d}w\exp\left(-\frac{w}{\tilde{a}}\right)\left[\frac{(w+n\pi)}{\tilde{a}}-1\right]\times \\
& \left[\frac{p\cot(w)\coth(p(w+n\pi))}{(w+n\pi)}-\frac{p}{w}\frac{\coth(pn\pi)}{n\pi}+\frac{(1-p^2)}{3(w+n\pi)}-\frac{1}{(w+n\pi)^3}\right] \\
& +\int_{-\pi/2}^{\pi/2}dw\exp\left(-\frac{w}{\tilde{a}}\right)\Bigg[p\cot(w)\left(\frac{\coth(p(w+n\pi))}{(w+n\pi)}+\frac{p}{\sinh^2(p(w+n\pi))}\right) \\
& -\frac{p}{w}\left(\frac{\coth(pn\pi)}{n\pi}+\frac{p}{\sinh^2(pn\pi)}\right)+\frac{2}{3}\frac{1}{(w+n\pi)}-\frac{2}{(w+n\pi)^3}\Bigg] \\
& +\left[\frac{p}{\tilde{a}}\coth(pn\pi)+\frac{p^2}{\sinh^2(pn\pi)}\right]\left[-\mathrm{E}_1\left(\frac{\pi}{2\tilde{a}}\right)-\mathrm{Ei}\left(\frac{\pi}{2\tilde{a}}\right)\right] \\
& +\frac{2p}{n\pi}\coth(pn\pi)\sinh\left(\frac{\pi}{2\tilde{a}}\right)\Bigg\}\ ,\quad (n\geq 1)\ .
\end{aligned} \tag{6.39}$$

The tree–level density in the normalization convention used [cf. (6.28)] is:

$$\tilde{\mathcal{U}}^{(0)} \equiv \mathcal{U}^{(0)}/\left(\frac{m^4\tilde{a}^2}{8\pi^2}\right) = \frac{4\pi^2}{g^2}(1+p^2)\ . \tag{6.40}$$

The perturbative power expansion of the induced energy density $\delta\tilde{\mathcal{U}}$ is:

$$\delta\tilde{\mathcal{U}}^{\mathrm{pert.}}(\tilde{a}:p) = \left(d_1 1!\,\tilde{a}^2 + d_3 3!\,\tilde{a}^4 + d_5 5!\,\tilde{a}^6 + \cdots\right)\ , \tag{6.41}$$

where the expansion coefficients are:

$$\begin{aligned} d_1 &= \frac{1}{45}\left[3+5p^2-p^4\right] \ , \\ d_3 &= \frac{1}{945}\left[10+21p^2-7p^4+2p^6\right] \ , \\ d_5 &= \frac{1}{14175}\left[21+50p^2-21p^4+10p^6-3p^8\right] \ , \text{ etc.} \end{aligned} \tag{6.42}$$

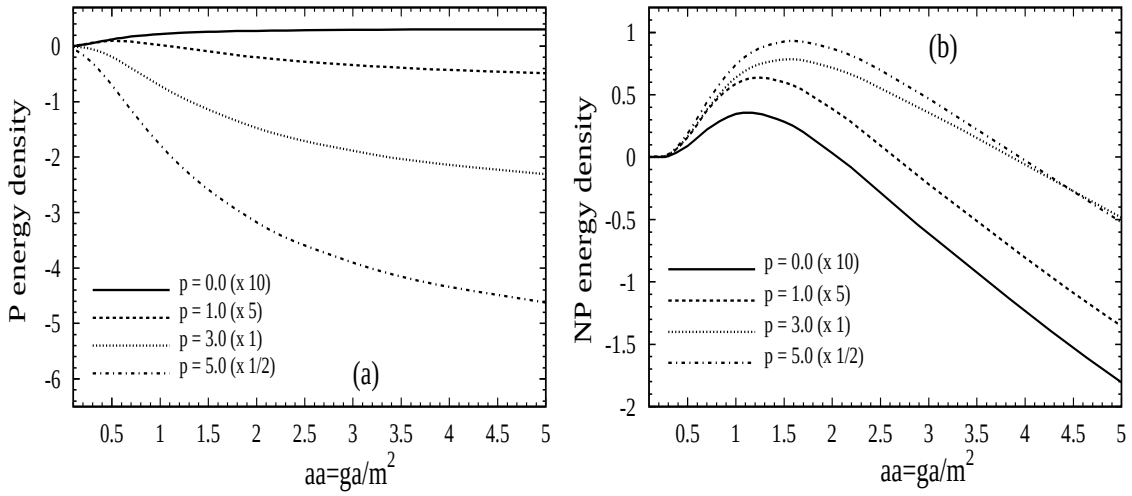

Figure 6.4: (a) Perturbative and (b) nonperturbative induced energy densities [cf. (6.38) and (6.39)] as functions of $\tilde{a}$ at various fixed values of $p=\tilde{b}/\tilde{a}$ (6.28). The actual values of the curves have been multiplied, for better visibility, by the denoted factors, just as in Figs. 6.2.

The results for the induced perturbative (6.38) and nonperturbative parts (6.39), and their ratios, are presented in Figs. 6.4 (a)–(b) and 6.5, respectively, in analogy with Figs. 6.2 (a)–(b) and 6.3. The case of the pure (quasi-)magnetic field is not included in Figs. 6.4–6.5, because in this case $\delta\tilde{\mathcal{U}}=-\delta\tilde{\mathcal{L}}$ and thus the relevant information is already contained in Figs. 6.2–6.3. The behavior of the induced energy densities is, in broad qualitative terms, similar to that of the induced Lagrangian densities. [4]

In the special case of QED, similarly as for the Lagrangian densities in the previous section, the total induced energy densities account for a very small part of the total energy

[4]The total induced energy densities, and values of the truncated perturbation series (6.41) that include terms $\sim\tilde{a}^8$, are included in Figs. 6.7 in section 6.4.3.

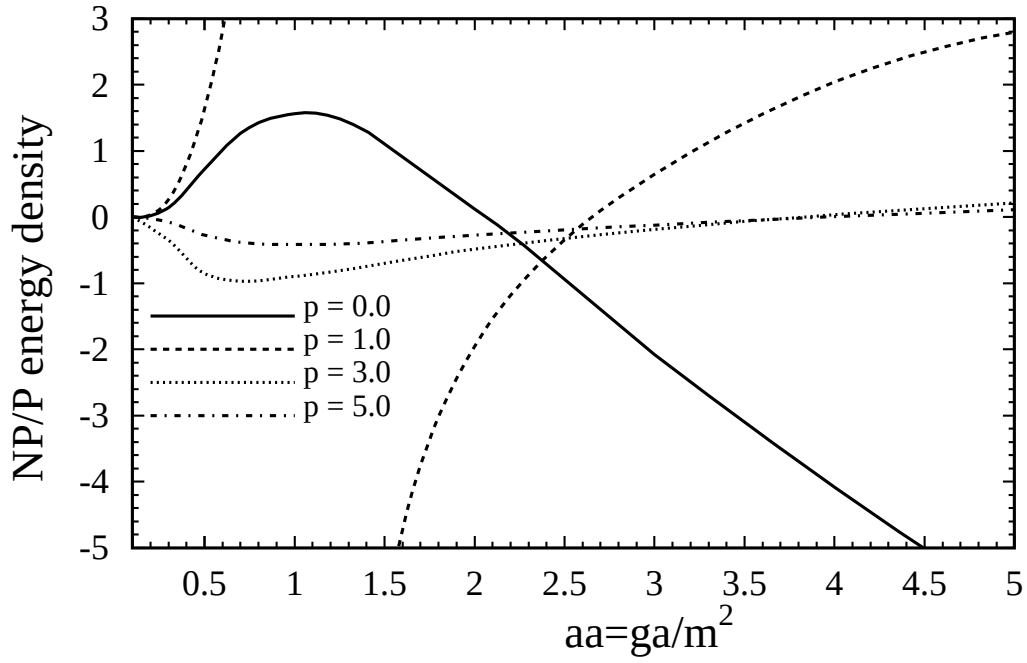

Figure 6.5: Ratios of the nonperturbative and the perturbative induced energy densities for the cases depicted in Figs. 6.4. The ratio for $p=1$ varies strongly for $\tilde{a}=0.5$–1.5 because the perturbative induced density has a zero at $\tilde{a}\approx 1.1$.

density (0.2–0.3 permille when $\tilde{a}\approx 1$) and can become significant only when the field becomes exceedingly large ($\tilde{a}\gtrsim 10^2$). The same is true also for the dielectric permeability tensor ε_{ij}: In the direction of the fields, we have $\delta\varepsilon_\parallel \equiv \varepsilon_\parallel - 1 = a\partial(\mathrm{Re}\delta\mathcal{L})/\partial a|_b$, i.e., by (6.36)–(6.37) we have $\delta\varepsilon_\parallel = (\delta\tilde{\mathcal{U}} + \mathrm{Re}\delta\tilde{\mathcal{L}})\alpha/(2\pi)$, which is about 10^{-3} for $\tilde{a}\approx 1$ and $p=1$. Therefore, the effective coupling parameter along the field direction $\alpha_\parallel = \alpha/\varepsilon_\parallel$ changes by about one permille, while $\alpha_\perp = \alpha/\varepsilon_\perp$ remains unchanged since $\varepsilon_\perp = 1$. Therefore, in QED, any quantity which can be expanded in powers of the coupling parameter alone (without fields) remains a perturbative quantity. QED then remains a perturbative theory despite such strong fields – cf. also Ref. [129] on that point.

The energy density is not stable in time when $\tilde{a}\neq 0$, due to the energy losses to pair creation of fermions of mass m. It decreases by about 50 percent in the time $t_{1/2}$:

$$t_{1/2} \approx \frac{\pi^2}{8\alpha} \exp\left(+\frac{\pi}{\tilde{a}}\right) \left[\frac{(1+p^2)}{p\pi\coth(p\pi)}\right] \frac{1}{m} \,, \tag{6.43}$$

where $\alpha \equiv g^2/(4\pi)$. The factor in the square brackets, appearing due to the presence of the (quasi-)magnetic field, is usually not essential in the estimates since it is $\sim$1 for $p \leq 5$. In the case of QED and with $p=0$, $t_{1/2}$ is about $0.9 \cdot 10^5 m_e^{-1}$, $0.4 \cdot 10^4 m_e^{-1}$ and $0.3 \cdot 10^3 m_e^{-1}$ for $\tilde{a} = 0.5$, 1, and 5, respectively. Here, $m_e^{-1} \approx 1.3 \cdot 10^{-21}$ s is the electron Compton time.

6.4 Quasianalytic Continuation into the Nonperturbative Sector

In this section, we use the discussed induced densities as an example on which to test and get some insights into methods of approximate analytic (i.e., quasianalytic) continuation. In various physical contexts, such methods allow one to extract all or part of the information on the nonperturbative sector from the knowledge of the perturbative sector alone. We will use the method of Borel–Padé transformation, or a modification thereof.

6.4.1 Definitions

Before we discuss the efficiency of methods of quasianalytic continuation into the nonperturbative sector we give some useful definitions for this section.

- Quasianalytic continuation:
  If we know, for a function $f(a)$, which is analytic at $a = 0$, the full power expansion around $a = 0$:
  $$f(a) \sim e_1 a + e_2 a^2 + e_3 a^3 + \ldots \,, \tag{6.44}$$
  then usually this infinite series is convergent in the complex plain in a disc of a finite radius $r_0 (|a| < r_0)$ (in some cases we even have $r_0 = 0$, e.g. in QCD). But then, if $r_0 \neq 0$ (and often even when $r_0 = 0$), the function $f(a)$ can be determined also for $|a| > r_0$ by means of the analytic continuation. Physically, this represents a continuation from the weak coupling $|a| < r_0$ to the strong coupling $|a| > r_0$, based only on our initial knowledge of $f(a)$ in the weak coupling regime, i.e., the knowledge of the infinite power series of $f(a)$. However, in physical problems we often do not know the full power series of $f(a)$, but only a few terms (truncated power series (TPS)). Thus our knowledge of $f(a)$ in the weak coupling regime is in practice not exact (full). Therefore, any approximation that gives us the values

of $f(a)$ in the strong coupling regime, on the basis of the known TPS, is called quasianalytic continuation, in contrast to the aforementioned analytic continuation.

- Borel transformation:
  Suppose we have a function $f(a)$. Then the Borel transformation $\mathrm{BT}f(w)$ of $f(a)$ is defined via the integral relation:

$$f(a) = \int_0^\infty \mathrm{d}w \, \exp(-w/a) \, \mathrm{BT}f(w). \tag{6.45}$$

  This integral is called Borel integral, or often also Borel-Laplace integral. The above relation $\mathrm{BT}f(w) \to f(a)$ is called inverse Borel transformation. The Borel transformation is $f(a) \to \mathrm{BT}f(w)$. The power expansions of $f(a)$ (in powers of a) and of $\mathrm{BT}f(a)$ (in powers of w) are closely related, as can be checked via the above integral relation:

$$\begin{aligned} f(a) &\sim e_1 a + e_2 a^2 + e_3 a^3 + \ldots . \\ \mathrm{BT}f(w) &= e_1 + e_2 \frac{w}{1!} + e_3 \frac{w^2}{2!} + e_4 \frac{w^3}{3!} + \ldots . \end{aligned} \tag{6.46}$$

- Padé-approximant:
  If we have an input perturbative series given by: $f(x) = \sum_{n=0}^\infty c_n x^n$, a Padé-approximant (PA) can be constructed by writing a ratio of two polynomials so that their Taylor expansion up to and including order $N + M$ is identical to the original series:

$$\mathrm{P}_{[N/M]}(x) = \frac{a_0 + a_1 x + \ldots + a_N x^N}{1 + b_1 x + \ldots + b_M x^M}, \quad \mathrm{P}_{[N/M]}(x) = f(x) + O(x^{N+M+1}). \tag{6.47}$$

- Borel-Padé transformation:
  If we know only a TPS for $f(a)$, we can either construct a PA of that TPS of $f(a) \to \mathrm{PA}_f(a)$, or we can take first the corresponding TPS of $\mathrm{BT}f(w)$, construct a PA for this latter TPS $[\mathrm{BT}f(w) \to \mathrm{PA}_{\mathrm{BT}f}(w)]$ and then pretend that this PA is $\mathrm{BT}f(w)$ (it is only approximately so) and apply to it the Borel integration:

$$\mathrm{BP}f(aw) = \int_0^\infty \mathrm{d}w \, \exp(-w/a) \, \mathrm{PA}_{\mathrm{BT}f}(aw). \tag{6.48}$$

  This we can call a Borel-Padé approximant of $f(a)$, since the PA was applied to its Borel transformation $\mathrm{BT}f(w)$, not to $f(a)$ itself. The above integration can be called loosely Borel-Padé transformation.

- Modified Borel Transformation:
  We defined the modified Borel transformation of $f(a)$ as $\mathrm{MBT}f(w)$ such that the following integral transformation connects them

$$f(a) = 1/a \int_0^\infty \mathrm{d}w \, \exp(-w/a) \, \mathrm{MBT}f(w). \tag{6.49}$$

  This transformation is almost like the usual above-mentioned Borel transformation, except that we have now the factor $1/a$ in front of the Borel integral.

- Meromorphic function:
  Meromorphic function is a function $f(a)$ which is analytic in the entire complex plane, expect for a discrete number of points (this discrete number can be infinite, but each point of singularity is surrounded by an area of analyticity).

6.4.2 Application of Borel-Padé Method for the Euler-Heisenberg Lagrangian Density

One may ask whether the perturbation expansions (6.31) and (6.41) allow us to obtain the full, including the nonperturbative, information about the corresponding densities. The answer for the Lagrangian density is yes, but under the condition that we take in the corresponding Borel–Padé approximants the Cauchy principal values when integrating over the positive poles of the Padé integrand in the inverse Borel transformation. This is reflected in the terms $\mathrm{i}\epsilon$ in the denominators of the integrands of (6.24) and/or (6.27). More specifically, we first use the Borel–transform (BT) of the perturbation series (6.31):

$$\mathrm{BT}\left[\delta\tilde{\mathcal{L}}^{\mathrm{pert.}}(\tilde{a};p)\right] = c_1(p)\tilde{a} + c_3(p)\tilde{a}^3 + c_5(p)\tilde{a}^5 + \cdots \, , \tag{6.50}$$

then construct an $[N/M]_{\mathrm{B}}(\tilde{a};p)$ Padé approximant to (6.50), [5] and then apply the inverse Borel transformation:

$$\mathrm{BP}^{[N/M]}\left[\delta\tilde{\mathcal{L}}^{\mathrm{pert.}}\right](\tilde{a};p) = \int_0^\infty dw \exp\left(-\frac{w}{\tilde{a}}\right)[N/M]_{\mathrm{B}}(w;p) \, . \tag{6.51}$$

On the other hand, the real part of the actual density (6.24) can also be written as a Borel–type integral, when introducing $w \equiv agz$ and $\epsilon' \equiv ag\epsilon$ in (6.24) and normalizing the

[5] $[N/M](\tilde{a})$ Padé approximant to (6.50) is defined by two properties: 1. it is a ratio of two polynomials in $\tilde{a}$, the numerator polynomial having the highest power $\tilde{a}^N$ and the denominator $\tilde{a}^M$; 2. when expanded in powers of $\tilde{a}$, it reproduces the coefficients at the terms $\tilde{a}^n$ in (6.50) for $n \leq N+M$; it is based solely on the knowledge of these latter coefficients c_n $(n \leq N+M)$.

density according to (6.28)

$$\mathrm{Re}\delta\tilde{\mathcal{L}}(\tilde{a};p) = \mathrm{Re}\int_0^\infty dw \exp\left(-\frac{w}{\tilde{a}}\right)\frac{(-1)}{w}\times \left[\frac{p\cos(w)}{\sin(w+\mathrm{i}\epsilon')}\coth(pw)+\frac{1}{3}(1-p^2)-\frac{1}{w^2}\right] . \quad (6.52)$$

The expansion of the integrand of (6.52), excluding the exponential, in powers of w is identical with the Borel transform (6.50) with $\tilde{a}\mapsto w$, as it should be. Comparing (6.51) with the exact result (6.52), we see that the Borel–Padé method (6.51) will be efficient in (quasianalytic continuation if Padé approximants $[N/M]_{\mathrm{B}}(w)$ approach the integrand of (6.52) in an increasingly wide integration interval of w when the Padé order indices N and M ($\approx N$) increase. This in fact happens, since the integrand in (6.52) is a meromorphic function in the complex plane whose pole structure on the positive axis is especially simple – there are only single (not multiple) poles, located at $w=\pi,2\pi,3\pi,\ldots$. Padé approximants to power expansions of such functions are known to approximate such functions increasingly better when the Padé order indices $N\approx M$ increase [130]. Near the poles $w\approx n\pi$ the integrand behaves as $\sim(w-n\pi+\mathrm{i}\epsilon')^{-1}$. Hence, for obtaining the real (dispersive) part of the density, the Borel integration over the poles has to be taken with the Cauchy principal value (CPV) prescription – not just in the exact expression (6.52), but also in the approximate expression (6.51). Thus, the Borel integration in (6.51) over the n'th pole, i.e., the n'th renormalon contribution, has in the case at hand no renormalon ambiguity. As the Padé order indices $N\approx M$ are increased, we thus systematically approach the exact $\mathrm{Re}\delta\tilde{\mathcal{L}}$ via the CPV of (6.51). This means that in the case at hand [strong (quasi–)Abelian fields with fermionic fluctuations included], the full induced Lagrangian density can be obtained on the basis of the knowledge of perturbation expansion (6.31) for weak fields and the CPV prescription. The more terms in (6.31) [and thus in (6.50)] we know, the higher Padé order indices $N\approx M$ we can have, and hence the closer to the full Lagrangian density we can come via (6.51).

On the basis of the knowledge of the first four nonzero perturbation terms in (6.31) and correspondingly in (6.50), we can construct the following Padé approximants of the perturbative Borel transform (6.50): $[1/2]_{\mathrm{B}},[1/4]_{\mathrm{B}},[3/4]_{\mathrm{B}}$. Then we can calculate the corresponding Borel-Padé transforms via (6.51) with the CPV prescription. Using the same method we evaluate the case of pure magnetic fields. The corresponding results of the approximants for the full induced density $\mathrm{Re}\delta\tilde{\mathcal{L}}$ are presented in Fig. 6.6, together with the exact numerical values calculated by (6.52) in section 6.2 . The curves are

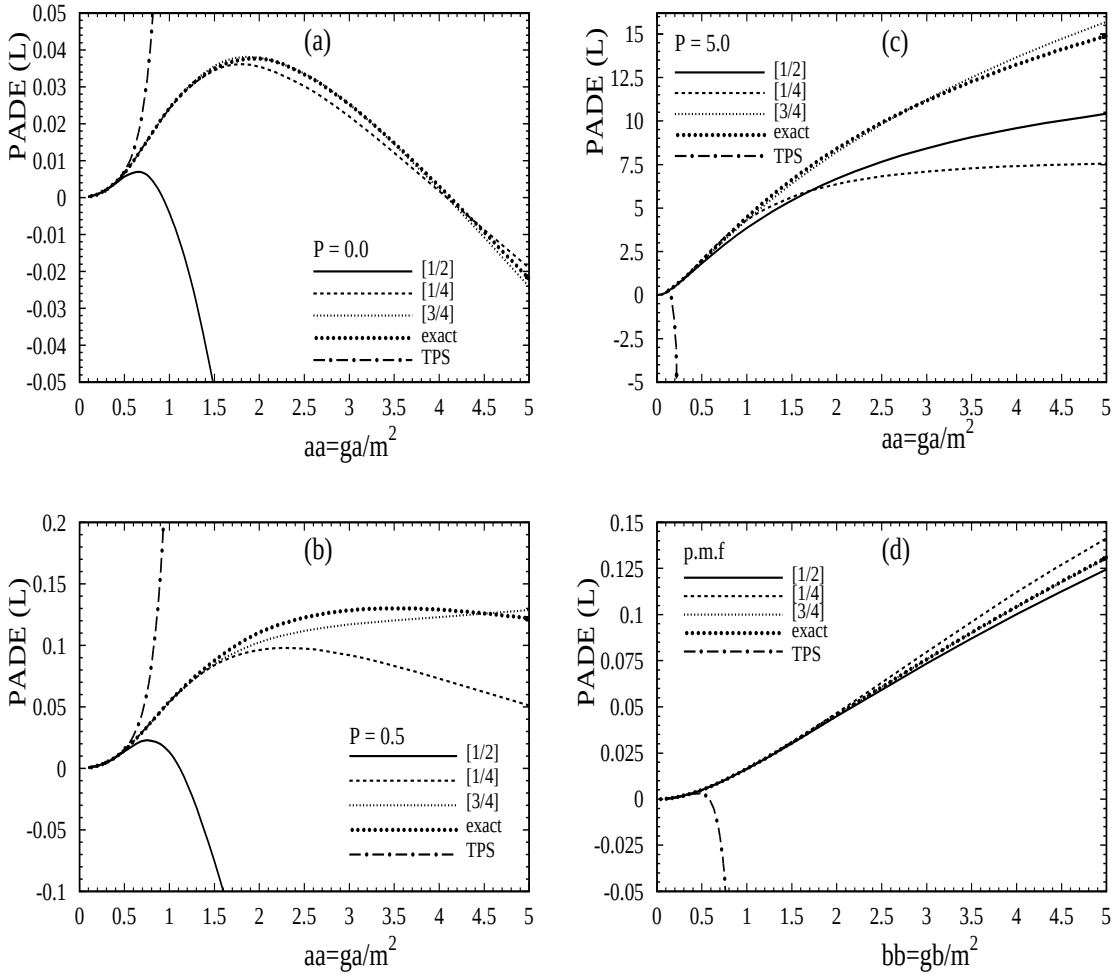

Figure 6.6: Borel–Padé approximants (BP's) to the induced dispersive Lagrangian density (6.28) as functions of $\tilde{a}$, for various values of $p = \tilde{b}/\tilde{a}$: (a) $p = 0$; (b) $p = 0.5$; (c) $p = 5.0$; (d) pure magnetic field ($\tilde{a} = 0$). Depicted are those BP's (6.51) which are based on the Padé approximants $[1/2]$, $[1/4]$ and $[3/4]$ of the Borel–transform (6.50). The numerically exact curves [sum of curves of Figs. 6.2 (a) and (b)] are also included and they virtually agree with the $[3/4]$ BP results. Included are also the the results of the truncated perturbative series which include terms $\sim\tilde{a}^8$ [in (d): $\sim\tilde{b}^8$].

given as functions of the (quasi-)electric strength parameter $\tilde{a}$ for four fixed values of the magnetic–to–electric field ratio p, and Fig. 6.6 (d) is for the case of the pure (quasi-)magnetic field ($\tilde{a}=0$). We see that the highest order ([3/4]) Borel–Padé results agree well with the exact results over the entire depicted region of $\tilde{a}$. When the Padé order indices N and M ($\sim N$) increase, the region of agreement includes increasingly large values of $\tilde{a}$. For comparison, we also included the results of the truncated perturbation series (TPS) made up of the first four nonzero terms of (6.31) and (6.34), i.e., those perturbation terms which the presented Borel–Padé transforms are based on and plot in Fig. 6.6 (d) for the corresponding p.m.f. case.

6.4.3 Application of Modified Borel-Padé Method for the Energy Density

If we apply the very same procedure in the case of the energy density Borel transforming the series $\delta\tilde{\mathcal{U}}^{\text{pert.}}/\tilde{a}$ of (6.41), constructing Padé approximants, and carrying out the inverse Borel transformation by using the CPV prescription – the results are disappointing. It turns out that increasing the Padé order indices N and M ($\sim N$) does not generally result in a better precision. For example, for $p \lessapprox 0.5$ and $\tilde{a} \gtrapprox 0.5$, the Borel–Padé transforms of the order [3/4] and [3/6] give significantly worse results than those of the lower order [1/4]. The reason for this erratic behavior of the Borel–Padé approximants in this case lies in the more complicated pole structure of the Borel–Padé transforms. This can be seen if we rewrite $\delta\tilde{\mathcal{U}}$ in the Borel–integral form analogous to (6.52), obtained from (6.52) by applying relation (6.36):

$$\begin{aligned} \text{Re}\delta\tilde{\mathcal{U}} &= \text{Re}\int_0^\infty \text{d}w \exp\left(-\frac{w}{\tilde{a}}\right)\frac{(-1)}{w} \\ &\quad \left[-\frac{pw}{\sin^2(w+\text{i}\epsilon')}\coth(pw)+\frac{1}{3}(1+p^2)+\frac{1}{w^2}\right] . \end{aligned} \tag{6.53}$$

The expansion in powers of w of the integrand in (6.53), excluding the exponential, gives of course the exact Borel transform of the perturbation series (6.41) divided by $\tilde{a}$ (and replacing $\tilde{a}\mapsto w$):

$$\begin{aligned} \text{BT}\left[\frac{\delta\tilde{\mathcal{U}}^{\text{pert.}}(w;p)}{w}\right] &= -\frac{1}{w}\left[-\frac{pw}{\sin^2(w+\text{i}\epsilon')}\coth(pw)+\frac{1}{3}(1-p^2)+\frac{1}{w^2}\right] \\ &= d_1(p)w + d_3(p)w^3 + d_5(p)w^5 + \cdots . \end{aligned} \tag{6.54}$$

However, we now see that this integrand has a double pole structure on the positive w axis, the double poles located at $w = \pi, 2\pi, 3\pi, \cdots$. The Padé approximants to the power series (6.54) have great trouble simulating this double pole structure adequately. When they do it by creating one single or two nearby real poles, say near $w = \pi$, then it turns out that the inverse Borel transformation via the CPV prescription often gives good results. However, when the Padé approximants try to simulate the double pole near $w = \pi$ by creating two mutually complex–conjugate poles $a \pm \mathrm{i}b$ ($a \approx \pi$, $|b| \ll \pi$), the inverse Borel transformation gives very unsatisfactory results. This occurs, for example, in Padé approximants $[3/4](w;p)$ and $[3/6](w;p)$ for $p \leq 0.5$. Heuristically we can understand that such a simulation is bad, because the structure of the integrand in (6.53) suggests that a double pole at $a - \mathrm{i}b$ alone, just below the real axis, would do a better job, but it is not allowed in the Padé approximants. The latter is true because the perturbation expansion (6.54) is explicitly real for real w's, and this property is hence shared also by the Padé approximants, enforcing for each complex pole another pole which is complex–conjugate.

To overcome this problem, the idea is to modify the Borel transformation of the perturbation series (6.41) in such a way that the resulting transformed series is represented by a (meromorphic) function without any double poles on the real positive axis, in contrast to the Borel transformed series (6.54). This, in fact, can be implemented in the easiest way by using the following modification of the Borel transformation (MB):

$$\begin{aligned} \frac{\partial \mathrm{MB}\left[\delta\tilde{\mathcal{U}}^{\mathrm{pert.}}\right](w;p)}{\partial w} &= \mathrm{BT}\left[\frac{\delta\tilde{\mathcal{U}}^{\mathrm{pert.}}(w;p)}{w}\right] \\ &= d_1(p)w + d_3(p)w^3 + d_5(p)w^5 + \cdots \\ \Rightarrow \quad \mathrm{MB}\left[\delta\tilde{\mathcal{U}}^{\mathrm{pert.}}\right](w;p) &= d_1(p)\frac{w^2}{2} + d_3(p)\frac{w^4}{4} + d_5(p)\frac{w^6}{6} + \cdots . \end{aligned} \tag{6.55}$$

This trick changes every double pole in the B into the corresponding single pole in the MB. Then we apply Padé approximants $[N/M]_{\mathrm{MB}}(w)$ to the MB series (6.55), and carry out the corresponding inverse modified Borel transformation:

$$\mathrm{MBP}^{[\mathrm{N/M}]}\left[\delta\tilde{\mathcal{U}}^{\mathrm{pert.}}\right](\tilde{a};p) = \frac{1}{\tilde{a}}\int_0^\infty dw \exp\left(-\frac{w}{\tilde{a}}\right)[N/M]_{\mathrm{MB}}(w;p) \tag{6.56}$$

with the CPV prescription when integrating over the single poles. This CPV prescription originates again from the $\mathrm{i}\epsilon'$ terms in the double pole structure $(w - n\pi + \mathrm{i}\epsilon')^{-2}$ of the Borel transform (B) integrand of (6.53) that is now changed to the single pole structure $(w - n\pi + \mathrm{i}\epsilon')^{-1}$ in the MB of (6.55) whose Padé approximants $[N/M]_{\mathrm{MB}}(w;p)$ appear in (6.56).

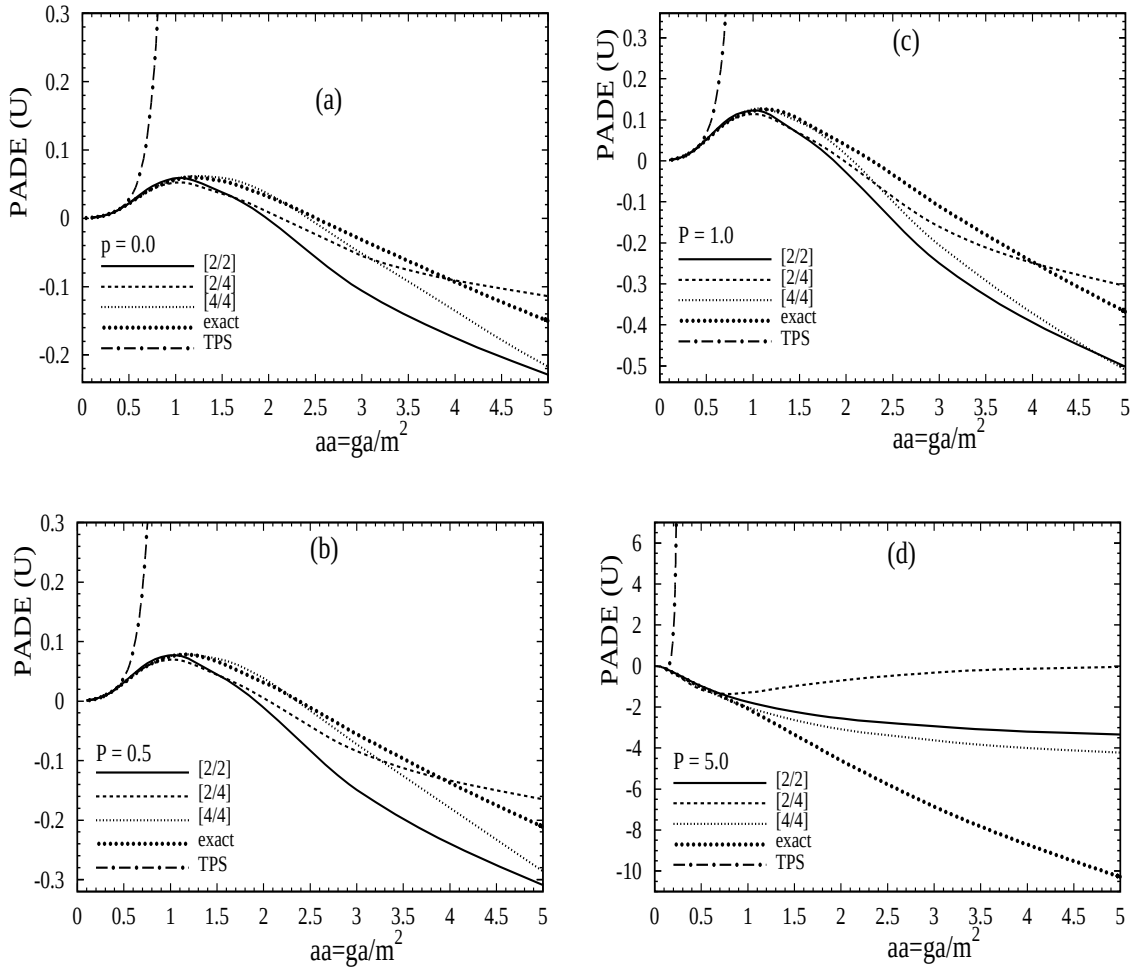

Figure 6.7: Modified Borel–Padé approximants [MBP's – cf. (6.56)] to the induced energy densities, based on the Padé approximants $[2/2]$, $[2/4]$ and $[4/4]$ for the MBP's (6.55), as functions of $\tilde{a}$, at fixed values of $p=\tilde{b}/\tilde{a}$: (a) $p=0$; (b) $p=0.5$; (c) $p=1.0$; (d) $p=5.0$.

The numerics clearly confirm that these MBP's (6.56) are well behaved, i.e., they approximate well the actual full induced energy density $\delta\tilde{\mathcal{U}}(\tilde{a};p)$ in the region of $\tilde{a}$ which is getting wider when the Padé order indices N and M ($\approx N$) increase. The results are presented in Fig. 6.7, where the MBP's for the first three possible Padé order indices [2/2], [2/4] and [4/4], along with the exact numerical results, are shown as functions of $\tilde{a}$, at four fixed values of $p \equiv \tilde{b}/\tilde{a}$. Another reason why the results now behave better than those of the usual BP tranforms lies in the fact that the Padé approximants ([2/2], [2/4] and [4/4]) are now more diagonal than earlier ([1/2], [1/4] and [3/4]). This is due to one additional power of w in the MB series (6.55), as compared with the usual B series. The diagonal and near–diagonal Padé approximants are known to behave better than the (far) off–diagonal ones [130]. In fact, Fig. 6.7 suggest that clear improvement – extension of the $\tilde{a}$ range of agreement with the exact results – sets in when we switch from [2/2] to [4/4] MBP, while the off–diagonal [2/4] MBP may even be slightly worse than [2/2]. For comparison, we also included the results of the truncated perturbation series (TPS) made up of the first four nonzero terms (up to $\sim\tilde{a}^8$) of (6.41), i.e., the terms on which the presented Borel–Padé transforms are based. The case of the pure (quasi-)magnetic field was not included in these Figures because in this case $\delta\tilde{\mathcal{U}} = -\delta\tilde{\mathcal{L}}$ and thus the information on this case is contained in Fig. 6.6 (d).

6.4.4 Renormalons

This application of Borel–Padé transformations and their modification may give us some insights into how the quasianalytic continuation from the perturbative (small $\tilde{a}$) into the nonperturbative (large $\tilde{a}$) regions can be carried out in other theories whose exact behavior in the latter region is still theoretically unknown. One such example is the perturbative QCD (pQCD), where some observables are known at the next–to–next–to–leading order ($\mathrm{N^2LO}$). The coupling parameter in that case [$\tilde{a} \mapsto \alpha_s(Q^2)$] can be quite large when the relevant energies of the process are low ($Q \sim 1$ GeV), thus rendering the direct evaluation of the $\mathrm{N^2LO}$ TPS unreasonable or at best unreliable. When applying Borel–Padé transformations or modifications thereof to such series, we are faced with two major problems:

- The first problem is of a more technical nature. Since only very few, at most two, coefficients beyond the leading order are known, the Padé approximants associated

with the (modified) Borel transform of the series have low order indices ($N, M \leq 2$) and thus do not necessarily reproduce the location of the leading poles on the positive axis, if they exist, adequately.

- The second problem is of a deeper theoretical nature. Knowing too little about the behavior of QCD in, or close to, the nonperturbative regime, we do not know how to integrate over the possible positive poles in the inverse (modified) Borel transformation – this can be termed the infrared renormalon ambiguity [131].

In the discussed case of integrated fermionic fluctuations in strong (quasi–)Abelian fields – for the Lagrangian and energy densities – we do not face any of the two afore–mentioned problems since the exact solution is known. We have to apply CPV prescription in the integration of the Borel–Padé transform of the induced dispersive Lagrangian density, and in the modified Borel–Padé transform of the induced energy density. The CPV is the direct consequence of the path (ϵ parameter) in the exact solution (6.23) [$\Leftrightarrow$ (6.24)]. The knowledge of the full theoretical solution in the latter case also tells us that the pole structure of the usual Borel transform of the induced energy density is more complicated (double poles), so that we have to apply a modified Borel-Padé transform which changes the double poles into a single pole structure.

We point out that the positive poles – renormalons – discussed in this thesis cannot be directly identified with the usual infrared (ultraviolet) renormalons in QCD (QED). The latter renormalons, as defined in the literature [131], are interpreted in the perturbative language as originating from renormalon chains at low (high) momenta k. The renormalon chains are momentum–k gluon (photon) propagators with n chained one–loop insertions, where n can be arbitrarily large. In the model at hand, however, only quantum fluctuations of fermions, in the slowly–varying strong fields, are considered; the effects of the quantum fluctuations of propagating gluons (photons) were not included in the discussed effective model. The positive poles, i.e. renormalons, in the present model originate from a collective effect of arbitrarily many very soft gluons (photons) coupling to a fermion loop or to a fermion propagator – cf. [132]. The relevant parameter of the effective coupling of these soft gauge bosons to the fermions, appearing in the induced effective action, is $\tilde{a} = ga/m^2$ and it can be large due to the strong field a and/or due to the strong coupling g. These nonperturbative contributions are then roughly $\sim \exp(-\text{const.}/\tilde{a}) = \exp[-\text{const.}m^2/(ga)]$ – cf. (6.51), (6.56). This is similar, but

not identical, to the infrared renormalon contributions in QCD $\sim\exp(-\text{const.}'/g^2)$. We may be tempted to term the renormalons discussed in this thesis as infrared renormalons due to their nonperturbative origin in the infrared, although this name is reserved for the afore–mentioned QCD–type renormalons.

6.5 Borel-Padé vs Borel-Weniger Method

Various QCD and QED applications of the Borel-Padé approach, with CPV prescription, have been made in [133–135]. The new method of Ref. [135] gives modified real and imaginary parts of the Borel–Padé of $\delta\tilde{\mathcal{L}}$, in comparison to the usual CPV prescription, when the Padé approximants $[N/M]_B$ have poles off the positive real axis. This may influence the speed of the convergence of the Borel–Padé transforms towards the full solution when the Padé order indices N and M ($\approx N$) increase.

Two other references [126, 136] are also somewhat related to our work. Dunne and Hall [136] considered, among other things, the question of resummation of the (one–loop) Euler–Heisenberg (EH) Lagrangian density by using the knowledge of the perturbation expansion of the Borel transform. Since they did not use Padé in addition, they needed at least an approximate information on *all* the coefficients of the series to reconstruct approximately the nonperturbative sector. Jentschura *et al.* [126], on the other hand, did not employ the Borel transform, but applied directly to truncated perturbation series (TPS) of the EH density a numerical method (Weniger sequence transformation) which differs from Padé in several aspects. Their results of resummation are better than the direct application of Padé to the TPS of the EH Lagrangian.

We present in this section numerical evidence for a QED and QCD example suggeting that in this case the combined method of Borel-Padé works better than its analog Borel-Weniger, and that it may work better or comparably well in some of the cases when there are singularities on the positive axis in the Borel plane.

6.5.1 A QED Example

Since we worked out the efficiency of the Borel-Padé method on the EH Lagrangian densitiy in previous section we start to apply the Borel-Weniger method for it. The authors of [126] proposed the use of Weniger (delta sequence) transformations as an alternative to

the use of Padé approximants, for direct resummation of truncated perturbation series. For a TPS of the form $F_{[n+1]}(z) = \sum_0^{n+1} \gamma_j z^j$, it is defined as [137]:

$$\delta_n^{(0)}(\zeta; \gamma_0, \ldots, \gamma_{n+1}) = \frac{\displaystyle\sum_j^n (-1)^j \binom{n}{j} \frac{(\zeta+j)_{n-1}}{(\zeta+n)_{n-1}} \frac{z^{n-j} F_{[j]}(z)}{\gamma_{j+1}}}{\displaystyle\sum_j^n (-1)^j \binom{n}{j} \frac{(\zeta+j)_{n-1}}{(\zeta+n)_{n-1}} \frac{z^{n-j}}{\gamma_{j+1}}} \ , \tag{6.57}$$

where $(\zeta+j)_{n-1} \equiv \Gamma(\zeta+j+n-1)/\Gamma(\zeta+j)$ are the Pochhammer symbols and $\zeta=1$ is usually taken. The approximant (6.57) is a ratio of two polynomials in z of power n each, and when expanded back in powers of z it reproduces all the terms of $F_{[n+1]}$.

The authors of [126] applied (6.57) directly to the TPS's of $\delta\tilde{\mathcal{L}}^{\text{pert.}}(\tilde{a}; p)/\tilde{a}^2$ of (6.31), and when re-expanding the approximant in powers of $\tilde{a}$ they were able to predict the next coefficient in the series with a better precision than the one provided by the corresponding diagonal (or almost diagonal) Padé approximant. Further, in the case of the pure magnetic field they showed that the method (6.57), when applied directly to the TPS's in $\tilde{b}$ of the induced Lagrangian density, [6] gave better results of resummation than the corresponding Padé approximants.

We now apply the method of (6.57) to the Borel transformation of (6.50), and compare the results of resummation obtained in this way with the results of the corresponding Borel–Padé approximants of the sec. 6.4. Formula (6.57) is applied to the Borel transform (6.50) divided by w with $\tilde{a} \to w$. We identify $z = w^2$. In the ensuing Borel–Weniger approximant, we integrate in the Laplace–Borel integral over the poles of the integrand with the CPV prescription, just as in Borel–Padé approximant (6.51), in accordance with the full known solution (6.52).

The results of these calculations are presented in Figs. 6.8(a)–(d), as functions of the electric field strength parameter $\tilde{a}$, for various values of $p \equiv \tilde{b}/\tilde{a} = 0., 0.5, 1.5, 5.0$. In Fig. 6.9 we present the analogous results for the case of the pure magnetic field (p.m.f.), as function of the magnetic field parameter $\tilde{b}$. N3 and [3/4] denote the Borel–Weniger and the Borel–Padé resummations based on the truncated Borel transform (6.50) with the first four nonzero terms (i.e., three terms beyond the leading order); N5 and [5/6] are based on the first six terms in (6.50). Comparison with the exact solutions, also present in the Figs. 6.8 and 6.9, suggests that the Borel–Padé is significantly better than the

[6] The approximants (6.57) applied to the TPS's of the series (6.34) divided by $\tilde{b}^2$.

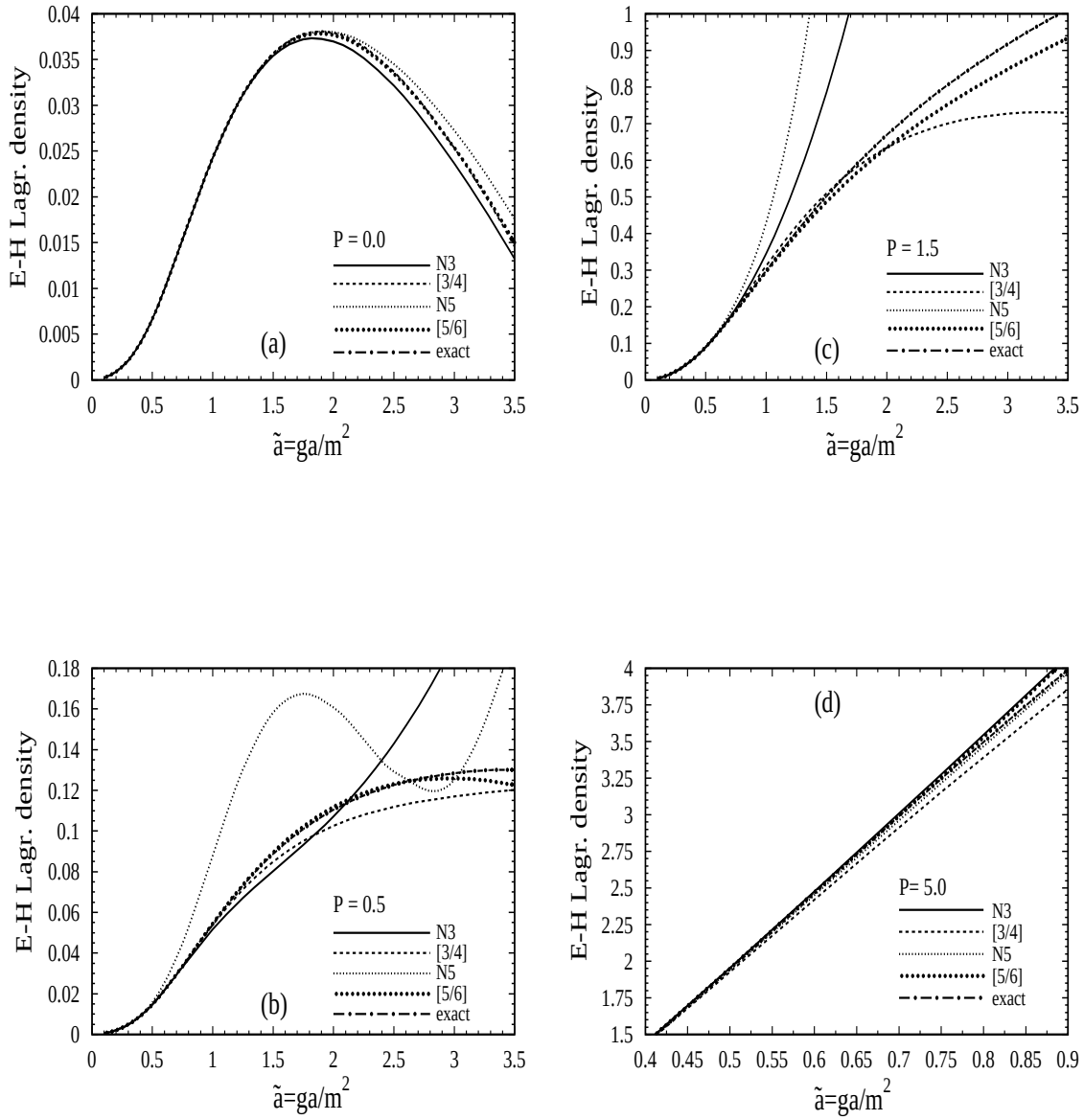

Figure 6.8: Borel–Padé approximants ([3/4], [5/6]) and the corresponding Borel–Weniger approximants (N3, N5) to the induced dispersive Lagrangian density (6.53), as functions of $\tilde{a}$, for various values of $p=\tilde{b}/\tilde{a}$: (a) $p=0.0$; (b) $p=0.5$; (c) $p=1.5$; (d) $p=5.0$. The numerically exact curves are included for comparison.

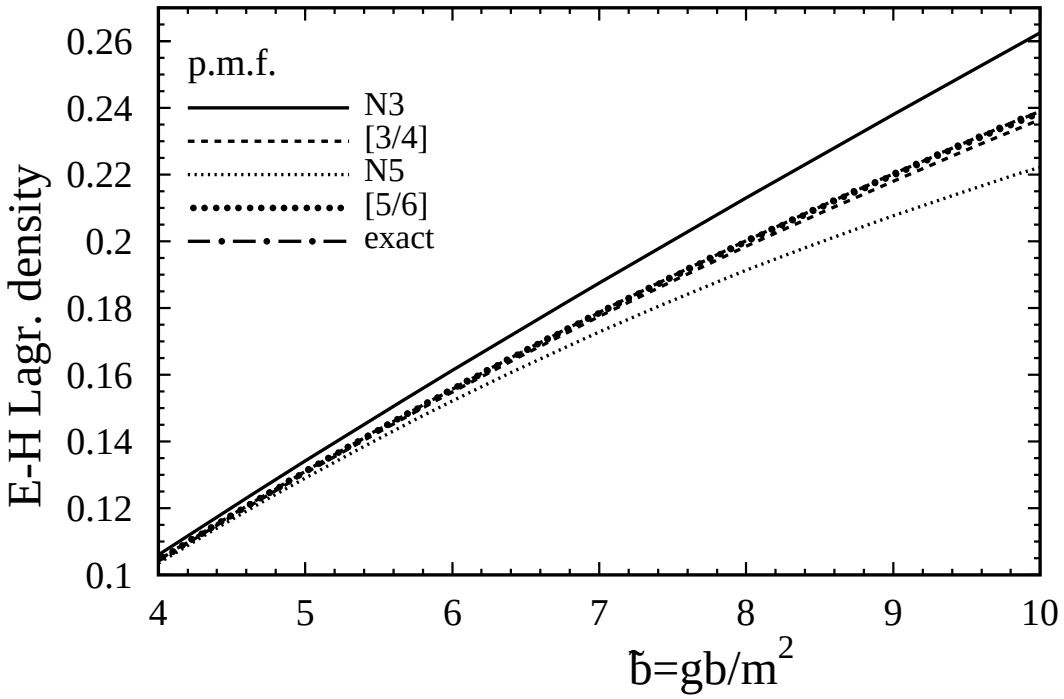

Figure 6.9: Borel–Padé approximants ([3/4], [5/6]) and Borel–Weniger approximants (N3, N5) to the induced dispersive Lagrangian density (6.33), as functions of $\tilde{b}$, for the pure magnetic field case ($\tilde{a}=0$). The numerically exact curve is included for comparison.

corresponding Borel–Weniger, except in the case of $p=5.0$ (electric field combined with a much stronger magnetic field). Further, comparison of Fig. 6.9 with the results of Table I of Ref. [126] suggests strongly that Borel–Padé and Borel–Weniger methods are much more efficient than Weniger method in resuming a series which has singularities in the Borel plane. Weniger method in the p.m.f. case is better than Padé method [126].

We can also do analogous calculations for the induced energy densities δU. In that case, the simple Borel transform has a double–pole structure on the positive real axis, and the Padé and Weniger approximants have trouble simulating such multiple poles adequately. Therefore, we employ a slightly modified Borel transform in the case of the

induced energy densities in (6.55) which has no multiple–pole structure – all the poles are simple. The (modified) Laplace–Borel integral in this case is:

$$\delta\tilde{\mathcal{U}}(\tilde{a};p) = \frac{1}{\tilde{a}}\int_0^\infty dw \exp\left(-\frac{w}{\tilde{a}}\right) \mathrm{MB}(w;p) \ , \tag{6.58}$$

where again the Cauchy principal value has to be taken, once $\mathrm{MB}(w;p)$ is replaced in (6.58) by its Padé or Weniger approximants. For details, we refer to the sec.6.4 where Borel–Padé was employed also for the induced energy densities. Weniger formula (6.57) is now applied to the modified Borel transform (6.55) divided by w^2. The results are presented in Figs. 6.10(a)–(d), as functions of $\tilde{a}$ at fixed $p = 0., 0.5, 1.5, 5.0$, respectively. [7] We present the solutions of Borel–Weniger and Borel–Padé based on the first four (N3, [4/4]) and six (N5, [6/6]) nonzero terms of the modified Borel transform of the energy density. We see that for the induced energy density the situation is less clear. In the cases $p = 0$, 0.5 and 5.0 the Borel–Padé and Borel–Weniger resummations are apparently of comparable quality, while at $p = 1.5$ the Borel–Padé appears to work better.

We can see these trends also if we compare the perturbation coefficients predicted by these two methods with the exact ones. These results are written in Table 6.1 for the case of the Lagrangian density (predicted c_9 and c_{13}) and in Table 6.2 for the case of the energy density (predicted d_9 and d_{13}). Predictions of the Borel–Padé are better in most cases, predictions of the Borel–Weniger are of comparable quality in the cases of $p = 0., 0.5, 5.0$ for energy density and in the case of $p = 5.0$ for Lagrangian density. In fact, in the case $p = 5.0$ of the energy density, the modified Borel–Weniger is slightly, but discernibly, better than the modified Borel–Padé. Comparing predictions of Table 6.1 (for $p = 0.0$) with those of Tables II and III of Ref. [126] suggests strongly that the discussed Borel–Padé and Borel–Weniger methods are better than the Weniger method in predicting the coefficients c_n. The Weniger method is better than the Padé method in predicting the c_n's [126].

6.5.2 A QCD Example

We compare the efficiency of the Borel–Padé and Borel–Weniger methods with an example from QCD, and it will have to do with the "fixing" of a pole of a Borel transform rather than with a resummation. We look at the Bjorken polarized sum rule (BjPSR), which

[7] In the case of the pure magnetic field, the energy density is the same as the Lagrangian density, except for the sign change.

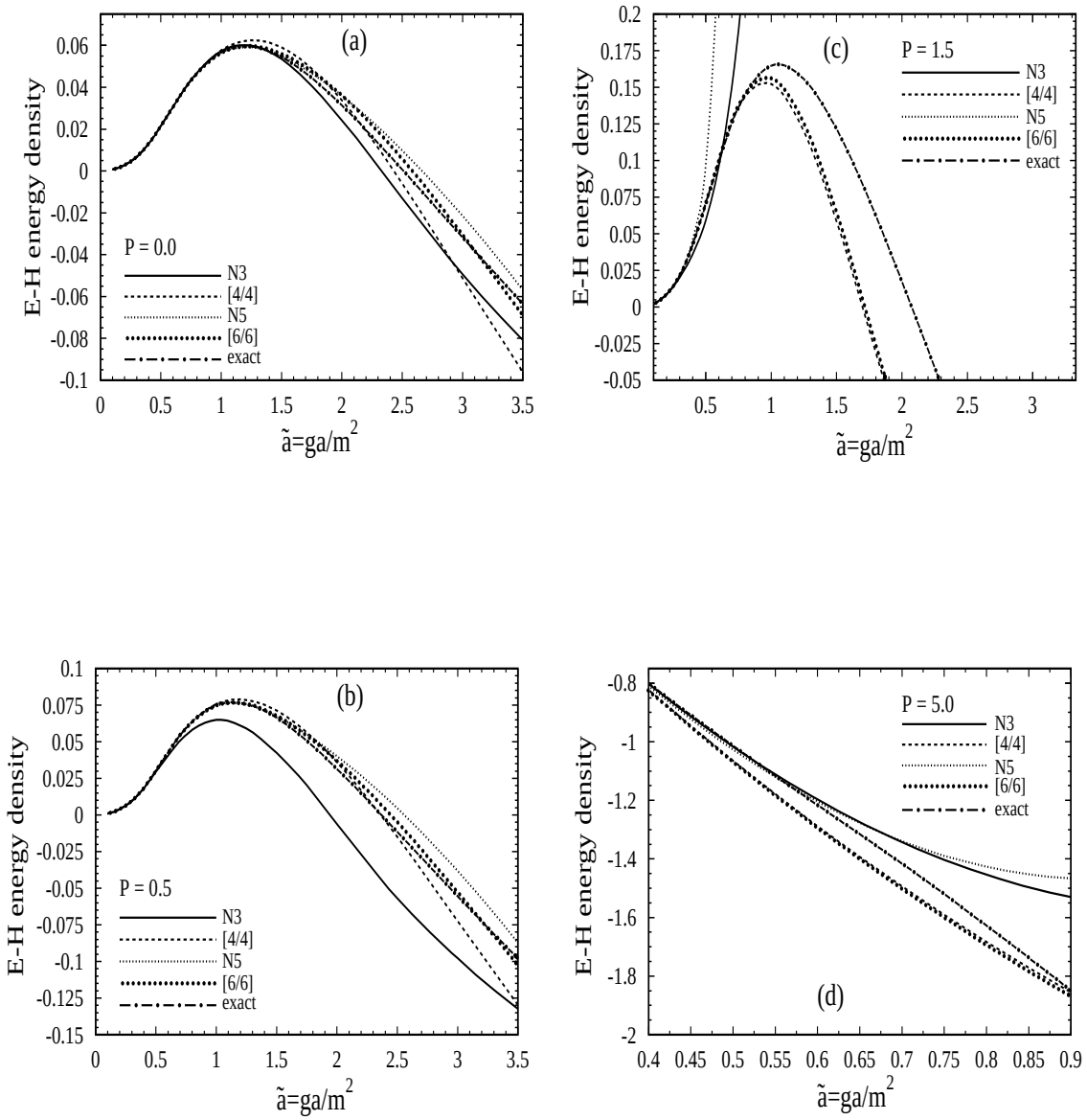

Figure 6.10: Modified Borel–Padé ([4/4], [6/6]) and the corresponding modified Borel–Weniger (N3, N5) approximants to the induced energy densities (6.53), as functions of $\tilde{a}$, at fixed values of $p=\tilde{b}/\tilde{a}$: (a) $p=0.0$; (b) $p=0.5$; (c) $p=1.5$; (d) $p=5.0$.

approximant	$p = 0.0$ and p.m.f	$p = 0.5$	$p = 1.5$	$p = 5.0$
N3	$c_9 = 2.1666{\cdot}10^{-6}$	$c_9 = 3.524{\cdot}10^{-6}$	$c_9 = 4.320{\cdot}10^{-4}$	$c_9 = 596.91$
[3/4]	$c_9 = 2.1637{\cdot}10^{-6}$	$c_9 = 3.648{\cdot}10^{-6}$	$c_9 = 5.866{\cdot}10^{-4}$	$c_9 = 595.28$
exact	$c_9 = 2.1644{\cdot}10^{-6}$	$c_9 = 3.711{\cdot}10^{-6}$	$c_9 = 6.166{\cdot}10^{-4}$	$c_9 = 596.24$
N5	$c_{13} = 2.2212{\cdot}10^{-8}$	$c_{13} = 3.725{\cdot}10^{-8}$	$c_{13} = 2.460{\cdot}10^{-5}$	$c_{13} = 3823.65$
[5/6]	$c_{13} = 2.2215{\cdot}10^{-8}$	$c_{13} = 3.804{\cdot}10^{-8}$	$c_{13} = 3.157{\cdot}10^{-5}$	$c_{13} = 3824.42$
exact	$c_{13} = 2.2215{\cdot}10^{-8}$	$c_{13} = 3.805{\cdot}10^{-8}$	$c_{13} = 3.161{\cdot}10^{-5}$	$c_{13} = 3824.45$

Table 6.1: Coefficients c_9 and c_{13} of the perturbation series for the induced Lagrangian density, as predicted by various Borel–Weniger and Borel–Padé approximants. We include exact values for comparison.

approximant	$p = 0.0$	$p = 0.5$	$p = 1.5$	$p = 5.0$
N3	$d_9 = 2.3752{\cdot}10^{-5}$	$d_9 = 3.8124{\cdot}10^{-5}$	$d_9 = 3.312{\cdot}10^{-4}$	$d_9 = -452.06$
[4/4]	$d_9 = 2.3658{\cdot}10^{-5}$	$d_9 = 3.7974{\cdot}10^{-5}$	$d_9 = 4.529{\cdot}10^{-6}$	$c_9 = -458.32$
exact	$d_9 = 2.3808{\cdot}10^{-5}$	$d_9 = 3.8085{\cdot}10^{-5}$	$d_9 = 2.503{\cdot}10^{-5}$	$c_9 = -464.01$
N5	$d_{13} = 3.3319{\cdot}10^{-7}$	$d_{13} = 5.4289{\cdot}10^{-7}$	$c_{13} = 8.162{\cdot}10^{-5}$	$c_{13} = -2977.3$
[6/6]	$d_{13} = 3.3309{\cdot}10^{-7}$	$d_{13} = 5.4291{\cdot}10^{-7}$	$c_{13} = -1.571{\cdot}10^{-6}$	$c_{13} = -2991.7$
exact	$d_{13} = 3.3322{\cdot}10^{-7}$	$d_{13} = 5.4301{\cdot}10^{-7}$	$c_{13} = -2.537{\cdot}10^{-6}$	$c_{13} = -2976.7$

Table 6.2: Coefficients d_9 and d_{13} of the perturbation series for the induced energy density, as predicted by various Borel–Weniger and Borel–Padé approximants. For comparison, exact values are included as well.

involves the isotriplet combination of the first moments over $x_{\rm Bj}$ of proton and neutron polarized structure functions:

$$\int_0^1 {\rm d}x_{\rm Bj} \left[g_1^{(p)}(x_{\rm Bj}; Q^2_{\rm ph}) - g_1^{(n)}(x_{\rm Bj}; Q^2_{\rm ph}) \right] = \frac{1}{6} |g_A| \left[1 - S(Q^2_{\rm ph}) \right] \ . \tag{6.59}$$

Here, $p^2 = -Q^2_{\rm ph} < 0$ is γ^* momentum transfer. At $Q^2_{\rm ph} = 3{\rm GeV}^2$ where three quarks are assumed active ($n_f = 3$), and if taking $\overline{\rm MS}$ scheme and renormalization scale (RScl) $Q_0^2 = Q^2_{\rm ph}$, we have the following TPS of the BjPSR observable $S(Q^2_{\rm ph})$ available [138]:

$$S_{[2]}(Q^2_{\rm ph}; Q_0^2 = Q^2_{\rm ph}; c_2^{\rm MS}, \quad c_3^{\rm MS}) = a_0(1 + 3.583 a_0 + 20.215 a_0^2) \ , \tag{6.60}$$

with:

$$a_0 = a(\ln Q_0^2; c_2^{\rm MS}, c_3^{\rm MS}, \ldots), \quad n_f = 3, \quad c_2^{\rm MS} = 4.471, \quad c_3^{\rm MS} = 20.99 \ . \tag{6.61}$$

Here we denoted by a the strong coupling parameter $a \equiv \alpha_s/\pi$.

It is known from [139, 140] that the Borel transform $B_S(z)$ of S has the lowest positive pole at $z_{\rm pole} = 1/\beta_0 = 4/9$ (leading infrared renormalon) and that this pole has a much stronger residuum than the highest negative pole at $z_{\rm pole} = -1/\beta_0$ (leading ultraviolet renormalon). The question we raise here is: How well can Padé and Weniger approximants to the Borel transform $B_S(z)$ determine the next coefficient r_3 of the term $r_3 a_0^4$ in the TPS (6.60), via the requirement that $z_{\rm pole} = 4/9$? For that, we have to know well the actual r_3. That term can be determined reasonably well on the basis of two approximants discussed in [141] – the effective charge approximant (ECH) $\mathcal{A}_S^{\rm (ECH)}(c_3)$ with $c_3 \approx 20.$, and another, also renormalization scale (RScl)– and renormalization scheme –independent approximant $\mathcal{A}_{S^2}^{1/2}(c_3)$ with $c_3 \approx 15.5$. These two approximants give the correct location of the leading infrared renormalon pole, and when we expand them back in powers of a_0 we obtain $r_3 \approx 129.4$ and $r_3 \approx 130.8$, respectively. Therefore, we can estimate with high confidence the actual value $r_3 = 130.0 \pm 1.0$.

It is important to consider the RScl–and scheme–invariant Borel transform when we want to apply Padé or Weniger approximants to it, so that the predicted values of r_3 will be independent of the RScl– and scheme in which we work at the intermediate stage. Such a Borel transform has been used in [142], and we use its variant $\widetilde{B}_S(z)$ as specified in [141] [cf. Eqs. (6.59)–(6.61) there]. Such a Borel transform reduces (up to a z–dependent nonsingular factor) to the usual Borel transform in the approximation of the one–loop evolution. The resulting power expansion of $\widetilde{B}_S(z)$ up to $\sim z^3$ will depend on the coefficient r_3

$$\widetilde{B}_S(z) = 1 + \frac{32}{81}(\gamma - 1)y + (0.02078...)y^2 + \frac{8}{729}(-21.88... + \frac{1}{6}r_3)y^3 + \mathcal{O}(y^4) \ , \tag{6.62}$$

where $\gamma = 0.577...$ is Euler constant, and $y \equiv 2\beta_0 z$. If we apply [2/1] and [1/2] Padé approximants to the TPS (6.62) and demand $z_{\rm pole} = 1/\beta_0$ ($y_{\rm pole} = 2$), we obtain predictions $r_3 = 137.0$ and $r_3 = 128.0$, respectively. The prediction of [1/2] is significantly better, and this could possibly be explained with the more involved denominator structure of [1/2] in comparison to [2/1]. When applying to (6.62) Weniger formula (6.57) ($\delta_2^{(0)}$ with $\zeta = 1$), we obtain $r_3 = 135.3$. This is further away from the actual value of 130.0 ± 1.0 than the

prediction of [1/2]. In both [1/2] and $\delta_2^{(0)}$, the denominators are polynomials of quadratic degree in z.

To summarize this QCD example: We applied Padé and Weniger approximants to a (TPS of a) Borel transform of the Bjorken polarized sum rule and demanded that the leading infrared renormalon pole be reproduced correctly. Weniger approximant $\delta_2^{(0)}$ then apparently gives a somewhat worse prediction for the next coefficient than the corresponding Padé approximant [1/2].

Chapter 7

Summary

We introduced the concept of separation of the induced dispersive action into nonperturbative and perturbative parts. We then investigated numerically the nonperturbative contributions to the dispersive (real) part of the Lagrangian density and to the real energy density, induced by quantum fluctuations of fermions in the strong (quasi–)Abelian fields that don't change significantly in space–time over the typical fermionic Compton wavelengths $1/m$. There are only nonperturbative contributions in the absorptive (imaginary) part of the strong field Lagrangian density, the latter part being responsible for the fermion–antifermion pair creation. On the other hand, the nonperturbative contributions in the real (dispersive) sector are in general also significant and can often even dominate over the perturbative induced contributions there. The induced dispersive Lagrangian density modifies the Maxwell equations for strong fields. The induced energy density is in principle an observable quantity. When the (quasi-)electric fields are strong, however, these densities decay fast (in $\sim 10^3$ Compton times, for $\tilde{a} \sim 1$). These two induced densities lead to a change in the dielectric permeability tensor of the vacuum. In the special case of QED, all these induced effects are below one per cent unless the fields are huge ($\tilde{a} \sim 10^2$).

We then used the discussed induced quantities as a "laboratory" to test and investigate the efficiency of specific methods of quasianalytic continuation from the perturbative region (weak fields) into the nonperturbative region (strong fields). We employed the method of Borel–Padé for the induced dispersive Lagrangian density, since the function represented by the Borel transform series has only simple poles. For the induced energy density, we had to employ a modified Borel–Padé transformation since the function represented by the (nonmodified) Borel transform series has double poles. We found out

numerically that such quasianalytic continuations become precise over an increasing region of the effective expansion parameter $\tilde{a}$ when the number of available terms in the perturbative expansion increases. This means that the quasianalytic continuation gradually becomes the analytic (exact) continuation when the number of the perturbative expansion terms accounted for increases. The Borel integration over positive poles (renormalons) is necessary. The correct prescription for the integration over these poles, in the case at hand, is the simplest one – the Cauchy principal value (CPV) prescription, its origin being the path (ϵ parameter) in the exact solution (6.23) [$\Leftrightarrow$ (6.24)]. Such analyses could give us some insight into the problems faced in QCD when nonperturbative contributions to observables are investigated either on the basis of the perturbative results themselves or by using other models [143] that are at least partly motivated by perturbative methods.

The correct analytic continuation, in the discussed case of strong background gauge fields, is the one employing the simplest (CPV) prescription for integration over the poles in the Laplace–Borel integral. This appears to be in agreement with the conclusions of Ref. [144] which were obtained from quite different considerations involving the renormalization group – that the vacuum polarization induced by the intense gauge fields is in principle determined by the information on the behavior of the theory in the perturbative region. The situation in QCD is less clear. A necessary condition for the existence of the (correct) analytic continuation from the perturbative into the nonperturbative regime in QCD is that a nontrivial infrared stable fixed point exist for the running strong coupling parameter. Such an infrared stable fixed point, however, seems to exist only if the number of the quark flavors is high ($N_f > 9$) [145]. For the real (low–N_f) QCD, a phase transition takes place, and methods of analytic continuation have probably only a limited range of applicability. Stated differently, in this case the full knowledge of the perturbative sector probably does not allow us to obtain information on the deep nonperturbative sector. In such a case, it is probable that even the renormalon ambiguity in the low–flavor perturbative QCD (pQCD) is an intrinsic ambiguity that cannot be entirely eliminated with pQCD–related methods alone.

Finally, We discussed the Padé approximants, the Delta sequence method and the combined methode of Borel-padé and Borel-weniger for the Euler-heisenberg Lagrangian (QED case) and the Bjorken polarized sum rule (QCD case) and compared their methodes. The predictions based on these methods have better results for the EH Lagrangian than the padé approximants and the delta tranformation alone.

Appendix A

Connection between Helicity Amplitudes of Zucker and the Rarita-Schwinger Form Factors for the N-Δ Transition

The relationships between the helicity amplitudes of Zucker in [37] and the Rarita-Schwinger form factors from Ref. [35] are given in the following way:

$$T_{\frac{3}{2}} = f(W)N_{RS}\,q_{CMS}\Big[\Big(\frac{W+M_N}{M_N}\Big)C_3^V + \frac{Wq^0_{CMS}}{M_N^2}\big(C_4^V + C_5^V\big) + \frac{Q^2}{M_N^2}C_5^V\Big] \quad \text{(A.1)}$$

$$T_{\frac{1}{2}} = \frac{1}{\sqrt{3}}f(W)N_{RS}q_{CMS}\Big[\Big(\frac{q^0_{CMS}-P^0_{CMS}-M_N}{M_N}\Big)C_3^V + \frac{Wq^0_{CMS}}{M_N^2}\big(C_4^V + C_5^V\big) + \frac{Q^2}{M_N^2}C_5^V\Big] \quad \text{(A.2)}$$

$$T_C = -\sqrt{\frac{2}{3}}f(W)N_{RS}\frac{q^2_{CMS}}{M_N}\Big[C_3^V + \frac{W}{M_N}\big(C_4^V + C_5^V\big) - \frac{q^0_{CMS}}{M_N}C_5^V\Big] \quad \text{(A.3)}$$

$$U_{\frac{3}{2}} = f(W)N_{RS}(P^0_{CMS}+M_N)\Big[\Big(\frac{W-M_N}{M_N}\Big)C_3^A + \frac{Wq^0_{CMS}}{M_N^2}C_4^A + C_5^A\Big] \quad \text{(A.4)}$$

$$U_{\frac{1}{2}} = \frac{1}{\sqrt{3}}f(W)N_{RS}(P^0_{CMS}+M_N)\Big[\Big(\frac{q^0_{CMS}+M_N-P^0_{CMS}}{M_N}\Big)C_3^A + \frac{Wq^0_{CMS}}{M_N^2}C_4^A + C_5^A\Big] \quad \text{(A.5)}$$

$$U_C = -\sqrt{\frac{2}{3}} f(W) N_{RS} (P^0_{CMS} + M_N) \frac{q_{CMS}}{M_N} \Big[C_3^A + \frac{W}{M_N} C_4^A - \frac{q^0_{CMS} M_N}{Q^2} C_5^A \Big] \quad \text{(A.6)}$$

$$U_D = \sqrt{\frac{2}{3}} f(W) N_{RS} (P^0_{CMS} + M_N) \frac{q^2_{CMS}}{M_N^2} \Big[C_5^A + C_6^A \Big], \quad \text{(A.7)}$$

where $P^0_{CMS} = \sqrt{M_N^2 + q^2_{CMS}}$ is the initial proton energy in the final πN center of mass system, $q^2_{CMS} = |\vec{q}|^2_{CMS}$, and the normalization factor

$$N_{RS} \equiv -i \sqrt{\frac{q_{CMS}}{4W(P^0_{CMS} + M_N)}}. \quad \text{(A.8)}$$

q_{CMS} is given by in Eq. (2.24).

Appendix B

Double Integration in the Function $f(\lambda)$

The double integration of the denominator in Eq. (2.98) with the effective length $L(b)$ is given by:

$$\begin{aligned} I &\equiv \int_{\infty} b\mathrm{d}b \int_{-\infty}^{\infty} \mathrm{d}z \frac{1}{1+e^{\frac{\sqrt{b^2+z^2}-C}{C_1}}} \\ &= 2\int_{\infty} b\mathrm{d}b \int_{0}^{+\infty} \mathrm{d}z \frac{1}{1+e^{\sqrt{b^2/C_1^2+z^2/C_1^2}-C/C_1}} \ . \end{aligned} \tag{B.1}$$

With the defined variables to simplify the integration:

$$x_1 = \frac{C}{C_1}, \quad u = \frac{z}{C_1}, \quad v = \frac{b^2}{C_1^2} \tag{B.2}$$

we get

$$I = C_1^3 \int_0^{\infty} \mathrm{d}v \int_0^{\infty} \mathrm{d}u \frac{1}{1+e^{\sqrt{v+u^2}-x_1}} \ . \tag{B.3}$$

Furthermore, we substitute $w = \sqrt{v+u^2} - x_1$ in Eq. (B.3):

$$\begin{aligned} I &= C_1^3 \int_{u-x_1}^{\infty} 2(w+x_1)\mathrm{d}w \int_0^{\infty} \mathrm{d}u \frac{1}{1+e^w} \\ &= 2\,C_1^3 \int_{-x_1}^{\infty} \mathrm{d}w \int_0^{w+x_1} \mathrm{d}u \frac{w+x_1}{1+e^w} \\ &= 2\,C_1^3 \int_{-x_1}^{\infty} \mathrm{d}w \frac{(w+x_1)^2}{1+e^w} \ . \end{aligned} \tag{B.4}$$

To calculate this integration we use Mathematica [146] and get the results as:

$$I = \frac{2}{3}C_1^3\left[\pi^2 x_1 + x_1^3 - 6\text{Polylog}(3, -e^{-x_1})\right] \tag{B.5}$$

with

$$\begin{aligned}\text{Polylog}(3, -e^{-x_1}) &= \sum_{n=1}^{\infty} \frac{(-e^{-x_1})^n}{n^3} \\ &= \sum_{k=1}^{\infty} e^{-2kx_1}\left(\frac{1}{(2k)^3} - \frac{e^{x_1}}{(2k-1)^3}\right) .\end{aligned} \tag{B.6}$$

Appendix C

The Limit of $\sigma_{\pm} = 0$

We discuss here two limit cases, i.e. $\sigma_{\pm} = 0$ in Eq. (2.145). The case of $\sigma_{+} = 0$ is given by:

$$\begin{aligned} \rightarrow \sigma &= \sqrt{1-\sigma_{-}}, \\ \mu &= \frac{1+\sigma_{-}}{\sigma_{-}} e^{\kappa\sigma L} \end{aligned} \tag{C.1}$$

and $\sigma_{-} = 0$ case:

$$\begin{aligned} \rightarrow \sigma &= \sqrt{1-\sigma_{+}}, \\ \mu &= \frac{2(1+\sigma_{+})}{\sigma_{-}} e^{\kappa\sigma L}. \end{aligned} \tag{C.2}$$

As it can be seen, the limit of $\sigma_{-} = 0$ gives the parameter μ which is infinite. For this reason we change the ansatz in Eq. (2.143) by taking instead

$$h(y) = \rho e^{\kappa\sigma y} + e^{-\kappa\sigma y}. \tag{C.3}$$

After the same calculations we get the following result:

$$\begin{aligned} \rho &= -\frac{\sigma_{-} e^{-\kappa\sigma L}}{1-\sigma_{+}} + \sigma \\ \sigma &= \sqrt{(1-\sigma_{+})^2 - \sigma_{-}^2}. \end{aligned} \tag{C.4}$$

In the case of $\sigma_{-} = 0$:

$$\begin{aligned} \sigma &= (1-\sigma_{+}), \\ \rho &= 0 \end{aligned} \tag{C.5}$$

and $\sigma_+ = 0$:

$$\begin{aligned} \sigma &= \sqrt{1-\sigma_-^2}, \\ \rho &= -\frac{\sigma_- e^{\kappa\sigma L}}{1+\sqrt{1-\sigma_-^2}} \end{aligned} \tag{C.6}$$

It follows that the limit $\sigma_- = 0$ is regular and the limit $\sigma_+ = 0$ case is not very evident.

Appendix D

Example calculation of the ratio $r = (\sigma(\pi^+) + \sigma(\pi^-))/\sigma(\pi^0)$

In this appendix we calculate the ratio $r = (\sigma(\pi^+) + \sigma(\pi^-))/\sigma(\pi^0)$ of charged current cross sections for propane (C_3H_8) and halon (CF_3Br) targets which have been used by the CERN Gargamelle experiment [65]. This experiment utilized a wide band neutrino beam with an average neutrino energy $< E_\nu > \sim 2$ GeV, see p. 29 in [65]. In the case of a halon target we compare with an experimental measurement of the ratio.

Considering a neutrino energy $E_\nu = 2.0$ GeV[1], we can read off the charged current cross sections for free nucleons from Figs. 2.3–2.8

$$\begin{aligned}
\sigma^+(p) &\equiv \sigma(\nu_\mu + p \to \mu^- + p + \pi^+) = 0.668 \times 10^{-38}\text{cm}^2 \\
\sigma^+(n) &\equiv \sigma(\nu_\mu + n \to \mu^- + n + \pi^+) = 0.179 \times 10^{-38}\text{cm}^2 \\
\sigma^0(p) &\equiv \sigma(\bar{\nu}_\mu + p \to \mu^+ + n + \pi^0) = 0.122 \times 10^{-38}\text{cm}^2 \\
\sigma^0(n) &\equiv \sigma(\nu_\mu + n \to \mu^- + p + \pi^0) = 0.2 \times 10^{-38}\text{cm}^2 \\
\sigma^-(p) &\equiv \sigma(\bar{\nu}_\mu + p \to \mu^+ + p + \pi^-) = 0.139 \times 10^{-38}\text{cm}^2 \\
\sigma^-(n) &\equiv \sigma(\bar{\nu}_\mu + n \to \mu^+ + n + \pi^-) = 0.312 \times 10^{-38}\text{cm}^2 \ .
\end{aligned}$$

Furthermore, it is convenient to introduce the column vectors

$$\vec{\sigma} \equiv \begin{pmatrix} \sigma^+ \\ \sigma^0 \\ \sigma^- \end{pmatrix}, \quad \vec{\sigma}(p) = \begin{pmatrix} 0.668 \\ 0.122 \\ 0.139 \end{pmatrix} \times 10^{-38}\text{cm}^2, \quad \vec{\sigma}(n) = \begin{pmatrix} 0.179 \\ 0.2 \\ 0.312 \end{pmatrix} \times 10^{-38}\text{cm}^2 \ .$$

[1] The ratio r depends only weakly on the neutrino energy. We have checked this explicitly by performing the calculations below with an energy $E_\nu = 6$ GeV giving very similar results.

Propane

Considering the propane target as a collection of free nucleons we can write

$$\begin{aligned}\vec{\sigma}_{\text{free}}(C_3H_8) &= 3\ \vec{\sigma}_{\text{free}}({}_6C^{12}) + 8\ \vec{\sigma}_{\text{free}}(H) \\ &= 3\ [Z\ \vec{\sigma}(p) + (A-Z)\ \vec{\sigma}(n)] + 8\ \vec{\sigma}(p) \\ &= 24\ \vec{\sigma}(p) + 18\ \vec{\sigma}(n)\ .\end{aligned}$$

Thus, $\vec{\sigma}_{free}(C_3H_8) = (19.254, 6.996, 8.952)^T \times 10^{-38}\text{cm}^2$ and the ratio for a free target is given by $r_{\text{free}} = (19.254 + 8.952)/6.996 = 4.03$.

In order to take into account the nuclear corrections we proceed as follows. Since the various atoms in propane are only weakly bound (due to electro-magnetic interactions) we consider propane as $C_3H_8 \simeq 3 \times {}_6C^{12} + 8 \times H$, i.e.,

$$\begin{aligned}\vec{\sigma}(C_3H_8) &= 3\ \vec{\sigma}({}_6C^{12}) + 8\ \vec{\sigma}(H) \\ &\overset{\text{ANP}}{=} 3\ M({}_6C^{12})\ \vec{\sigma}_{\text{free}}({}_6C^{12}) + 8\ \vec{\sigma}_{\text{free}}(H)\end{aligned}$$

where the second equation can be calculated according to the ANP model with help of the charge exchange matrix $M({}_6C^{12})$ for carbon

$$M({}_6C^{12}) = A_p \begin{pmatrix} 0.805 & 0.149 & 0.047 \\ 0.149 & 0.703 & 0.149 \\ 0.047 & 0.149 & 0.805 \end{pmatrix} \tag{D.1}$$

with the parameter $A_p = 0.816$.[2] Using $\vec{\sigma}_{\text{free}}({}_6C^{12}) = (5.082, 1.932, 2.706)^T \times 10^{-38}\text{cm}^2$ (and of course $\vec{\sigma}_{\text{free}}(H) = \vec{\sigma}(p)$) we obtain $\vec{\sigma}(C_3H_8) = (16.375, 7.766, 7.734)^T \times 10^{-38}\text{cm}^2$. Therefore the ratio r including nuclear corrections is given by $r_{\text{nuc.corr.}} = (16.375 + 7.734)/7.766 = 3.1$.

Halon

Following the same steps as above we find for CF_3Br:

$$\begin{aligned}\vec{\sigma}_{free}(CF_3Br) &= \vec{\sigma}_{free}({}_6C^{12}) + 3\ \vec{\sigma}_{free}({}_9F^{19}) + \vec{\sigma}_{free}({}_{35}Br^{80}) \\ &= [6\ \vec{\sigma}(p) + 6\ \vec{\sigma}(n)] + 3\ [9\ \vec{\sigma}(p) + 10\ \vec{\sigma}(n)] + [35\ \vec{\sigma}(p) + 45\ \vec{\sigma}(n)] \\ &= 68\ \vec{\sigma}(p) + 81\ \vec{\sigma}(n).\end{aligned}$$

[2] Of course, the ratio r depends only mildly on the precise value of A_p since it is canceled to a large extent.

Therefore, $\vec{\sigma}_{free}(CF_3Br) = (59.923, 23.482, 34.724)^T \times 10^{-38}\text{cm}^2$ and the ratio is $r_{free} = (59.923 + 34.742)/23.482 = 4.03$.

The nuclear corrections require the charge exchange matrices $M(_6C^{12})$, $M(_9F^{19})$ and $M(_{35}Br^{80})$ which we take from Ref. [52]. Writing

$$\begin{aligned}\vec{\sigma}(CF_3Br) &= \vec{\sigma}(_6C^{12}) + 3\ \vec{\sigma}(_9F^{19}) + \vec{\sigma}(_{35}Br^{80}) \\ &= M(_6C^{12})\vec{\sigma}_{free}(_6C^{12}) + 3\ M(_9F^{19})\vec{\sigma}_{free}(_9F^{19}) + M(_{35}Br^{80})\vec{\sigma}_{free}(_{35}Br^{80})\end{aligned}$$

we find $\vec{\sigma}(CF_3Br) = (35.644, 21.245, 23.372)^T \times 10^{-38}\text{cm}^2$ and the ratio containing nuclear corrections is $r_{nuc.corr.} = (35.644 + 23.372)/21.246 = 2.78$. This compares favourably with the experimental result [65] $r_{\text{exp}} = 2.3 \pm 0.9$ for a CF_3Br target, whereas the ratio for a free target, $r_{\text{free}} = 4.03$, appears to be too large.

Appendix E

Kinematic Region of the Variables x and y in Deeply Inelastic Tau-Lepton Nucleon Scattering

The momentum transfer $q^2 = -Q^2$ in DIS (see Fig. 3.1) is given by:

$$\begin{aligned} Q^2 &= 2k_1 \cdot k_2 - m_l^2 \\ &= 2E_\nu E_l - 2E_\nu k_2^0 \cos\theta - m_l^2 \end{aligned} \tag{E.1}$$

with $k_2^0 = \sqrt{E_l^2 - m_l^2}$. From this we can easily read the following relations:

$$Q^2_{min,max} = 2E_\nu(E_\nu - \nu) \pm 2E_\nu\sqrt{(E_\nu - \nu)^2 - m_l^2} - m_l^2 \tag{E.2}$$

using $\nu = E_\nu - E_l$. $Q^2_{min,max}$ denotes the minimum and the maximum of Q^2, respectively. Combining the variables $x = \frac{Q^2}{2M_N\nu}$ and $y = \frac{\nu}{E_\nu}$ we obtain $Q^2 = 2M_N E_\nu xy = (s - M_N^2)xy$ with $s = (k_1 + p)^2 = M_N^2 + 2M_N\nu$, $\nu = E_\nu y$. Substituting x, y into $Q^2_{min,max}$ in Eq. (E.2) is obtained as follows:

$$Q^2_{min,max} = 2E_\nu^2(1-y) - m_l^2 \pm 2E_\nu^2\sqrt{(1-y)^2 - \frac{m_l^2}{E_\nu^2}}. \tag{E.3}$$

$$\Rightarrow \quad 2E_\nu^2(1-y) - m_l^2 - 2E_\nu^2\sqrt{(1-y)^2 - \frac{m_l^2}{E_\nu^2}} \leq Q^2 = 2M_N E_\nu xy$$

$$\leq 2E_\nu^2(1-y) - m_l^2 + 2E_\nu^2\sqrt{(1-y)^2 - \frac{m_l^2}{E_\nu^2}} \tag{E.4}$$

$$\Leftrightarrow \quad \underbrace{\frac{E_\nu}{M_N x}(1-y) - \frac{m_L^2}{2M_N E_\nu x}}_{d_1} - \underbrace{\frac{E_\nu}{M_N x}\sqrt{(1-y)^2 - \frac{m_l^2}{E_\nu^2}}}_{d_2} \leq y$$

$$\leq \underbrace{\frac{E_\nu}{M_N x}(1-y) - \frac{m_L^2}{2M_N E_\nu x}}_{d_1} + \underbrace{\frac{E_\nu}{M_N x}\sqrt{(1-y)^2 - \frac{m_l^2}{E_\nu^2}}}_{d_2} \tag{E.5}$$

$$\Leftrightarrow \quad d_1 - d_2 \leq y \leq d_1 + d_2 \tag{E.6}$$

$$\Rightarrow \quad |y - d_1| \leq d_2 \tag{E.7}$$

$$\Rightarrow \quad (y-d_1)^2 - d_2^2 = 0. \tag{E.8}$$

Using two following conditions from Eq. (E.3):

- $\sqrt{(1-y)^2 - \frac{m_l^2}{E_\nu^2}}$ is real.
- $Q^2_{\text{min}} \geq 0$.

We get the y region from the first condition as follows:

$$y \leq 1 - \frac{m_l}{E_\nu}. \tag{E.9}$$

since from the second condition we have negative y range, we do not take it into account. We obtained the final results in Eq. (3.13) solving $(y-d_1)^2 - d_2^2 = 0$ in Eq. (E.8).

Appendix F

Unitary Transformation Leading to Harmonic Oscillators

We want to find a unitary operator $\hat{U}$ which "diagonalizes" the scalar density for the covariantly homogeneous strong abelian field (6.6):

$$\left[\hat{P} - gA\right]^2 = \left(\hat{P}^0\right)^2 - \left(\hat{P}^1\right)^2 - \left(\hat{P}^2 - g\mathcal{B}_{\|}\hat{X}^1\right)^2 - \left(\hat{P}^3 + g\mathcal{E}\hat{X}^0\right)^2 , \qquad \text{(F.1)}$$

into the sum of two harmonic oscillator densities as written in (6.17). This approach can be regarded as a generalization of the approach by Itzykson and Zuber [106]. Since the latter authors used a relatively simple unitary "diagonalizing" operator for the case of a homogeneous electromagnetic field, we adopt their consideration and use the commutation relations: $[\hat{X}^\mu,\hat{P}^\nu] = -\mathrm{i}g^{\mu\nu}$, and $P^\nu = \mathrm{i}\partial^\nu$. In fact, using the mentioned commutation relations and the operator identity[1]

$$\begin{aligned} \exp\left(\hat{B}\right)\hat{A}\exp\left(-\hat{B}\right) &= \hat{A} + \frac{1}{1!}\left[\hat{B},\hat{A}\right] + \frac{1}{2!}\left[\hat{B},\left[\hat{B},\hat{A}\right]\right] + \dots \\ &\quad + \frac{1}{n!}\left[\hat{B},\left[\hat{B},\dots\left[\hat{B},\hat{A}\right]\dots\right]\right] + \dots , \end{aligned} \qquad \text{(F.2)}$$

we can derive the following useful formulas for the case $\mu \neq \nu$:

$$\exp\left(\mathrm{i}\alpha\hat{P}^\mu\hat{P}^\nu\right)\left(\hat{X}^\delta\right)\exp\left(-\mathrm{i}\alpha\hat{P}^\mu\hat{P}^\nu\right) = \hat{X}^\delta - \alpha g^{\nu\delta}\hat{P}^\mu - \alpha g^{\mu\delta}\hat{P}^\nu. \qquad \text{(F.3)}$$

We can now make the following ansatz for the unitary operator $\hat{U}$:

$$\hat{U} = \exp\left(\mathrm{i}\xi_1\hat{P}^1\hat{P}^2\right)\exp\left(\mathrm{i}\xi_2\hat{P}^0\hat{P}^3\right) . \qquad \text{(F.4)}$$

[1] This identity can be proved, for example, by introducing an operator $\hat{F}(\alpha) = \exp(\alpha\hat{B})\hat{A}\exp(-\alpha\hat{B})$; it is straightforward to show that $d^n\hat{F}(\alpha)/d\alpha^n = [\hat{B},[\hat{B},\dots[\hat{B},\hat{F}]\dots]]$, where the latter expression involves n commutators; Taylor expansion of $\hat{F}(1)$ around the point $\alpha = 0$ then leads to (F.2).

Using the above two formulas and the unitarity of $\hat{U}$, we can show the following: the $\hat{P}^k$ (k=2,3) operators in (F.1) vanish

$$\begin{aligned}\hat{U}\left[\hat{P}-gA(\hat{X})\right]^2\hat{U}^\dagger &= \left(\hat{U}\left[\hat{P}-gA(\hat{X})\right]\hat{U}^\dagger\right)^2 \\ &= \left(\hat{P}^0\right)^2-\left(\hat{P}^1\right)^2-g^2\mathcal{E}^2\left(\hat{X}^0\right)^2-g^2\mathcal{B}_\parallel^2\left(\hat{X}^1\right)^2, \qquad \text{(F.5)}\end{aligned}$$

where

$$\hat{U}=\exp\left(\mathrm{i}g^{-1}\mathcal{B}_\parallel^{-1}\hat{P}^1\hat{P}^2\right)\exp\left(\mathrm{i}g^{-1}\mathcal{E}^{-1}\hat{P}^0\hat{P}^3\right). \qquad \text{(F.6)}$$

Thus final result is:

$$\hat{U}\left[\hat{P}-gB(\hat{X})\right]^2\hat{U}^\dagger = \left[\left(\hat{P}^0\right)^2-g^2a^2(\hat{X}^0)^2\right]-\left[(\hat{P}^1)^2+g^2b^2(\hat{X}^1)^2\right] \qquad \text{(F.7)}$$

with

$$\begin{aligned}a &= \left[+\vec{\mathcal{E}}^2-\vec{\mathcal{B}}^2+\sqrt{\left(\vec{\mathcal{E}}^2-\vec{\mathcal{B}}^2\right)^2+4\left(\vec{\mathcal{E}}\cdot\vec{\mathcal{B}}\right)^2}\right]^{1/2}/\sqrt{2}\,, \\ b &= \left[-\vec{\mathcal{E}}^2+\vec{\mathcal{B}}^2+\sqrt{\left(\vec{\mathcal{E}}^2-\vec{\mathcal{B}}^2\right)^2+4\left(\vec{\mathcal{E}}\cdot\vec{\mathcal{B}}\right)^2}\right]^{1/2}/\sqrt{2}\,.\end{aligned}$$

Appendix G

Tracing over the Harmonic Oscillator Degrees of Freedom

Here we calculate traces (integrals) of exponentiated harmonic oscillators appearing in expression (6.20), i.e., we calculate:

$$T_1(s) = \int_{-\infty}^{+\infty} \mathrm{d}q^0 \left\langle q^0 \left| \mathrm{e}^{2\mathrm{i}s\mathcal{H}^{(1)}} \right| q^0 \right\rangle \ , \quad T_2(s) = \int_{-\infty}^{+\infty} \mathrm{d}q^1 \left\langle q^1 \left| \mathrm{e}^{-2\mathrm{i}s\mathcal{H}^{(2)}} \right| q^1 \right\rangle \ , \tag{G.1}$$

where $\mathcal{H}^{(k)}$ ($k=1,2$) are Hamiltonian densities of harmonic oscillators:

$$\mathcal{H}^{(1)} = \left\{ \frac{1}{2}\hat{P}^0\hat{P}^0 - \frac{g^2a^2}{2}\hat{X}^0\hat{X}^0 \right\} \ , \tag{G.2}$$

$$\mathcal{H}^{(2)} = \left\{ \frac{1}{2}\hat{P}^1\hat{P}^1 + \frac{g^2b^2}{2}\hat{X}^1\hat{X}^1 \right\} \ . \tag{G.3}$$

Expressions (G.2)-(G.3) show that, in a rotated basis, $\mathcal{H}^{(1)}$ and $\mathcal{H}^{(2)}$ are sets of oscillators each, with frequency parameters $\omega = \mathrm{i}ga$ and $\omega = gb$, respectively, and with mass parameter $m = 1$. Since tracing (G.1) for these oscillators can be done in any complete basis, we choose instead of momentum-eigenstate basis $|q^0\rangle$ ($|q^1\rangle$) the basis of eigenstates of the c-number Hamiltonian densities $\mathcal{H}^{(k)}$ ($k=1,2$). Eigenenergies $\mathrm{i}E^{(1)}(m)$ (imaginary positive) of the first set, and $E^{(2)}(m)$ (real positive) of the second set of harmonic Hamiltonians are then:

$$\mathrm{i}E^{(1)}(m) = \mathrm{i}ga\left(m + \frac{1}{2}\right) \ , \tag{G.4}$$

$$E^{(2)}(m) = gb\left(m + \frac{1}{2}\right) \ ,$$

where $m=0,1,2,\cdots$ are the energy quantum numbers of the harmonic oscillators. Tracing therefore reduces to simple geometric sums:

$$\begin{aligned}\int_{-\infty}^{+\infty} dq^0 \left\langle q^0 \left| \exp\left[2\mathrm{i}s\mathcal{H}^{(1)}\right] \right| q^0 \right\rangle &= \sum_{m=0}^{\infty} \exp\left[2\mathrm{i}sE^{(1)}(m)\right] \\ &= \exp\left[-gsa\right] \sum_{m=0}^{\infty} \left\{\exp\left[-2gsa\right]\right\}^m \\ &= \frac{1}{2\sinh\left[gsa\right]} \ , \end{aligned} \tag{G.5}$$

$$\begin{aligned}\int_{-\infty}^{+\infty} dq^1 \left\langle q^1 \left| \exp\left[-2\mathrm{i}s\mathcal{H}^{(2)}\right] \right| q^1 \right\rangle &= \sum_{m=0}^{\infty} \exp\left[-2\mathrm{i}sE^{(2)}(m)\right] \\ &= \exp\left[-\mathrm{i}gsb\right] \sum_{m=0}^{\infty} \left\{\exp\left[-2\mathrm{i}gsb\right]\right\}^m \\ &= \frac{1}{2\mathrm{i}\sin\left[gsb\right]} \ . \end{aligned} \tag{G.6}$$

In order to ensure that the geometric sum in (G.6) converges, we have to move the proper time $s>0$ slightly below the real axis: $s \mapsto z = s - \mathrm{i}\varepsilon'$ ($\varepsilon' = +0$). Thus, the final result is obtained as follows:

$$T_1(s)\, T_2(s) = \frac{1}{4\mathrm{i}\sinh\left[gza\right]\sin\left[gzb\right]} \ . \tag{G.7}$$

Keeping in mind notation (G.1) for matrices $T_1(s)$ and $T_2(s)$, as well as notation (6.17), we see that the resulting formula (G.7) proves the implication (6.20)⇒(6.21).

Appendix H

On the Analyticity of $\delta\tilde{\mathcal{L}}_0$

In this appendix we will clarify the nature of the nonanalytic terms $\sim\exp(-\text{const.}/\tilde{a})$ that appear in the naive expansion of the perturbative part $\mathrm{Re}\delta\tilde{\mathcal{L}}_0(\tilde{a};p)$ of (6.26) around the point $\tilde{a}=0$. Such terms may in principle be dangerous for our interpretation of (6.26) as the perturbative part of the induced Lagrangian density, because they have the nonanalytic structure similar to those terms that appear in the nonperturbative parts $\mathrm{Re}\delta\tilde{\mathcal{L}}_n(\tilde{a};p)$ of (6.27), the latter containing genuinely nonperturbative contributions due to the singular (pole) structure of the integrand. We will show that the mentioned terms in (6.26) are an artifact of having the abrupt infrared (IR) cutoff there, and that they disappear as soon as the abruptness of the infrared cutoff is (infinitesimally) softened.

In the proper–time formalism, the IR and UV regions correspond to the high and the low values of the proper time, respectively [147]. In the proper–time integral (6.24) for $\delta\mathcal{L}$, the IR region of large proper time z [$z\geq\pi/(ag)$] contains poles, the latter leading to nonperturbative effects. The region of smaller z has no such singularities and thus no nonperturbative effects. Therefore, the perturbative part of $\delta\mathcal{L}$ should cover the latter region, and suppress the IR region. The general way to do this is to introduce, in the spirit of approaches of [147], a nonnegative regulator $\rho_\varepsilon(w)$ ($w\equiv agz$) in the proper–time integral:

$$\begin{aligned}\mathrm{Re}\delta\tilde{\mathcal{L}}^{(\mathrm{P.})}_\varepsilon(\tilde{a};p) &= -\mathrm{Re}\int_0^\infty\frac{dw}{w}\rho_\varepsilon(w)\exp\left(-\frac{w}{\tilde{a}}\right)\times\\ &\quad\left[p\cot(w+\mathrm{i}\epsilon')\coth(pw)+\frac{1}{3}(1-p^2)-\frac{1}{w^2}\right]\ ,\end{aligned}\tag{H.1}$$

where the minimal IR regularization requirements are

$$\rho_\varepsilon(w)\approx 1\quad\text{for } w\ll 1\ ,\qquad \rho_\varepsilon(w)\ll 1\quad\text{for } w\stackrel{>}{\approx}\pi\ .\tag{H.2}$$

The nonnegative parameter ε indicates that we can choose a class of such regulators. In fact, we will require that for small ε a large chunk of the perturbative region, namely the w–region of approximately $[0, \pi/2]$, survive in (H.1). Thus we restrict the minimal conditions (H.2) to the following ones, when $\varepsilon \ll 1$:

$$\rho_\varepsilon(w) \approx 1 \quad \text{for } w \stackrel{<}{\approx} \pi/2 - \sqrt{\varepsilon}\ , \qquad \rho_\varepsilon(w) \ll 1 \quad \text{for } w \stackrel{>}{\approx} \pi/2 + \sqrt{\varepsilon}\ . \tag{H.3}$$

A seeming alternative to (H.1) would be to introduce a regulator $\rho_\varepsilon(z)$ that would scale as a function of $z \equiv w/(ag)$ instead of w. But this possibility must be discarded because then the condition of suppressing the pole structure $[\rho_\varepsilon(z) \ll 1$ for $z \geq \pi/(ga) \equiv \pi/(m^2\tilde{a})]$ cannot be reconciled with the condition of the survival of a large chunk of the perturbative region $[\rho_\varepsilon(z) \approx 1$ for $z \leq \pi/(2m^2\tilde{a})]$ at various values of $\tilde{a}$ simultaneously.

The conditions (H.3) are designed in such a way that the limit $\varepsilon \to +0$ would apparently lead to the abrupt IR regulator appearing in $\mathrm{Re}\delta\tilde{\mathcal{L}}_0(\tilde{a}; p)$ of (6.26), with the abrupt cutoff at $w = \pi/2$. We can choose the following specific one–parameter family of regulators $\rho_\varepsilon(w)$ satisfying the afore–mentioned conditions:

$$\rho_\varepsilon(w) \ = \ \frac{\tilde{\rho}_\varepsilon(w)}{\tilde{\rho}_\varepsilon(0)}\ , \quad \tilde{\rho}_\varepsilon(w) = \frac{1}{2} - \frac{1}{\pi}\arctan\left(\frac{w - \pi/2}{\varepsilon}\right)\ . \tag{H.4}$$

When $\varepsilon \to +0$ ($\varepsilon \neq 0$), these regulators differ from the abrupt cutoff regulator outside the narrow w–interval $[\pi/2 - \sqrt{\varepsilon}, \pi/2 + \sqrt{\varepsilon}]$ by at most $\sim\sqrt{\varepsilon}$

$$\rho_\varepsilon(w) = \left\{ \begin{array}{ll} 1 - (\varepsilon/\pi)(\pi/2 - w)^{-1} + \mathcal{O}(\varepsilon^2) & \text{if } w < \frac{\pi}{2} - \sqrt{\varepsilon} \\ (\varepsilon/\pi)(w - \pi/2)^{-1} + \mathcal{O}(\varepsilon^2) & \text{if } w > \frac{\pi}{2} + \sqrt{\varepsilon}\ , \end{array} \right\} \tag{H.5}$$

while they may differ from the abrupt version significantly only in the afore–mentioned narrow interval. The first thing to check would be that the regularized expression (H.1) with the regulator (H.4)–(H.5), in the limit $\varepsilon \to +0$ ($\varepsilon \neq 0$) really gives numerically the result (6.26) of the abrupt cutoff. Stated otherwise, we should check that the $\lim_{\varepsilon \to +0}$ in front of the integral (H.1) can be moved into the integral, without changing the result. For such a check, we need to see that the contributions in (H.1) from the singular (poles) regions ($w > \pi/2$) are suppressed toward zero when $\varepsilon \to +0$. Such a check is straightforward and we performed it. It turns out that the w–regions $[(n-1/2)\pi, (n+1/2)\pi]$ around the n'th pole $w_n = n\pi$ are suppressed by a factor $\sim\varepsilon$ when $n \geq 2$, and by at least a factor $\sim\sqrt{\varepsilon}$ when $n = 1$. Thus, all these contributions go to zero when $\varepsilon \to +0$. On the other hand, on the w–interval $[0, \pi/2]$, there are no singularities of the integrand and

the regulator is virtually equal to 1 in the entire interval when $\varepsilon \to +0$. Therefore, on this interval we can automatically push the limiting procedure into the integral. Thus we really have

$$\lim_{\varepsilon\to+0} \mathrm{Re}\delta\tilde{\mathcal{L}}_{\varepsilon}^{(\mathrm{P.})}(\tilde{a};p) = \mathrm{Re}\delta\tilde{\mathcal{L}}_{0}(\tilde{a};p) \ , \tag{H.6}$$

i.e., the numerical value of the perturbative part with the infinitesimally "softened" IR cutoff is the same as that of the perturbative part with the abrupt IR cutoff (6.26).

Now we will investigate the expansions of the above two expressions around the point $\tilde{a}=0$, in order to see the difference in the (non)analyticity structure between the two cases. We can find the small–$\tilde{a}$ expansion of $\mathrm{Re}\delta\tilde{\mathcal{L}}_0(\tilde{a};p)$ of (6.26) by expanding first the integrand (without the exponent) there, i.e., the Borel transform, in powers of w. As argued in section 6.4.2 [cf. Eqs. (6.50)–(6.52)], this expansion yields (6.50) with $\tilde{a}\mapsto w$, where $c_j(p)$'s are given by (6.32). Then the term–by–term integration over w leads to the small–$\tilde{a}$ expansion of $\mathrm{Re}\delta\tilde{\mathcal{L}}_0$:

$$\begin{aligned}
\mathrm{Re}\delta\tilde{\mathcal{L}}_0(\tilde{a};p)^{(\mathrm{exp.})} &= c_1(p)\int_0^{\pi/2} dw\exp(-w/\tilde{a})w + c_3(p)\int_0^{\pi/2} dw\exp(-w/\tilde{a})w^3 + \cdots \\
&= \left[c_1(p)1!\,\tilde{a}^2 + c_3(p)3!\,\tilde{a}^4 + \cdots\right] \\
&\quad -\tilde{a}\exp\left(-\frac{\pi}{2\tilde{a}}\right)\left[c_1(p)\left(\frac{\pi}{2}\right) + c_3(p)\left(\frac{\pi}{2}\right)^3 + \cdots\right] \\
&\quad +\mathcal{O}\left(\tilde{a}^2\exp[-\pi/(2\tilde{a})]\right) \ .
\end{aligned} \tag{H.7}$$

Incidentally, the coefficient at $\tilde{a}\exp[-\pi/(2\tilde{a})]$, written as an infinite sum, is just the value of the Borel transform at $w=\pi/2$ [cf. remark following Eq. (6.52)]:

$$\left[c_1(p)\left(\frac{\pi}{2}\right) + c_3(p)\left(\frac{\pi}{2}\right)^3 + \cdots\right] = \left(\frac{2}{\pi}\right)\left[\left(\frac{2}{\pi}\right)^2 - \frac{1}{3}(1-p^2)\right] \ . \tag{H.8}$$

The coefficients of terms $\mathcal{O}\left(\tilde{a}^2\exp[-\pi/(2\tilde{a})]\right)$ can be obtained in an analogous manner, by using derivatives of the Borel transform with respect to w at $w=\pi/2$. Expressions (H.7)–(H.8) show explicitly the following: In the small–$\tilde{a}$ expansion of $\mathrm{Re}\delta\tilde{\mathcal{L}}_0$ of (6.26), in addition to the usual perturbation expansion part (6.31) that is analytic at $\tilde{a}=0$, we obtain formally also terms $\sim\tilde{a}^n\exp[-\pi/(2\tilde{a})]$ which are nonanalytic at $\tilde{a}=0$. One might suspect that such terms could possibly be of nonperturbative origin, and below we will show that they are not. More specifically, we will show that they are an artifact of the abruptness of the IR cutoff and that they are de facto not there, in the sense that they disappear when we consider instead of $\mathrm{Re}\delta\tilde{\mathcal{L}}_0$ its numerical equivalent, i.e., the $\varepsilon\to+0$

limit of the left–hand side of (H.6). To show this, we have to expand the latter expression [at $\varepsilon \neq 0$ – i.e. (H.1)] around $\tilde{a}=0$. For that, we first Taylor–expand the regulator $\rho_\varepsilon(w)$ (H.4), which is analytic everywhere, [1] in powers of w for small ε:

$$\tilde{\rho}_\varepsilon(w) = \tilde{\rho}_\varepsilon(0) - w\,\frac{\varepsilon}{2}\left(\frac{2}{\pi}\right)^3 - \cdots - w^n\,\frac{\varepsilon}{2}\left(\frac{2}{\pi}\right)^{n+2} - \cdots + \mathcal{O}(\varepsilon^3)\ , \tag{H.9}$$

$$\tilde{\rho}_\varepsilon(0) = 1 - \frac{2}{\pi}\varepsilon + \mathcal{O}(\varepsilon^3)\ . \tag{H.10}$$

The other part of the integrand in (H.1), without the exponent, is the Borel transform whose small–$\tilde{a}$ expansion is (6.50) with $\tilde{a} \mapsto w$. Combining this and (H.9)–(H.10), we obtain after some straightforward algebra [2] the small–$\tilde{a}$ expansion of (H.1) around $\tilde{a}=0$ for small ε:

$$\begin{aligned}
\mathrm{Re}\delta\tilde{\mathcal{L}}_\varepsilon^{(\mathrm{P.})}(\tilde{a};p)^{(\mathrm{exp.})} = {} & \left[c_1(p)1!\,\tilde{a}^2 + c_3(p)3!\,\tilde{a}^4 + c_5(p)5!\,\tilde{a}^6\cdots\right] \\
& -\varepsilon\frac{1}{2}\left(\frac{2}{\pi}\right)^3\left\{c_1(p)2!\,\tilde{a}^3 + \left(\frac{2}{\pi}\right)c_1(p)3!\,\tilde{a}^4\right. \\
& + \left[\left(\frac{2}{\pi}\right)^2 c_1(p) + c_3(p)\right]4!\,\tilde{a}^5 + \left[\left(\frac{2}{\pi}\right)^3 c_1(p) + \left(\frac{2}{\pi}\right)c_3(p)\right]5!\,\tilde{a}^6 \\
& \left. + \left[\left(\frac{2}{\pi}\right)^4 c_1(p) + \left(\frac{2}{\pi}\right)^2 c_3(p) + c_5(p)\right]6!\,\tilde{a}^7 + \cdots\right\} + \mathcal{O}(\varepsilon^2)\ .
\end{aligned} \tag{H.11}$$

Here we see explicitly that the small–$\tilde{a}$ expansion of $\mathrm{Re}\delta\tilde{\mathcal{L}}_\varepsilon^{(\mathrm{P.})}(\tilde{a};p)$ of (H.1) at nonzero ε exists and that this function is analytic there, having no nonanalytic terms $\sim \exp(-\mathrm{const.}/\tilde{a})$, in contrast to the expansion of $\mathrm{Re}\delta\tilde{\mathcal{L}}_0$ where ε was set equal to zero exactly (i.e., inside the integral). Further, expansion (H.12) goes over into the usual perturbation expansion $\delta\tilde{\mathcal{L}}^{\mathrm{pert.}}$ (6.31) when $\varepsilon \to +0$.

These considerations thus lead us to the following conclusions:

- The perturbative part of the induced Lagrangian density, $\mathrm{Re}\delta\tilde{\mathcal{L}}_0$ as defined in (6.26), has an abrupt IR cutoff at $w=\pi/2$, and it is numerically equal to the corresponding expression with an infinitesimally softened IR cutoff – cf. left–hand side of (H.6).

- The small–$\tilde{a}$ expansion of $\mathrm{Re}\delta\tilde{\mathcal{L}}_0(\tilde{a};p)$ reproduces the usual perturbation expansion (6.31) plus nonanalytic terms $\sim\tilde{a}^n\exp(-\mathrm{const.}/\tilde{a})$ [cf. (H.7)].

[1] In contrast to the abrupt cutoff when $\rho_0(w)=1$ for $w<(\pi/2)$, and $\rho_0(w)=0$ for $w>(\pi/2)$.
[2] We again integrate term–by–term; and we repeatedly use the identity: $\int_0^\infty du\exp(-u)u^n = n!$.

- The small–$\tilde{a}$ expansion of the corresponding expression (H.1) with a softened IR cutoff ($\varepsilon \neq 0$) yields no nonanalytic terms; when the softening of the IR cutoff becomes infinitesimal ($\varepsilon \to +0$, $\varepsilon \neq 0$), the expansion becomes identical with that of the usual perturbation expansion (6.31).

- The above points show that the nonanalytic terms in the small–$\tilde{a}$ expansion of $\mathrm{Re}\delta\tilde{\mathcal{L}}_0(\tilde{a};p)$ are only an artifact of the abruptness of the IR cutoff (the cutoff regulator becomes a nonanalytic function of the proper time w) and are thus not of a nonperturbative physical origin. $\mathrm{Re}\delta\tilde{\mathcal{L}}_0(\tilde{a};p)$ should be reinterpreted as the limit with the infinitesimally softened IR cutoff [the left–hand side of (H.6)], the latter being numerically the same but its small–$\tilde{a}$ expansion having no nonanalytic terms.

Bibliography

[1] E. A. Paschos, L. Pasquali, and J. Y. Yu, Nucl. Phys. **B588**, 263 (2000).

[2] E. A. Paschos and J. Y. Yu, Phys. Rev. **D65**, 033002 (2002).

[3] G. Cvetič and J.-Y. Yu, Int. J. Mod. Phys. **A16**, 57 (2001).

[4] G. Cvetič and J.-Y. Yu, Mod. Phys. Lett. **A15**, 1227 (2000).

[5] Y. Fukuda *et al.*, Kamiokande Collaboration, Phys. Lett. **B335**, 237 (1994).

Y. Fukuda *et al.*, Super-Kamiokande Collaboration, Phys. Lett. **B433**, 9 (1998).

Y. Fukuda *et al.*, Super-Kamiokande Collaboration, Phys. Lett. **B436**, 33 (1998).

Y. Fukuda *et al.*, Super-Kamiokande Collaboration, Phys. Rev. Lett. **81**, 1562 (1998).

[6] D. Casper *et al.*, Phys. Rev. Lett. **66**, 2561 (1991).

R. Becker-Szendy *et al.*, Phys. Rev. **D46**, 3720 (1992).

[7] K. S. Hirata *et al.*, KAMIOKANDE-II Collaboration, Phys. Lett. **B205**, 416 (1988).

K. S. Hirata *et al.*, Kamiokande-II Collaboration, Phys. Lett. **B280**, 146 (1992).

[8] J. N. Bahcall, Phys. Rept. **333**, 47 (2000).

[9] M. C. Gonzalez-Garcia, M. Maltoni, C. Pena-Garay, and J. W. F. Valle, Phys. Rev. **D63**, 033005 (2001).

[10] J. Davis, Raymond, D. S. Harmer, and K. C. Hoffman, Phys. Rev. Lett. **20**, 1205 (1968).

R. Davis, Prog. Part. Nucl. Phys. **32**, 13 (1994).

K. Lande *et al.*, Astrophys. J. **496**, 505 (1998).

K. Lande, P. Wildenhain, R. Corey, M. Foygel, and J. Distel, Nucl. Phys. Proc. Suppl. **91**, 50 (2001).

[11] K. S. Hirata *et al.*, Kamiokande-II Collaboration, Phys. Rev. **D44**, 2241 (1991).

Y. Fukuda *et al.*, Kamiokande Collaboration, Phys. Rev. Lett. **77**, 1683 (1996).

[12] K. S. Hirata *et al.*, Phys. Rev. **D38**, 448 (1988).

[13] Y. Fukuda *et al.*, Super-Kamiokande Collaboration, Phys. Rev. Lett. **81**, 1158 (1998).

Y. Suzuki, Prog. Part. Nucl. Phys. **40**, 427 (1998).

[14] A. I. Abazov *et al.*, Phys. Rev. Lett. **67**, 3332 (1991).

V. N. Gavrin, SAGE Collaboration, Nucl. Phys. Proc. Suppl. **91**, 36 (2001).

[15] P. Anselmann *et al.*, GALLEX Collaboration, Phys. Lett. **B285**, 376 (1992).

W. Hampel *et al.*, GALLEX Collaboration, Phys. Lett. **B388**, 384 (1996).

W. Hampel *et al.*, GALLEX Collaboration, Phys. Lett. **B447**, 127 (1999).

[16] K. Nakamura, K2K Collaboration, Nucl. Phys. Proc. Suppl. **91**, 203 (2001).

S. H. Ahn *et al.*, K2K Collaboration, Phys. Lett. **B511**, 178 (2001).

[17] A. B. McDonald, The SNO Collaboration, Nucl. Phys. Proc. Suppl. **91**, 21 (2000).

[18] A. Bazarko, MiniBooNE Collaboration, Nucl. Phys. Proc. Suppl. **91**, 210 (2000).

[19] P. G. Harris, Nucl. Phys. Proc. Suppl. **85**, 113 (2000).

J. Schneps, Nucl. Phys. Proc. Suppl. **87**, 189 (2000).

[20] F. Arneodo *et al.*, ICARUS and NOE Collaboration, *ICANOE: Imaging and calorimetric neutrino oscillation experiment: A proposal for a CERN-GS long baseline and atmospheric neutrino oscillation experiment*, INFN-AE-99-17.

[21] H. Shibuya *et al.*, *The OPERA emulsion detector for a long-baseline neutrino oscillation experiment*, CERN-SPSC-97-24.

K. Kodama *et al.*, *The OPERA nu/tau appearance experiment in the CERN-Gran Sasso neutrino beam*, CERN-SPSC-98-25.

A. G. Cocco, OPERA Collaboration, Nucl. Phys. Proc. Suppl. **85**, 125 (2000).

[22] F. Arneodo *et al.*, ICARUS Collaboration, *The ICARUS experiment, a second-generation proton decay experiment and neutrino observatory at the Gran Sasso laboratory*, arXiv:hep-ex/0103008.

[23] A. Piepke, KamLAND Collaboration, Nucl. Phys. Proc. Suppl. **91**, 99 (2001).

[24] G. Ranucci *et al.*, BOREXINO Collaboration, Nucl. Phys. Proc. Suppl. **91**, 58 (2001).

E. Meroni, Nucl. Phys. Proc. Suppl. **100**, 42 (2001).

[25] Y. Itow *et al.*, *The JHF-Kamioka neutrino project*, hep-ex/0106019.

[26] C. Albright *et al.*, *Physics at a neutrino factory*, hep-ex/0008064.

B. Autin *et al.*, *Prospective study of muon storage rings at CERN*, CERN-99-02.

[27] M. Hirai, S. Kumano, and M. Miyama, Phys. Rev. **D64**, 034003 (2001).

[28] K. J. Eskola, V. J. Kolhinen, and C. A. Salgado, Eur. Phys. J. **C9**, 61 (1999).

[29] K. J. Eskola, V. J. Kolhinen, and P. V. Ruuskanen, Nucl. Phys. **B535**, 351 (1998).

K. J. Eskola, V. J. Kolhinen, P. V. Ruuskanen, and C. A. Salgado, Nucl. Phys. **A661**, 645 (1999).

[30] S. L. Adler, S. Nussinov, and E. A. Paschos, Phys. Rev. **D9**, 2125 (1974).

[31] F. Vissani and A. Y. Smirnov, Phys. Lett. **B432**, 376 (1998).

[32] S. L. Adler, Ann. Phys. **50**, 189 (1968).

[33] G. L. Fogli and G. Nardulli, Nucl. Phys. **B160**, 116 (1979).

[34] D. Rein and L. M. Sehgal, Ann. Phys. **133**, 79 (1981).

[35] C. H. Llewellyn Smith, Phys. Rept. **3**, 261 (1972).

[36] P. A. Schreiner and F. V. Von Hippel, Nucl. Phys. **B58**, 333 (1973).

[37] P. A. Zucker, Phys. Rev. **D4**, 3350 (1971).

[38] S. L. Singh *et al.*, Phys. Lett. **B416**, 23 (1998).

[39] G. L. Fogli and G. Nardulli, Nucl. Phys. **B165**, 162 (1980).

[40] T. K. Gaisser, M. Nowakowski, and E. A. Paschos, Phys. Rev. **D33**, 1233 (1986).

[41] M. Nowakowski, *Interferenz und Ladungsaustauscheffekte in ausgewählten Streuprozessen*, Ph.D. thesis, University of Dortmund (1988).

[42] L. Alvarez-Ruso, S. K. Singh, and M. J. Vicente Vacas, Phys. Rev. **C57**, 2693 (1998).

[43] J. Liu, N. C. Mukhopadhyay, and L.-s. Zhang, Phys. Rev. **C52**, 1630 (1995).

[44] T. R. Hemmert, B. R. Holstein, and N. C. Mukhopadhyay, Phys. Rev. **D51**, 158 (1995).

[45] D. E. Groom *et al.*, Particle Data Group Collaboration, Eur. Phys. J. **C15**, 1 (2000).

[46] J. D. Bjorken and E. A. Paschos, Phys. Rev. **D1**, 3151 (1970).

[47] G. M. Radecky *et al.*, Phys. Rev. **D25**, 1161 (1982).

[48] S. J. Barish *et al.*, Phys. Rev. **D19**, 2521 (1979).

[49] H. J. Grabosch *et al.*, SKAT Collaboration, Z. Phys. **C41**, 527 (1989).

[50] D. Allasia *et al.*, AMSTERDAM-BOLOGNA-PADUA-PISA-SACLAY-TURIN Collaboration, Z. Phys. **C20**, 95 (1983).

[51] S. J. Barish *et al.*, Phys. Lett. **B91**, 161 (1980).

[52] S. L. Adler, Phys. Rev. **D12**, 2644 (1975).

[53] T. Bolognese, J. P. Engel, J. L. Guyonnet, and J. L. Riester, Phys. Lett. **B81**, 393 (1979).

[54] W. Krenz *et al.*, Gargamelle Neutrino Propane Collaboration, Nucl. Phys. **B135**, 45 (1978).

[55] M. Derrick *et al.*, Phys. Rev. **D23**, 569 (1981).

[56] S. J. Barish *et al.*, Phys. Rev. Lett. **33**, 448 (1974).

[57] W. Lee *et al.*, Phys. Rev. Lett. **38**, 202 (1977).

[58] S. Gasirorowicz, *Elementary Particle Physics* (John Wiley & Sons, 1966).

[59] C. W. De Jager, H. De Vries, and C. De Vries, Atom. Data Nucl. Data Tabl. **36**, 495 (1987).

[60] M. Abramowitz and I. Stegen, *Handbook of Mathematical Functions* (Dover Publications, INC. New York, 1970).

[61] M. M. Sternheim and R. R. Silbar, Phys. Rev. **D6**, 3117 (1972).

[62] R. R. Silbar and M. M. Sternheim, Phys. Rev. **C8**, 492 (1973).

[63] L. D. Roper, Phys. Rev. Lett. **12**, 340 (1960).

[64] A. Bohr and B. A. Mottelson, *Nuclear structure vol. I* (W. A. Benjamin, INC. New York, 1969).

[65] P. Musset and J. P. Vialle, Phys. Rept. **39**, 1 (1978).

[66] R. Merenyi *et al.*, Phys. Rev. **D45**, 743 (1992).

[67] K. Nishikawa, Nucl. Phys. Proc. Suppl. **77**, 198 (1999).

[68] L. J. Hall and H. Murayama, Phys. Lett. **B463**, 241 (1999).

[69] M. Apollonio *et al.*, CHOOZ Collaboration, Phys. Lett. **B420**, 397 (1998).
M. Apollonio *et al.*, CHOOZ Collaboration, Phys. Lett. **B466**, 415 (1999).

[70] E. Derman, Phys. Rev. **D7**, 2755 (1973).

[71] C. H. Albright and C. Jarlskog, Nucl. Phys. **B84**, 467 (1975).

[72] H. L. Lai *et al.*, CTEQ Collaboration, Eur. Phys. J. **C12**, 375 (2000).

[73] J. Lϕvseth, Phys. Lett. **5**, 199 (1963).
J. Lϕvseth, Nuovo Cim. **57**, 382 (1968).

[74] Y.-P. Yao, Phys. Rev. **176**, 1680 (1968).

[75] G. Battistoni, P. Lipari, J. Ranft, and E. Scapparone, *Simulation of nuclear effects in quasi elastic and resonant neutrino interactions*, hep-ph/9801426.

[76] J. S. Bell and C. H. Llewellyn Smith, Nucl. Phys. **B28**, 317 (1971).

[77] S. K. Singh and E. Oset, Nucl. Phys. **A542**, 587 (1992).

[78] D. C. Colley *et al.*, Z. Phys. **C2**, 187 (1979).

[79] N. J. Baker *et al.*, Phys. Rev. **D25**, 617 (1982).

[80] P. S. Auchincloss *et al.*, Z. Phys. **C48**, 411 (1990).

[81] W. G. Seligman, *A Next-to-leading order QCD analysis of neutrino - iron structure functions at the Tevatron*, Ph.D. thesis, University of Columbia (1997), NEVIS-292.

[82] D. MacFarlane *et al.*, Z. Phys. **C26**, 1 (1984).

[83] M. Arneodo *et al.*, European Muon Collaboration, Z. Phys. **C35**, 433 (1987).

[84] J. V. Allaby *et al.*, CHARM Collaboration, Z. Phys. **C38**, 403 (1988).

[85] C. Baltay *et al.*, Phys. Rev. Lett. **44**, 916 (1980).

[86] S. Ciampolillo *et al.*, Gargamelle Neutrino Propane Collaboration, Phys. Lett. **B84**, 281 (1979).

[87] J. G. Morfin *et al.*, Gargamelle SPS Collaboration, Phys. Lett. **B104**, 235 (1981).

[88] A. I. Mukhin *et al.*, Sov. J. Nucl. Phys. **30**, 528 (1979).

[89] D. S. Baranov *et al.*, Phys. Lett. **B81**, 255 (1979).

[90] E. Aslanides *et al.*, ANTARES Collaboration, *A deep sea telescope for high energy neutrinos*, astro-ph/9907432.

[91] L. K. Resvanis, Nucl. Phys. Proc. Suppl. **87**, 448 (2000).

[92] E. Andres *et al.*, AMANDA Collaboration, Nucl. Phys. Proc. Suppl. **91**, 423 (2000).

[93] V. Balkanov *et al.*, BAIKAL Collaboration, *A search for very high energy neutrinos with the Baikal Neutrino Telescope*, astro-ph/0105269.

[94] S. J. Barish *et al.*, Phys. Rev. **D16**, 3103 (1977).

[95] S. Bonetti *et al.*, Nuovo Cim. **A38**, 260 (1977).

[96] S. V. Belikov *et al.*, Z. Phys. **A320**, 625 (1985).

[97] The neutrino flux ν_μ is taken from the http:www.cern.ch/NGS.

[98] A. M. Gago, E. M. Santos, W. J. C. Teves, and R. Zukanovich Funchal, Phys. Rev. **D63**, 113013 (2001).

[99] A. Rubbia, Nucl. Phys. Proc. Suppl. **91**, 223 (2000).

[100] W. Heisenberg and H. Euler, Z. Phys. **98**, 714 (1936).

[101] V. Weisskopf, Kgl. Danske Videnskabs. Selskabs.Mat.-fys. Medd. 14, No. 6.

[102] J. Schwinger, Phys. Rev. **82**, 664 (1951).

[103] B. M. W. Greiner and J. Rafelski, *Quantum Electrodynamics of Strong Fields* (Springer, Berlin, heidelberg, 1985).

[104] W. Dittrich and M. Reuter, *Effective Lagrangians in Quantum Electrodynamics* (Springer, 1985).

[105] J. Schwinger, *Particles, Sources and Fields Vol. II* (Addison-Wesley, 1989), Chapters. 4-8.

[106] C. Itzykson and J.-B. Zuber, *Quantum Field Theory* (McGraw-Hill,New York, 1980), Chapters. 4-3.

[107] I. A. Batalin, S. G. Matinian, and G. K. Savvidy, Sov. J. Nucl. Phys. **26**, 214 (1977).

[108] R. Ragazzon, Phys. Rev. **D52**, 2422 (1995).

[109] P. Schwab, Phys. Lett. **B109**, 47 (1982).

[110] A. B. Migdal and S. B. Khokhlachev, JETP Lett. **41**, 194 (1985).

[111] V. I. Ritus, Sov. Phys. JETP **42**, 774 (1975).

V. I. Ritus, Zh. Eksp. Teor. Fiz. **73**, 807 (1977).

V. I. Ritus, *Effective Lagrange function of intense electromagnetic field in QED*, hep-th/9812124.

V. I. Ritus, in *Proceedings the Conference Frontier Tests of QED and Physics of the Vacuum, Sandansky, Bulgaria, June, 1998*, edited by D. B. E. Zavattini and C. Rizzo (Heron Press, Sofia, 1998), pp. 11–28, hep-ph/9812124.

[112] M. Reuter, M. G. Schmidt, and C. Schubert, Annals Phys. **259**, 313 (1997).

[113] G. V. Dunne and C. Schubert, Nucl. Phys. **B564**, 591 (2000).

[114] F. Sauter, Z. Phys. **69**, 742 (1931).

[115] O. Klein, Z. Phys. **53**, 157 (1929).

[116] A. I. Nikishov, Zh. Eksp. Teor. Fiz. **57**, 1210 (1969).

[117] A. Casher, H. Neuberger, and S. Nussinov, Phys. Rev. **D20**, 179 (1979).

[118] D. L. Burke *et al.*, Phys. Rev. Lett. **79**, 1626 (1997).

[119] Z. Bialynicka-Birula and I. Bialynicki-Birula, Phys. Rev. **D2**, 2341 (1970).

[120] S. L. Adler, Annals Phys. **67**, 599 (1971).

[121] E. Brezin and C. Itzykson, Phys. Rev. **D3**, 618 (1971).

[122] W.-Y. Tsai and T. Erber, Phys. Rev. **D10**, 492 (1974).

[123] W. Dittrich and H. Gies, Phys. Rev. **D58**, 025004 (1998).

W. Dittrich and H. Gies, in *Proceedings the Conference Frontier Tests of QED and Physics of the Vacuum, Sandansky, Bulgaria, June, 1998*, edited by D. B. E. Zavattini and C. Rizzo (Heron Press, Sofia, 1998), pp. 29–43, hep-ph/9806417.

[124] D. Bakalov, Nucl. Phys. Proc. Suppl. **35**, 180 (1994).

[125] S. A. Lee *et al.*, *Measurement of the magnetically-induced QED birefringence of the vacuum and an improved laboratory search for light pseudoscalars*, Measurement of the magnetically-induced QED birefringence of the vacuum and an improved laboratory search for light pseudoscalars, FERMILAB-PROPOSAL-P-877A.

[126] U. D. Jentschura, J. Becher, E. J. Weniger, and G. Soff, Phys. Rev. Lett. **85**, 2446 (2000).

[127] G. Cvetič, private notes, DO-TH 97/19.

[128] W. Dittrich and H. Gies, Springer Tracts Mod. Phys. **166**, 1 (2000).

[129] R. D. Peccei, J. Sola, and C. Wetterich, Phys. Rev. **D37**, 2492 (1988).

[130] G. A. Baker Jr. and P. Graves-Morris, *Padé Approximants 2nd ed. Encyclopedia of Mathematics and Its Applications Vol 59* (Cambridge University Press, Cambridge, 1996), ed. Gian-Carlo Rota.

[131] A. H. Mueller, Nucl. Phys. **B250**, 327 (1985).

V. I. Zakharov, Nucl. Phys. **B385**, 452 (1992).

A. I. Vainshtein and V. I. Zakharov, Phys. Rev. Lett. **73**, 1207 (1994).

M. Beneke, Phys. Rept. **317**, 1 (1999).

[132] C. B. Chiu and S. Nussinov, Phys. Rev. **D20**, 945 (1979).

[133] P. A. Raczka, Phys. Rev. **D43**, 9 (1991).

[134] M. Pindor, *Pade approximants and Borel summation for QCD perturbation expansions* (1999), hep-th/9903151.

[135] U. D. Jentschura, Phys. Rev. **D62**, 076001 (2000).

[136] G. V. Dunne and T. M. Hall, Phys. Rev. **D60**, 065002 (1999).

[137] E. J. Weniger, Ann. Phys. (N. Y.) **246**, 133 (1996).

[138] S. G. Gorishnii and S. A. Larin, Phys. Lett. **B172**, 109 (1986).

E. B. Zijlstra and W. L. van Neerven, Phys. Lett. **B297**, 377 (1992).

[139] D. J. Broadhurst and A. L. Kataev, Phys. Lett. **B315**, 179 (1993).

[140] X.-D. Ji, Nucl. Phys. **B448**, 51 (1995).

C. N. Lovett-Turner and C. J. Maxwell, Nucl. Phys. **B452**, 188 (1995).

[141] G. Cvetič, Phys. Lett. **B486**, 100 (2000).

[142] G. Grunberg, Phys. Lett. **B304**, 183 (1993).

[143] M. Beneke and V. M. Braun, Phys. Lett. **B348**, 513 (1995).

P. Ball, M. Beneke, and V. M. Braun, Nucl. Phys. **B452**, 563 (1995).

Y. L. Dokshitzer, G. Marchesini, and B. R. Webber, Nucl. Phys. **B469**, 93 (1996).

E. Gardi and G. Grunberg, JHEP **11**, 016 (1999).

[144] S. G. Matinian and G. K. Savvidy, Nucl. Phys. **B134**, 539 (1978).

[145] E. Gardi, G. Grunberg, and M. Karliner, JHEP **07**, 007 (1998).

F. A. Chishtie, V. Elias, V. A. Miransky, and T. G. Steele, Prog. Theor. Phys. **104**, 603 (2000).

[146] S. Wolfram, *The Mathematica book* (Wolfram media & Cambridge press, 1999).

[147] R. D. Ball, Phys. Rept. **182**, 1 (1989).

G. Cvetič, Annals Phys. **255**, 165 (1997).

Acknowledgements

First and foremost, I would like to thank my supervisor Prof. Dr. E. A. Paschos for his instructive scientific guidance and for a fruitful collaboration. I have benefitted from his continuous advice on main topics covered in this thesis as well as his generous support over the last years.

I am no less grateful to Dr. G. Cvetič for a fruitful collaboration and valuable advice. He has generously shared his insight with me and his knowledge has guided this investigation.

Thanks to Dr. L. Pasquali for a collaboration on the single pion production calculation. Particularly I would like to thank Dr. I. Schienbein for valuable and very helpful discussions about physics and for very carefully correcting this thesis. In addition thanks to W. Rodejohann for very helpful and constructive discussions about physics. I enjoyed it immensely.

Finally, I would like to thank all other (former) Dortmund colleagues, explicitly J. Noritzsch and Dr. H. Sprenger for their steady administration of our computer system and for help concerning LaTeX questions and P. Henselder for reading of this thesis and for a pleasant atmosphere and Dr. M. Flanz and B. Bucker for a nice working atmosphere and Susanne Laurent for her help with any kind of works. I enjoyed the many discussions about exciting non physics topics with TIII and TIV colleagues, too.